Cloud detection using the WSR-88Ds

Valery Melnikov*[#], Stephen Castleberry[*+], Richard Murnan[+], and Maj. David McDonald[+]

* Cooperative Institute for Mesoscale Meteorological Studies, the University of Oklahoma
[+] Radar Operations Center, the National Weather Service
[#] NOAA/OAR National Severe Storms Laboratory

September 2016

Table of Contents

1. Introduction

The understanding of climate and the monitoring of its change are very important for geoscience. Clouds are one of the main climatic components, so any information on clouds is important. The number of instruments for cloud studies is growing rapidly, and remote sensing of clouds with the WSR-88Ds can complement other information sources and deliver unique cloud data which is impossible to obtain with other instruments.

The WSR-88D radar has been designed to monitor severe weather and measure precipitation. The radars have superb sensitivity and are capable of observing precipitation at distances beyond 450 km. Such sensitivity allows observing non-precipitating clouds at shorter distances. Thick nonprecipitating clouds can be observed at distances beyond 200 km. The WSR-88D can operate in two distinct modes with different pulse widths called short and long. Both modes can be used to observe non-precipitating clouds. These modes have their advantages and drawbacks that are analyzed in this study (section 2).

Non-precipitating clouds are usually observed by cloud radars operating at mm-wavelengths with vertically pointing antennas to achieve high detectability (Kropfli and Kelly 1996, Moran et al. 1998, Kolias et al. 2007). Several such radars with a wavelength of 8 mm have been installed around the globe for the Atmospheric Radiation Measurement (ARM) program. The ARM cloud profiling 8mm-wavelength radars are capable of observing clouds with reflectivity values of -30 dBZ (the general mode) at a distance of 10 km. The cloud profiling radars (CPR) onboard the Cloudsat satellite operates at 3-mm-wavelength and is capable of observing reflectivity of -30 dBZ (Stephens et al. 2002). Minimal reported reflectivity observed with the WSR-88D is -25 dBZ at 10 km (Melnikov et al. 2011, see also Table 8.1 in section 8 of this report), which is comparable with the detectability of cloud radars. This level of detectability allows observing cirrus clouds which absorb only 6-10% of atmospheric radiation. Detection of non-precipitating clouds with the WSR-88Ds is discussed in the first 9 sections of this report. Detectability of the WSR-88D and CPR is compared in section 10.

Information from the WSR-88Ds is usually presented in conical cross-sections (the PPI representation). Non-precipitating clouds are often strongly non-uniform in the vertical direction. So, to observe the inner structures of clouds, vertical radar cross-sections (RHI) are often preferable. Numerous images in this report are presented as RHIs. On the other hand, clouds can be non-uniform in the horizontal direction. So it is evident that a three-dimensional (3D) presentation of radar images is desirable for clouds. Current VCPs have wide gaps between adjacent elevation angles at high elevations. These gaps can be filled in by using different interpolation schemes. One of the goals of this study is the 3D imaging with reliable interpolations of data in the gaps between the adjacent elevations (section 3).

The WSR-88Ds can be used to map non-precipitating clouds and to obtain their tops and bottoms. This information is useful for aviation, cloud modeling, and can also be used as an input to the atmospheric radiation problems (section 4). The WSR-88Ds also measure the

Doppler velocities and spectrum width (in the short pulse mode), which can be utilized in cloud models and is important for pilots to warn for hazardous wind shears and turbulence (section 5).

The highest elevation angle of the current volume coverage patterns (VCP) is 19.5° for the precipitation VCPs and 4.5° for the "clear air" VCPs. Non-precipitating clouds can be located at high altitudes which cannot be reached at such elevations at distances close to radar. These maximal elevations cause cones of silence or "no data" areas above radar sites. The maximal possible elevation angle for the WSR-88D is 60°; the system has a mechanical stopper at this elevation. Elevations of 20 - 60° are advantageous for observing very thin clouds close to the WSR-88Ds but the current VCPs do not scan these elevations. So, one of the goals of this study is to assess the capability of current VCPs in detecting non-precipitating clouds.

The WSR-88Ds are polarimetric radars; they deliver differential reflectivity, differential phase, and correlation coefficient products along with the base radar products, i.e., reflectivity, Doppler velocity, and spectrum width. The polarimetric variables can be used to distinguish cloud radar echoes and echoes from atmospheric biota. The polarimetric variables can be used to obtain the shapes of cloud hydrometeors (section 7) that could be of interest for cloud modeling.

Transitioning from clouds to rain is poorly understood process (Stephens and Kummerow 2007). Data on transitioning of water vapor into cloud droplets, i.e., cloud growth, and then into rain can be obtained from radars: WSR-88D is capable of mapping nonprecipitating clouds and small areas of precipitation (section 6).

Measurements of Doppler velocity in clouds can be used to obtain wind velocities up to heights of 12-13 km where clouds may exist. Such heights are problematic for the wind profilers so the data from WSR-88Ds can complement information from the profilers (section 8). Differential reflectivity (Z_{DR}) values from clouds can be used to monitor the system Z_{DR} bias (section 12). A version of a cloud detection algorithm for the WSR-88Ds is described in section 13 for the standard and possible cloud VCPs.

Potential users of cloud information from the WSR-88Ds are aviation services (such as the Federal Aviation Administration), cloud modelers of the NWS and other agencies / universities, climatologists of the NWS and universities, and cloud physicists working on microphysical cloud characteristics in universities and at the National Aeronautics and Space Administration (NASA).

2. The WSR-88D's long and short pulse modes for cloud mapping

The WSR-88D is capable of transmitting two pulses of different length: the short pulse (1.54 µs long), which is equivalent to 250 m radial resolution and the long pulse (4.5 µs) with 750 m radial resolution. Radial sampling in the long pulse mode is set to 500 m, which is more convenient for data presentation. So there is range oversampling in this mode in operational VCPs. The maximal pulse repetition frequency (PRF) in the long pulse mode is 460 Hz, which provides a large unambiguous range of 326 km with unambiguous Doppler velocity of ±11.5 m s^{-1} (the wavelength of 10 cm). The PRF in the long pulse operational VCPs is typically set at 320

Hz to have an unambiguous range of 460 km. Such VCPs are used to observe distant storms, but their Nyquist interval is only 8 m s^{-1}, which is not sufficient for velocity measurements. The maximal PRF in the short pulse mode is 1280 Hz that allows measurements of Doppler velocity in an interval of ±32 m s^{-1} with the unambiguous range of 117 km. These parameters are adequate for mapping the majority of nonprecipitating clouds. Detectability of clouds in the long pulse mode is 9 dB better that that in the short pulse mode. To map clouds at long distances, the long pulse mode is preferable but to obtain more detailed cloud structures and measure the Doppler velocities and spectrum widths, the short pulse should be used.

Detectability of clouds depends on its water/ice content and range from radar. Fig. 2.1 presents genuine RHIs collected with KOUN on 19 February 2014 in the long and short pulse modes. The RHI's azimuths are the same (30°) and the time difference between the RHIs is about 8 minutes. These are non-precipitating clouds that are observed up to 300 km in the long pulse mode. The bending of radar echoes at large distances is due to Earth's curvature and diminishing detectability of weak echoes. Such bending is not apparent in the short pulse mode (the bottom image in Fig. 2.1).
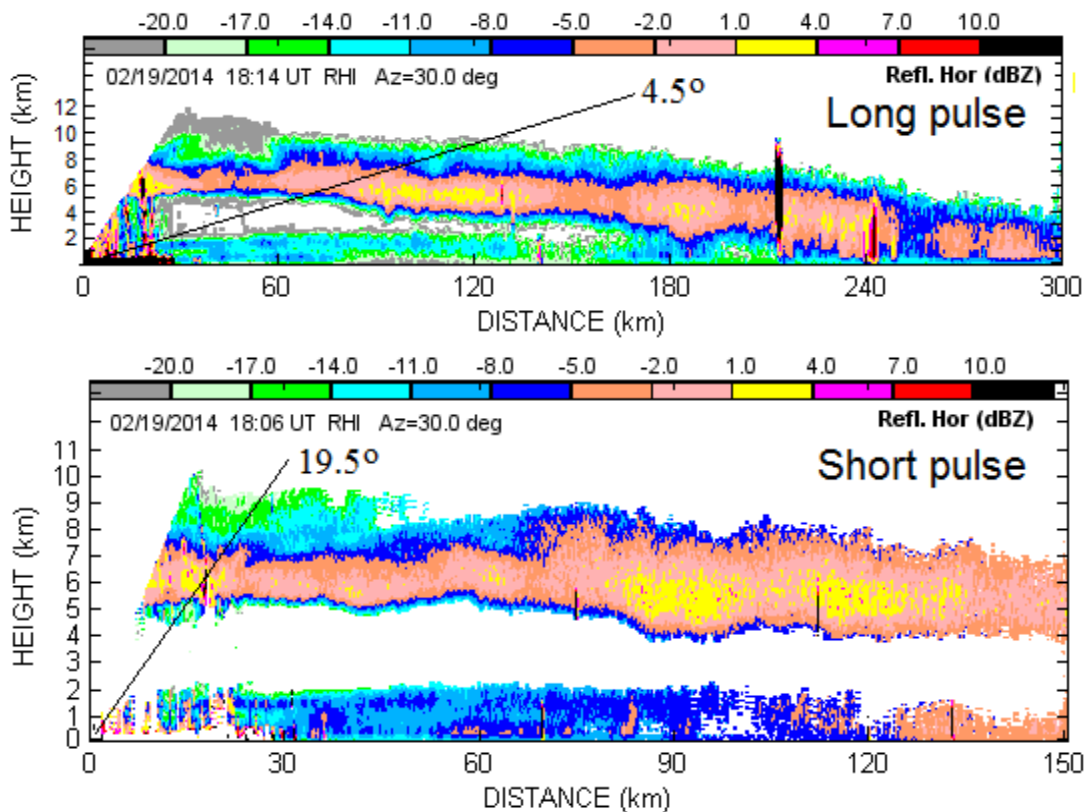
Fig. 2.1: RHIs of reflectivity of nonprecipitating clouds collected with the long (the top panel) and short (the bottom panel) radar pulses. WSR-88D KOUN. The thin black lines are maximum elevations for the clear air (4.5°) and precipitation (19.5°) VCPs. The thick black vertical line in the upper panel at a distance of about 215 km is most likely from an airplane.

6

One can see from Fig. 2.1 that the maximal height of the cloud is larger in the echo collected with the long pulse mode than that in the short pulse mode. In the long pulse mode, the height reaches 12 km at the ranges closest to the radar, whereas the maximal height in the short pulse mode is about 10 km. This is a manifestation of the better detectability of the long pulse mode. The maximal antenna elevations in the VCPs that use the long and short pulses are shown with the thin black lines. Data in Fig. 2.1 have been collected with KOUN in the genuine RHI mode, i.e., they have not been reconstructed from PPIs. It is evident that if KOUN had run a standard clear air VCP, the maximal cloud top would be measured at 9.5 km whereas its maximal heights at closer distances reach 12 km. A similar observation holds for the bottom panel: the cloud top at 19.5° is at 9 km whereas the height at higher elevations reaches 10 km. Cloud tops vary with range so some difference between the tops obtained at higher elevation and the standard maximum VCP's elevations can be natural but our cloud measurements show that the tops obtained at high elevations are frequently larger than those obtained at lower elevations. So to measure the maximal cloud heights, high antenna elevations are desirable.
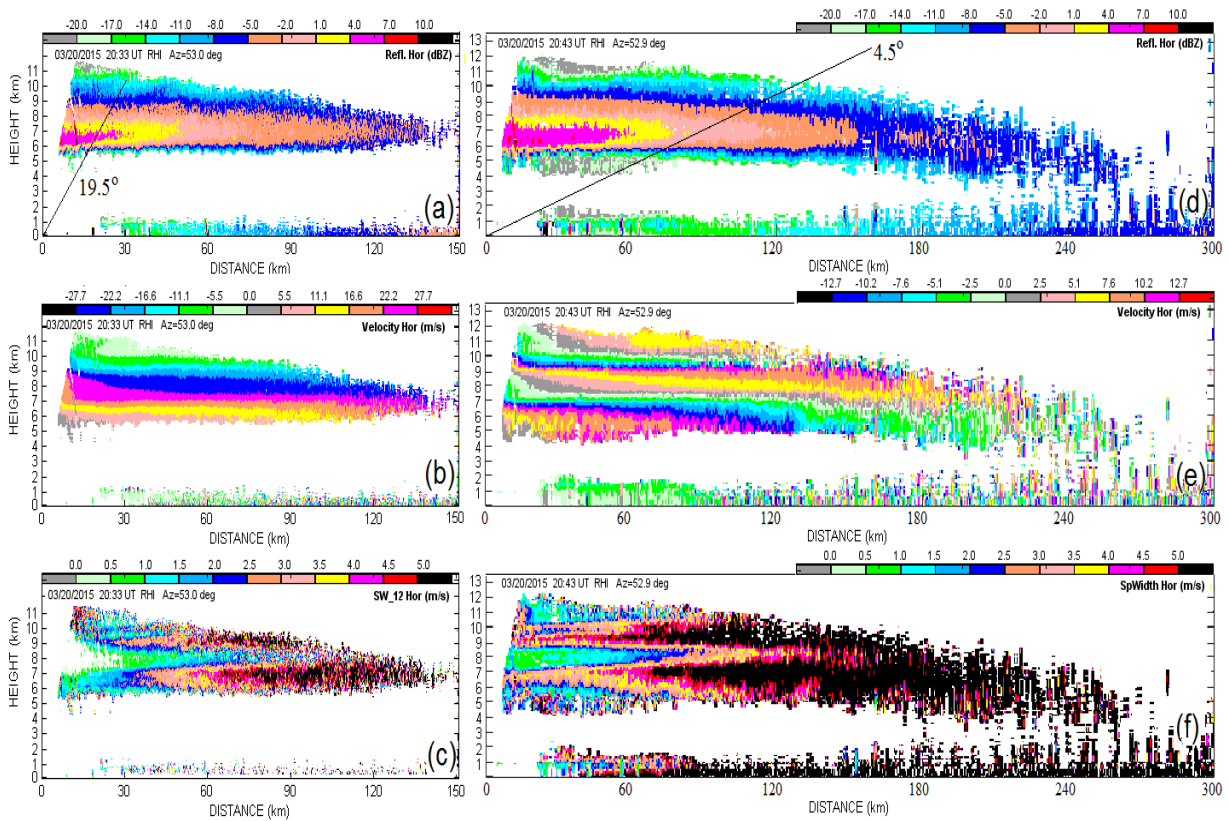
Fig. 2.2 (a, b, c): RHI collected with KOUN data on 20 March 2015 at 2033 UTC at the azimuth of 53° in the short pulse mode. The back line in panel (a) has an elevation of 19.5°. (d, e, f): Same as in (a, b, c) but at 2043 UTC and in the long pulse mode. The line in panel (d) has an elevation of 4.5°

7

Fig. 2.2 presents RHIs collected in the short (the left column) and long (the right column) pulse modes at the same azimuth. The time lag between the images is 10 minutes. One can see that radar echoes in the short and long pulse modes stretches to 150 km and 270 km correspondingly that demonstrates the difference in sensitivity. The slant black line in panel (a) represents the elevation of 19.5°, i.e., the maximal elevation angle in the short pulse VCPs. The cloud top and bottom obtained at this elevation are 10.8 and 5.6 km whereas at the elevation of 55°, they are 11.6 and 5.4 km. Such a difference could be significant for cloud modelling and is important for aviation. The slant black line in panel (d) is at 4.5°, which is the maximal elevation in the VCPs operating at the long pulse. The echo top at this elevation is 10.0 km, i.e., significantly lower than true height, i.e., 12.2 km. It is also seen that if the antenna had gone higher in the long pulse mode, the cloud tops would be obtained correctly.

The velocity panels in Fig. 2.2 demonstrate the need of a large Nyquist interval to measure the Doppler velocity. One can see a velocity folding in panel (b) obtained with the Nyquist interval of $\pm$ 27.7 m s^{-1}. The Doppler velocity in panel (e) exhibits two altitudes with folding.

The WSR-88D KTLX (Oklahoma City, OK) is located 19.95 km to the North-East from KOUN. This distance is short enough for the comparison of radar data collected with these two radars. KTLX is an operational system and runs the standard VCPs. On 20 March 2015 at the time shown in Fig. 2.2 for KOUN, KTLX was running a clear air VCP with the maximum elevation angle of 4.5°. Fig. 2.3 presents KTLX's images that can be compared with those presented in Fig. 2.2. Fig. 2.3b is a PPI Image collected with KTLX at the highest elevation. An annular ring pattern indicates layered clouds above the radar. To measure the cloud heights and to produce pseudo-vertical cross-sections, the WDSS-II software has been used. To measure the maximum cloud height, the very far point in the outer cloud boundary has been obtained with the built-in Readout tool (Fig. 2.3c). It is 9.6 km, which agrees well with 9.5 km obtained from KOUN at an elevation of 4.5° (Fig. 2.2d). Note that the maximum cloud tops obtained with KOUN at higher elevations is 12 km.

A pseudo-vertical cross-section from KTLX at an azimuth of 53°, i.e., the azimuth in which data in Fig. 2.2 were collected with KOUN, is shown in Fig. 2.3a. The "saw-tooth" pattern results from a large elevation steps at higher elevations. One can see that the genuine RHI (Fig. 2.2) presents cloud structure in more detail that reconstructed RHI in Fig. 2.3. The maximal cloud height obtained from Fig. 2.3a is 9.3 km (the left highest peak of the saw-tooth pattern), which is 200 m lower than 9.5 km obtained from KOUN at the same azimuth. It can be concluded that the standard operational VCPs can be used to obtain the presence of nonprecipitating clouds and estimate the heights of their boundaries.
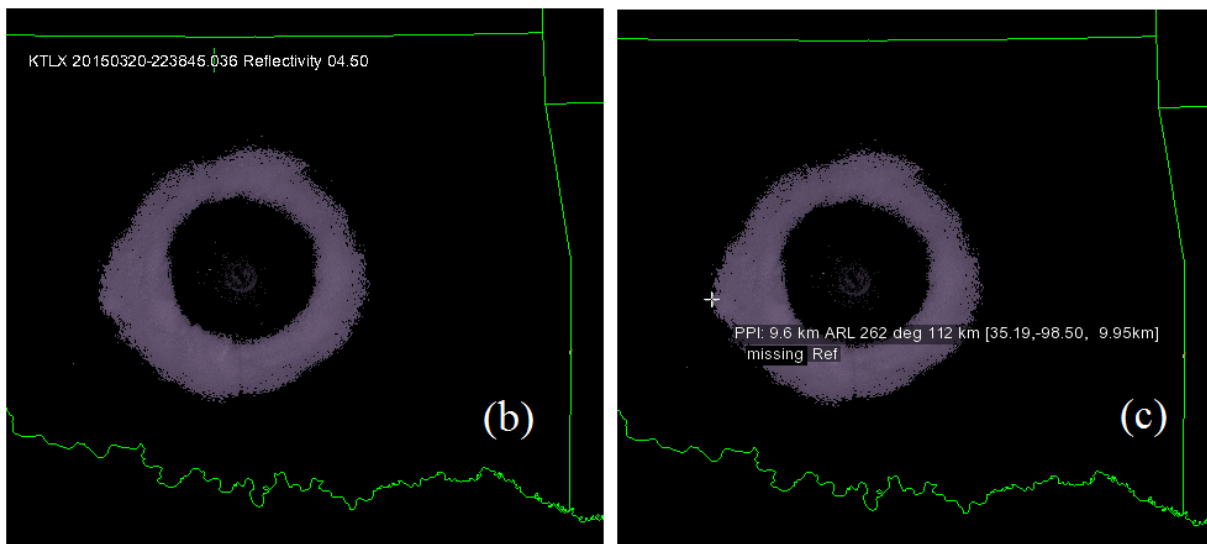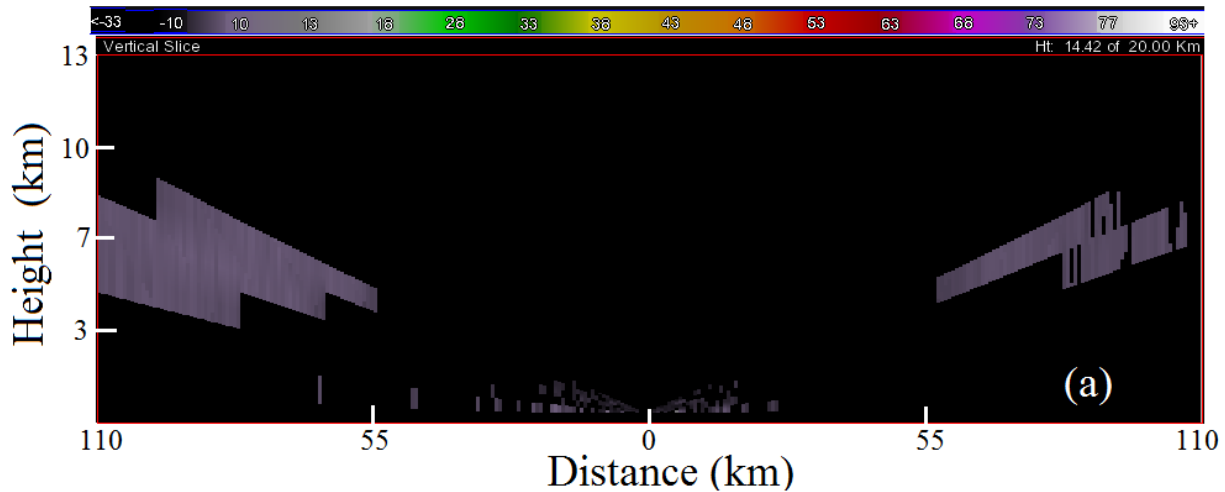
Fig. 2.3 (a): RHI in azimuth 53° collected with KTLX on 20 March 2015 at 2238 UTC, (b): PPI at the elevation of 4.5^o, (c): Measurement of the cloud top with the built-in Readout function of WDSS-II software.

     The WSR-88D is capable of range oversampling with a factor of 5 in the short pulse mode. This allows representing the data with radial resolution of 50 m (250/5), which is advantageous for a detailed mapping of clouds and precise measurements of the cloud tops and bottoms that can be beneficial for aviation. RHIs in Fig. 2.4 were collected in this mode. The black line in the reflectivity panel is at 19.5^o. One can see that at this elevation, the echo top is at the height of 10.55 km but the maximal top is at 11.25 km. This demonstrates the capability of range oversampling for more accurate measurements of the cloud tops and bottoms. Range oversampling requires the number of range gates be a factor of 5 larger than that of regular sampling. Thus this technique can be used for cloud observations at distances up to about 60 km (1200 range gates) that could be needed for detailed cloud studies.
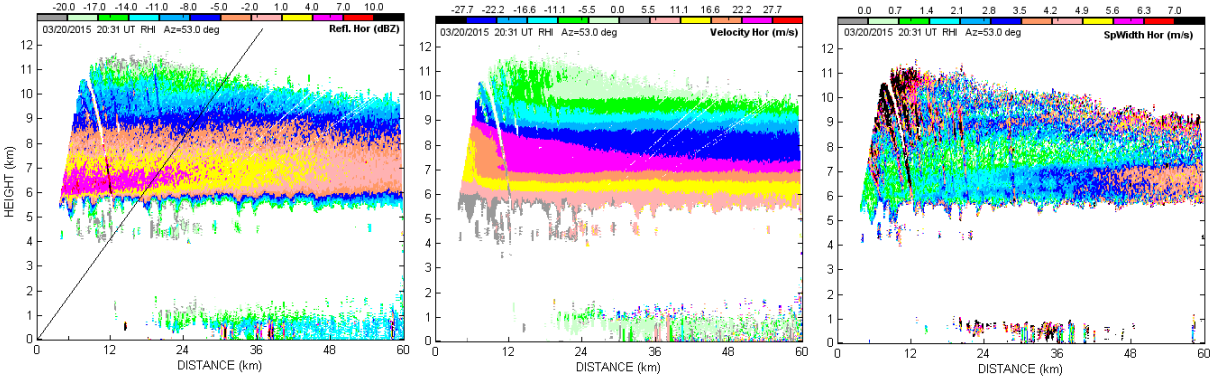
Fig. 2.4: Same as in Fig. 2.2 but collected in the short pulse mode with radial resolution of 50 m. The black line in the left panel has an elevation of 19.5°.

      The accuracy of measurements of the heights of cloud tops and bottoms is important for aviation and cloud modeling. The uncertainty of height measurements depends on the radial length of the gate and the distance to the radar range gate because of the increase of radar beam with range (Fig. 2.5). Let the radar beam be at an elevation angle θ and the height be measured at a range gate located at range R. The two-way radar beam boundaries are shown in Fig. 2.5 with the solid red lines and the beam's center is depicted with the dashed red line. The two-way radar beam for the WSR-88D is $\varphi = 0.5°$ (the one-way beam-width is about $1°$). The radial resolution is ΔR. There are two uncertainties ΔH_1 and ΔH_2 in the height measurement. The first uncertainty results from a finite ΔR and the second one is due to the beam-width. One can see that $\Delta H_1 = \Delta R \sin\theta$ and $\Delta H_2 = R\varphi \cos\theta$. The latter is valid for $\Delta R << R$, which typically holds in radar measurements. For instance, at height $H = 5$ km at the maximum elevation of 4.5° of the clear air VCPs, $\Delta H_1 = 59$ m and $\Delta H_2 = 557$ m. It is seen that the uncertainty of height measurements in the clear air VCPs is determined by ΔH_2, which equals 560 m at a range of 50 km and 1200 m at a range of 100 km. The uncertainty of height measurements from the Cloudsat satellite is 500 m which equals ΔH_2 at a range of 50 km from the radar.
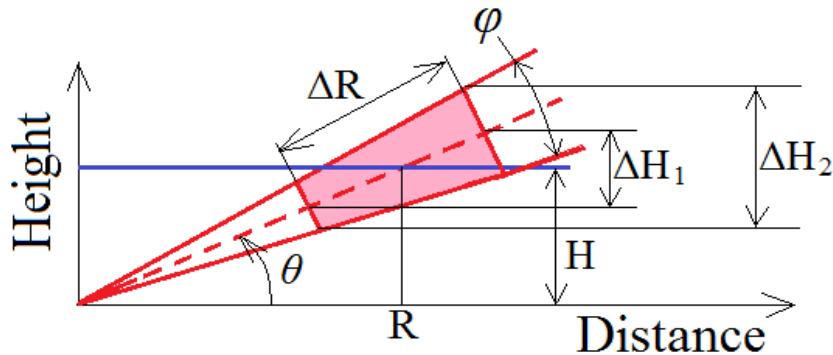

Fig. 2.5: Geometry of the uncertainty of height measurement.

10

In the precipitation VCPs, $\Delta R = 250$ m and the maximum elevation angle is 19.5°. So $\Delta H_1 = 83$ m and $\Delta H_2 = 525$ (1050) m at R = 50 (100) km which are close to the numbers for the clear air VCPs. So, the uncertainty of height measurements is mainly determined by the beam-width and is about 500 and 1000 m at ranges of 50 and 100 km respectively.

The weak dependence of measured cloud heights from the radar length at elevations lower than 40° makes measurements with the long pulse advantageous in comparisons with those that use the short pulse. Since the measurement uncertainty mainly depends on the beam-width, and not the pulse length. The sensitivity of the long pulse mode is several dB higher than that of the short pulse.

3. 2D and 3D display of radar cloud echoes

The operational WSR-88Ds scan over azimuth at predetermined elevations (PPI scans). Nonprecipitating clouds in a PPI display may appear in a form of an annular ring (Fig. 2.3b, c; Fig. 3.1). The inner boundary of annular echo in Fig. 3.1 is the lower cloud bound, and the outer boundary presents the cloud tops. The center of annular ring is sporadically filled with echoes from insects and leftovers of ground clutter filtering.
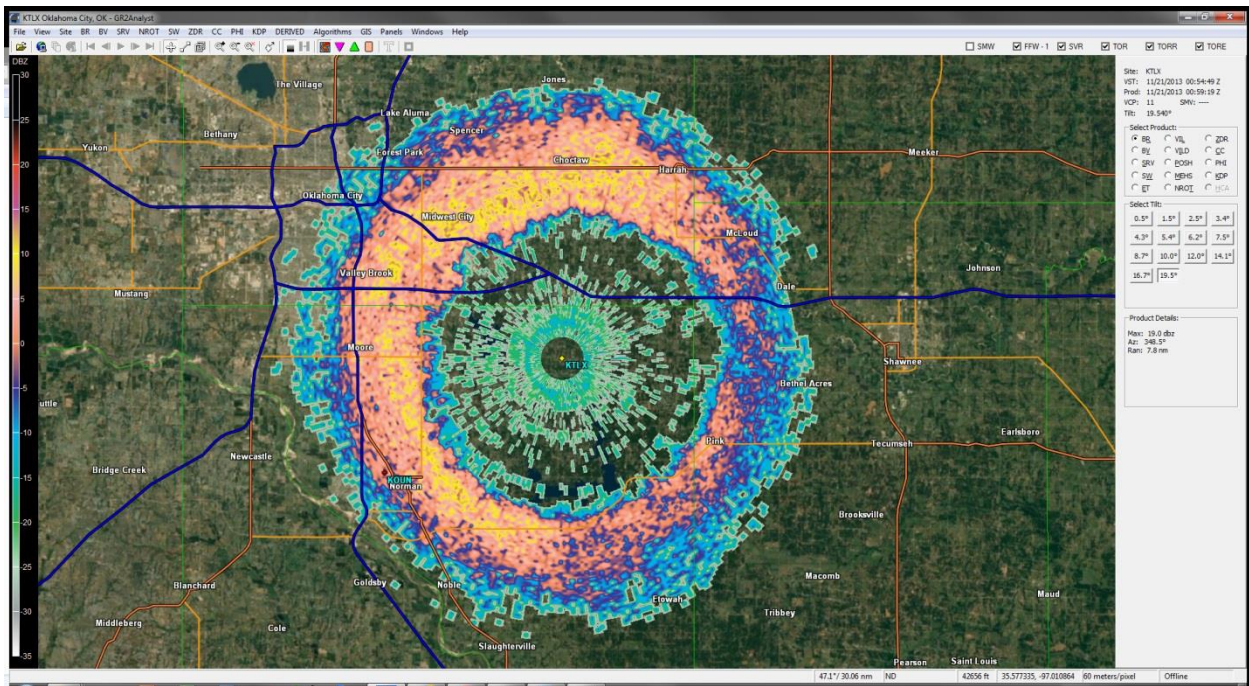
Fig. 3.1: Reflectivity PPI scan at 19.5° from KTLX collected on 11/21/2013 at 0059 UTC.

The software package WDSS-II is capable of producing pseudo-RHI images through a given direction; an example is in Fig. 2.3a. Pseudo-RHIs are generated from PPIs collected at predetermined elevations. The steps between elevations increase with their height so the echo edges have a saw-tooth shape (Fig. 2.3a). The WSR-88D KOUN is capable of making true RHIs,

i.e., a vertical cross-section collected with antenna scanned over elevations at a fixed azimuth (Fig. 2.1, Fig. 2.2, and Fig. 2.4). Such RHIs present vertical cloud structure in detail but such a field is for a single azimuth. Important cloud parts at other azimuths can be missed. Neither PPIs nor RHIs are capable of representing clouds adequately. So a 3D representation is natural for clouds. But 3D images are produced from PPIs collected at fixed elevations thus "saw-tooth" shapes are visible in 3D images as well. One of the main problems in producing 3D images is the approximation of data in between the elevation cuts. Cloud observations demonstrate tremendous variability in cloud parameters so it is hard to formulate general criteria for a gap-filling algorithm. A 3D image of reflectivity field of the case in Fig. 3.1 is shown in Fig. 3.2.
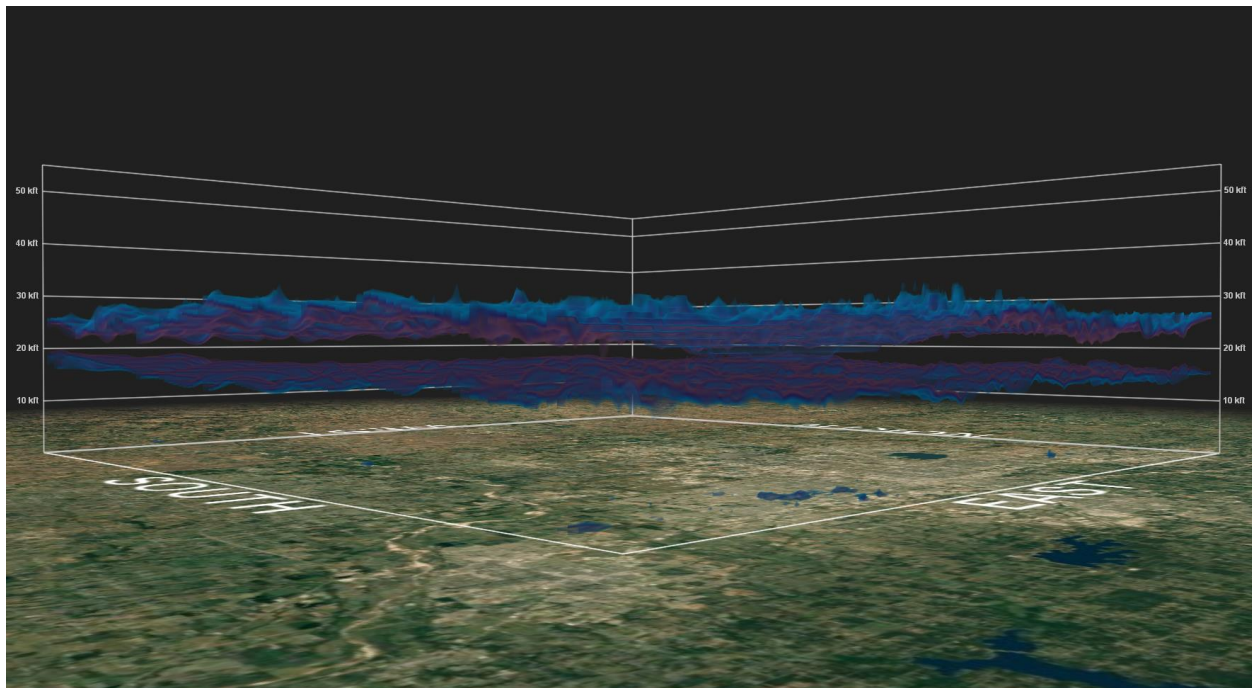
Fig. 3.2: 3D reflectivity field for the case of Fig. 3.1. The plot indicates that multiple cloud layers are likely present.

There is one more form of the 3D representation of clouds generated using the Gibson Ridge Level-II (GR2 Analyst) software package shown in Fig. 3.3. A horizontal projection of a cloud radar echo is placed on the ground and a pseudo-vertical cross-section is placed above it.
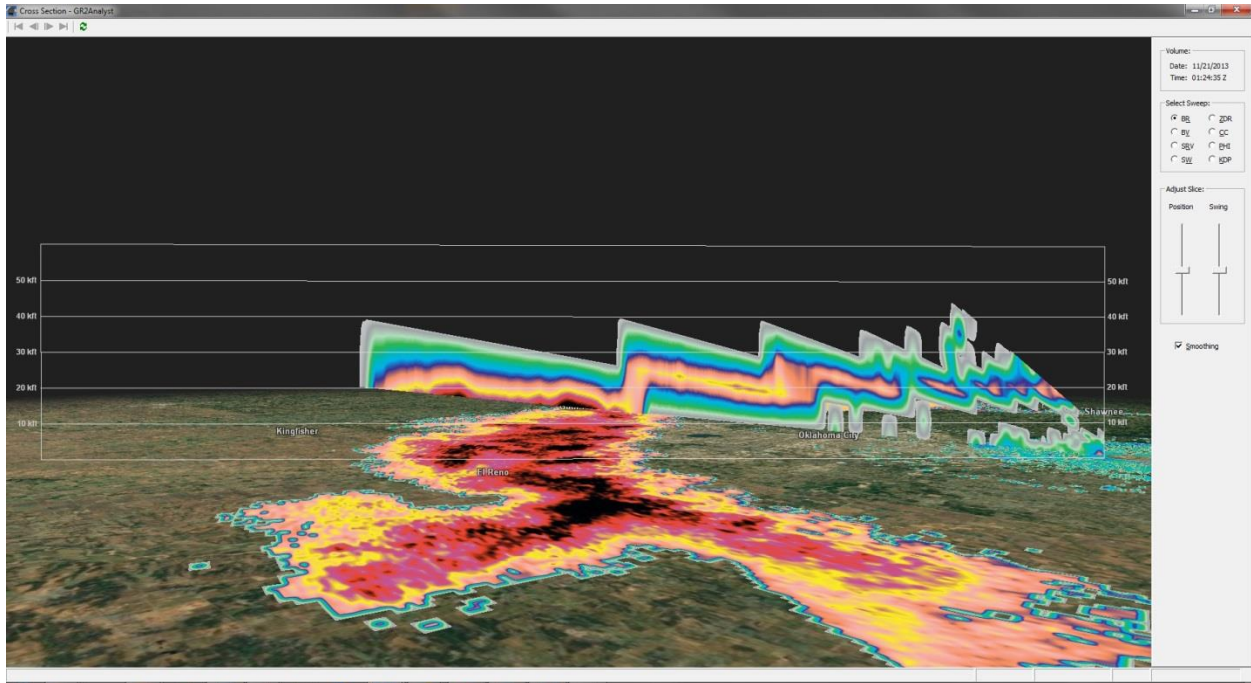
Fig. 3.3: Pseudo-RHI of reflectivity of nonprecipitating clouds placed on the horizontal projection of the radar cloud echo.
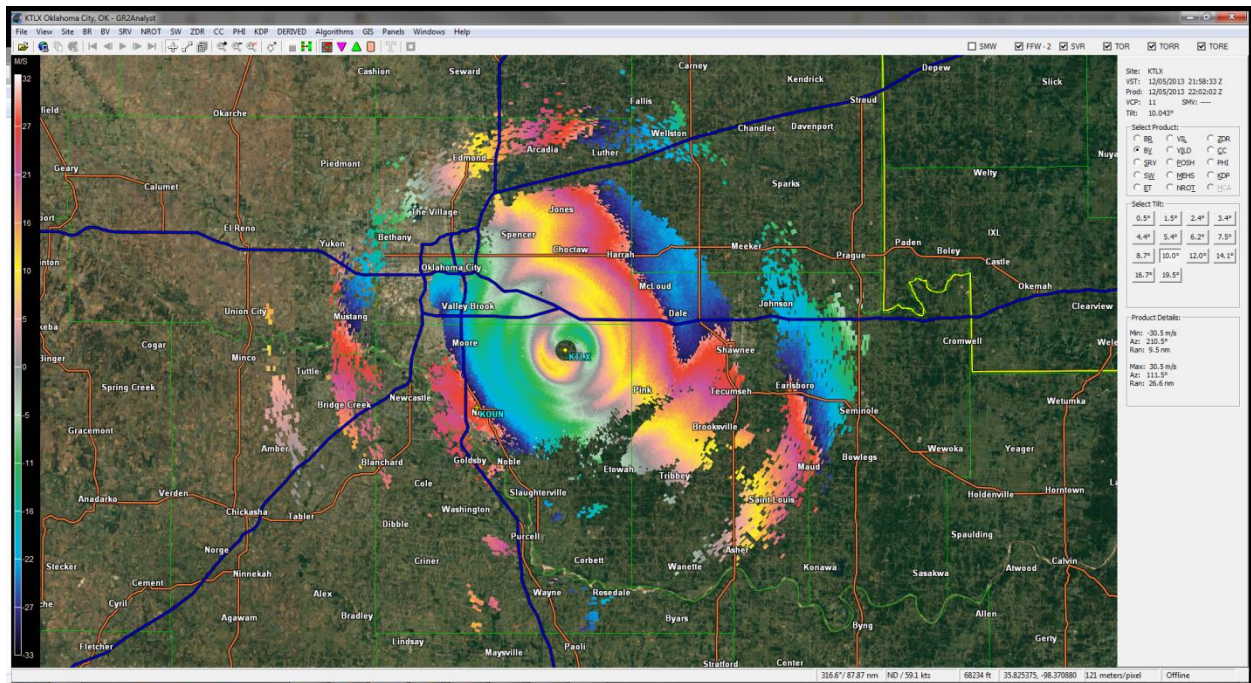
Fig. 3.4: Doppler velocity PPI collected with KTLX on 12/05/2013 at 2202 UTC at an elevation of 10°.
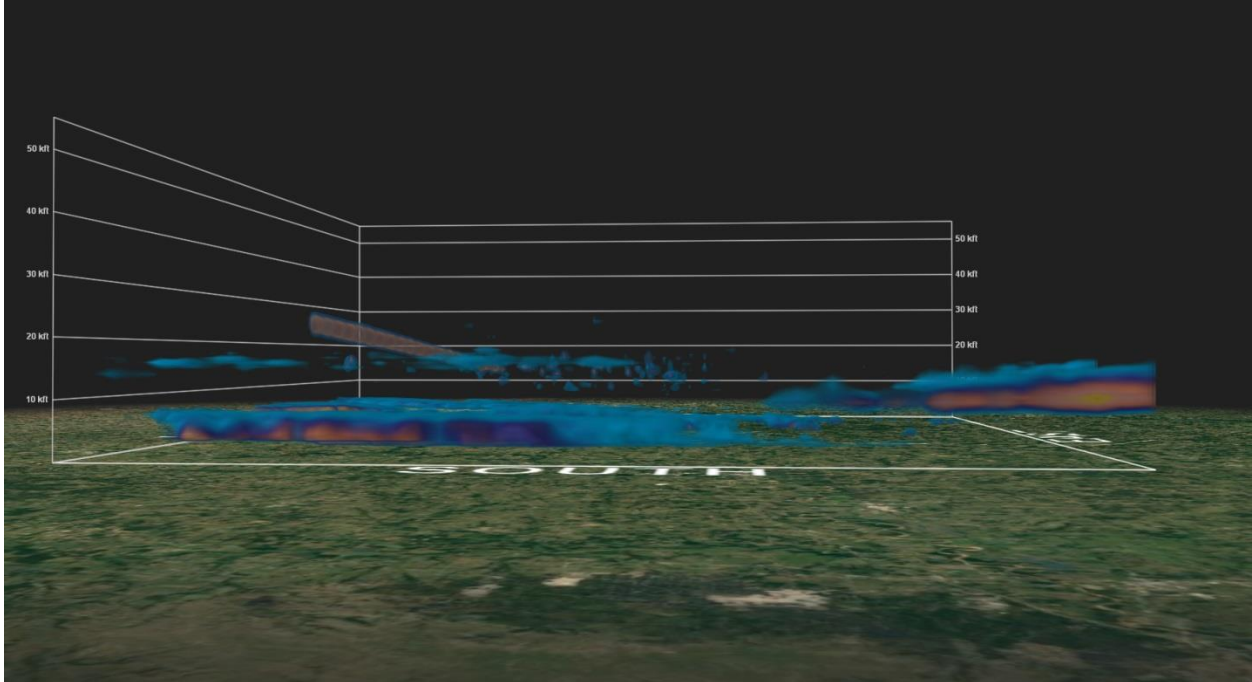
Fig. 3.5: 3D reflectivity field of the case in Fig. 3.4.

A Doppler velocity PPI of more complicated cloud structure is shown in Fig. 3.4. One can see two layers of echo; the second layer seen as two semi-circles in the north-west and south-east directions. A 3D radar image of this case is shown in Fig. 3.5. One can see the two cloud layers and the layers' heights can be obtained. Some openings are also seen in the image but one should keep in mind that these openings are from "radar point of view", so some light clouds could be present in the "radar openings".

a. Methods and challenges of 3D imaging of Level-II radar data

As previously discussed, there are many advantages and benefits of examining cloud structures in 3D using Level-II radar data. As the plots in Fig. 3.2, Fig. 3.3, and Fig. 3.5 also demonstrate, visualizing the data in 3D can reveal details of the cloud structures (such as multiple layers, non-precipitating layers above precipitating layers, the overall thickness of the layer, etc.) that otherwise may be missed by using the more traditional PPI and RHI plots alone.

Currently in this research, two primary methods have been experimented with to generate 3D images of cloud data sets using Level-II radar data (using both operational VCPs and experimental / higher max elevation angle VCPs, such as VCP20 with a maximum elevation angle of 40°): GR2 Analyst as used in generating Fig. 3.2, Fig. 3.3, and Fig. 3.5, and Matlab is used in generating the sample plot of spectrum width shown in Fig. 3.6 below.

14
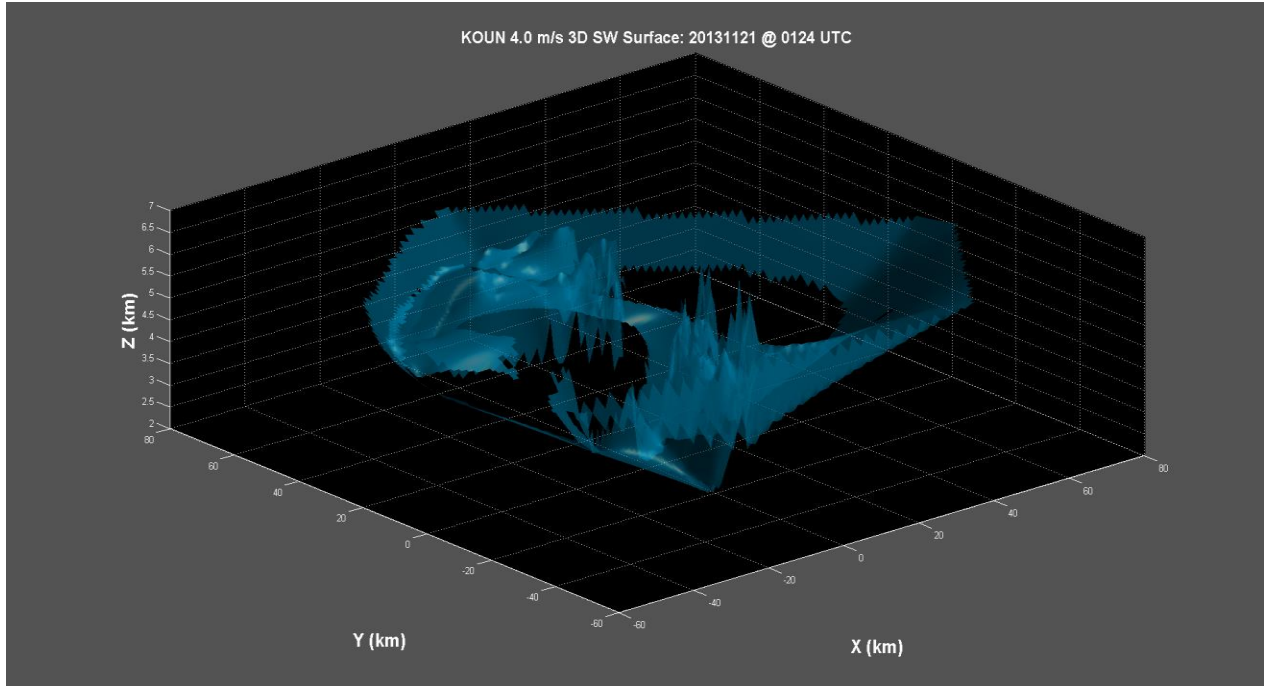
Fig. 3.6: 3D isosurface plot of spectrum width showing the 4.0 m/s contour, with the radar site at the center of the plot (X, Y = 0.0 km). The radar data used were from KOUN on 21 November 2013 at 0124 UTC. This particular contour of spectrum width is examined since this value is taken to be the lower threshold for severe turbulence. Width values equal to or greater than 4.0 m/s indicate turbulence that can be very hazardous to aircraft passing through those areas, especially during takeoff and landing.

While the method of using Matlab to generate 3D plots of cloud data is still undergoing testing and examination to determine the optimal technique to employ, the experimentation up to this point has found the following general procedure to be relatively stable in generating 3D isosurface plots such as that shown in Fig. 3.6:

1. For a given date and time at a given radar site, ingest the Level-II radar data into Matlab.
2. Using the spherical coordinate range (r), azimuth (θ), and elevation (φ) data at each tilt in the VCP, convert the data into rectangular coordinates (X, Y, Z) by accounting for the inherent π/2 offset in Matlab in the azimuthal direction as $\theta_m = \pi/2 - \theta$, and then using the following equations:
   a. $X = r \cos(\varphi) \cos(\theta_m)$
   b. $Y = r \cos(\varphi) \sin(\theta_m)$
   c. $Z = r \sin(\varphi) + \dfrac{r^2}{2\,IR\,R_E} + Z_{offset};$

Where IR is the standard refractive index of 1.21, R_E is the radius of the Earth (6371 km), and Z_{offset} is the height offset needed – either the height of the radar dish above ground level (AGL)

for the given site if Z in km AGL is desired, or the height of the dish plus the site's elevation above mean sea level (MSL) if Z in km MSL is desired.

3. For the radar variable of interest (reflectivity, velocity, spectrum width, differential reflectivity, correlation coefficient, etc.), select a value to contour (e.g. -5.0 dBZ for reflectivity, 4.0 m/s for width, etc.).
4. Using that value, and the given variable's field at each tilt, filter the X, Y, and Z coordinate data based on which values match the criteria.
5. Using now the filtered arrays of X, Y, and Z coordinates, generate the 3D isosurface image of the coordinates using one of Matlab's built-in interpolation and plotting algorithms.
6. Color, shade, and smooth the resultant surface accordingly based on the selected value.

Note that the transformation from spherical to rectangular coordinates is done so that the heights of various features in the isosurface can be more easily determined and visualized. The process for generating the 3D images in GR2 Analyst is a bit more straightforward in that one need only load the desired Level-II data file into the software interface, and then use its built-in volume explorer utility to instantly generate the 3D plot.

Each method has its advantages and limitations. GR2 is much faster and direct relative to the Matlab approach in that a plot can be generated with relatively few steps, and multiple values of the variable (such as reflectivity) contoured can be very easily shown and shaded in on the same plot. This allows for a better idea of the internal structure of the clouds, as well as makes detecting multiple layers much easier. However, it is not possible to automate and fully customize how GR2 generates its plots. For example, currently the only variables useful to cloud analyses available to plot in its volume explorer tool are the base variables (reflectivity, Doppler velocity, spectrum and width).

Matlab, on the other hand, is very easy to automate to produce 3D images from multiple volume scans and of multiple variables (including dual polarization variables) at multiple values. This method can save lots of time and effort overall. However, due mainly to the sparsity of data between the elevation tilts, Matlab's interpolation and smoothing algorithms sometimes perform erratically in connecting the data from the adjacent sweeps, thus limiting its ability to properly show multiple cloud layers and complex structures within the cloud layers. Furthermore, the Matlab algorithms and 3D imaging routines can be very computationally expensive, especially when attempting to overlay multiple values of the same variable, or overlay multiple variables on the same 3D plot. The research into optimizing the Matlab technique is ongoing, and improvements are being made accordingly. Overall, the recommendation is to use whichever technique suits the user's accuracy and time constraint needs most closely.

b. IBM 3D visualization of weather objects

3D imaging is currently one of the main topics in radar meteorology. Radar data displayed in 3D presents the data more in its native state (i.e. in the atmosphere) and with animation, these images quickly allow the user to see the weather evolve over time (i.e., time becomes the fourth dimension). Many software packages are capable of presenting weather objects in 3D, e.g. GR2, WDSS-II, NCAR Graphics, IBM-weather, RASSIN, and the Matlab tool described in the previous sections. 3D imageries eliminate the need to evaluate numerous traditional 2D images (such as PPI plots); such a representation saves time, and better represents atmospheric phenomena.

It is clear that various users need various 3D representations of data; for instance, the forecasters need a high resolution and highly detailed presentation of data, whereas the general public primarily needs to see a general representation of the weather. Cloud data are meant to be used by modelers and pilots, so they should be presented with a high spatial resolution that should also allow showing results of data processing (e.g., severe weather phenomena) and data obtained from other sources (e.g., temperature profiles from radiosondes or models).

An example of IBM-weather imagery is shown in Fig. 3.7 where clouds are shown with white-gray colors and regions of stronger reflectivity are shown with the light blue color. This image contains also a map of precipitation that is placed on the horizontal plane and a wind field near the ground shown with colored arrows. Meteorologists would like to see the inner structures of the thunderstorms, so this image is not capable of satisfying all their needs, and thus a more interactive 3D representation is desired.
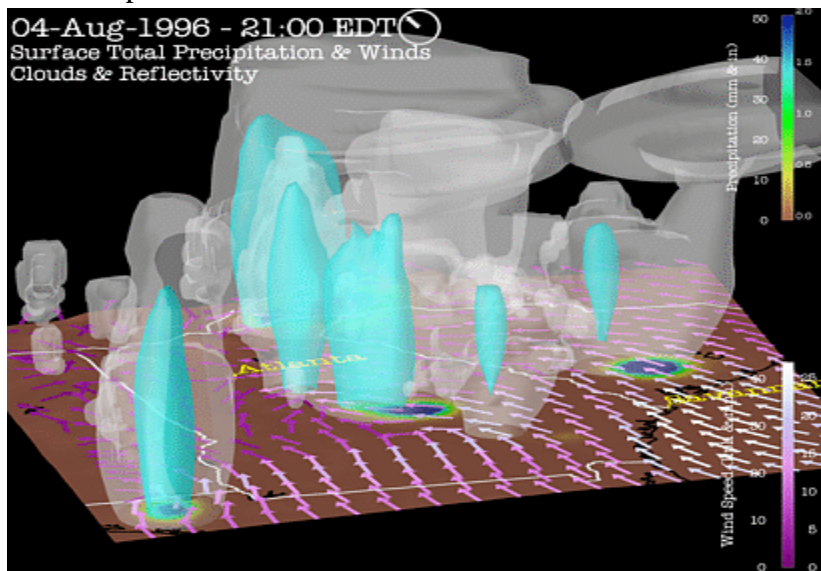
Fig. 3.7: 3D Representation of reflectivity (bluish) and clouds (white-gray) with the precipitation amount at ground level and the winds near ground level shown.

Another possible data presentation from the IBM-weather is shown in Fig. 3.8. The clouds and precipitation are shown with shaded white color and other atmospheric parameters (precipitation, temperature, pressure, and winds) are shown with different colors and contours. This image also demonstrates a possible presentation of a 3D "read-out" tool with vertical sticks with attached colored arrows. The 3D "read-out" tool is different from the one for a 2D image: a 3D image is represented on a 2D plane by using the stereographic projection. To create a 3D "read-out" tool, there should be a mechanism of navigating through the stereographic volume. Fig. 3.8 shows one of the possible solutions.
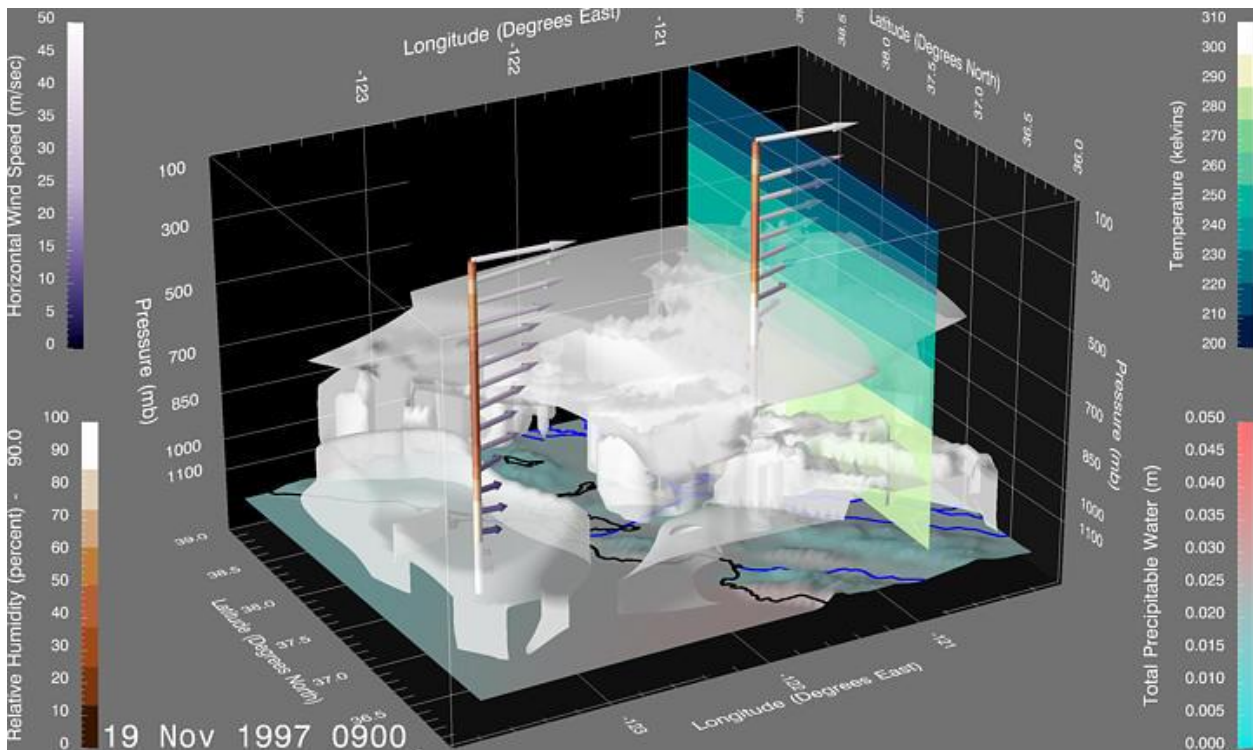
Fig. 3.8: Multiple parameters shown in 3D.

To represent multi-parameter radar data (e.g., Z, V, Z_{DR}, and others), many techniques can be explored; these are isomorphic colormaps, colored contours, segmented colormaps, isosurfaces, and volume rendering, among others. 3D "read-out" tools and presentations of critical weather features require interactivity. Transferring data to the end users requires effective methods of data compression to reduce download time. To show 3D weather data on the web, simplified versions of 3D imageries should be developed. These issues are on the focus of programmers that develop 3D imaging of weather objects.

4. The base radar products in clouds

Reflectivity factor Z, the Doppler velocity V, and velocity spectrum width W are the base radar variables measured with the WSR-88Ds. The goal of this section is to demonstrate the capability of the WSR-88D to measure and map Z, V, and W within clouds. It is also demonstrated the need of a large unambiguous velocity for accurate measurements of V and W. In the WSR-88D, Z and V are presented in range gates having signal-to-noise ratio (SNR) larger than 2 dB. Because spectrum width cannot be accurately measured at such SNR, W fields are presented for a SNR ≥ 7 dB.

Fig. 4.1 presents an RHI of nonprecipitating clouds along with precipitation echoes at ranges beyond 70 km. One can see that clouds are not-homogeneous, so convection plays a role in such stratiform clouds. The maximal tops are observed near the radar and reach 8 km. The upper cloud boundary lowers with range, most likely due to weakening detectability. One can see that the upper cloud boundary varies by about 1 km; for instance, the echo top at range of about 42 km is lower than 7 km. The cloud lower bound is minimal at the close ranges also.

The panel of Doppler velocity (Fig. 4.1) exhibits aliasing. Thus, a wide Nyquist interval is desirable for cloud observations. A wide Nyquist interval makes the distance of the observations shorter. At the maximal WSR-88D PRF of 1280 Hz, the unambiguous range is 117 km, which is not too large for all possible situations. This distance is probably sufficient for the terminal airport area (50 - 60 km from an airport) that can be monitored for cloud existence, and cloud tops and lower bounds. But a distance of 117 km could be not as large for cloud modelers in situations with thick clouds that can be observed at much longer ranges at lower PRFs. So various VCPs can be run to fulfill the different needs.

The spectrum width field in Fig. 4.1 exhibits high W values in the cloud at close ranges from radar. This is an artifact of ground clutter contamination. The ground clutter filter suppresses reflections from the ground but in areas with cloud echoes, the filter cannot completely remove clutter with low Doppler velocity so that even small leftovers of ground clutter can give the spectrum width a high bias. These enhanced W values are due to contaminations from antenna side lobes that were not completely suppressed by the ground clutter filter. One can see some contaminations from ground clutter in the V and W fields in a form of almost vertical strips. So one should be cautious in interpreting W radar fields at close distances where contamination from ground clutter is likely. Values of W beyond 80 km (Fig. 4.1) in precipitation are very high. This is due to mixing of precipitation with atmospheric biota. Such features are not analyzed herein because they do not occur in clouds.
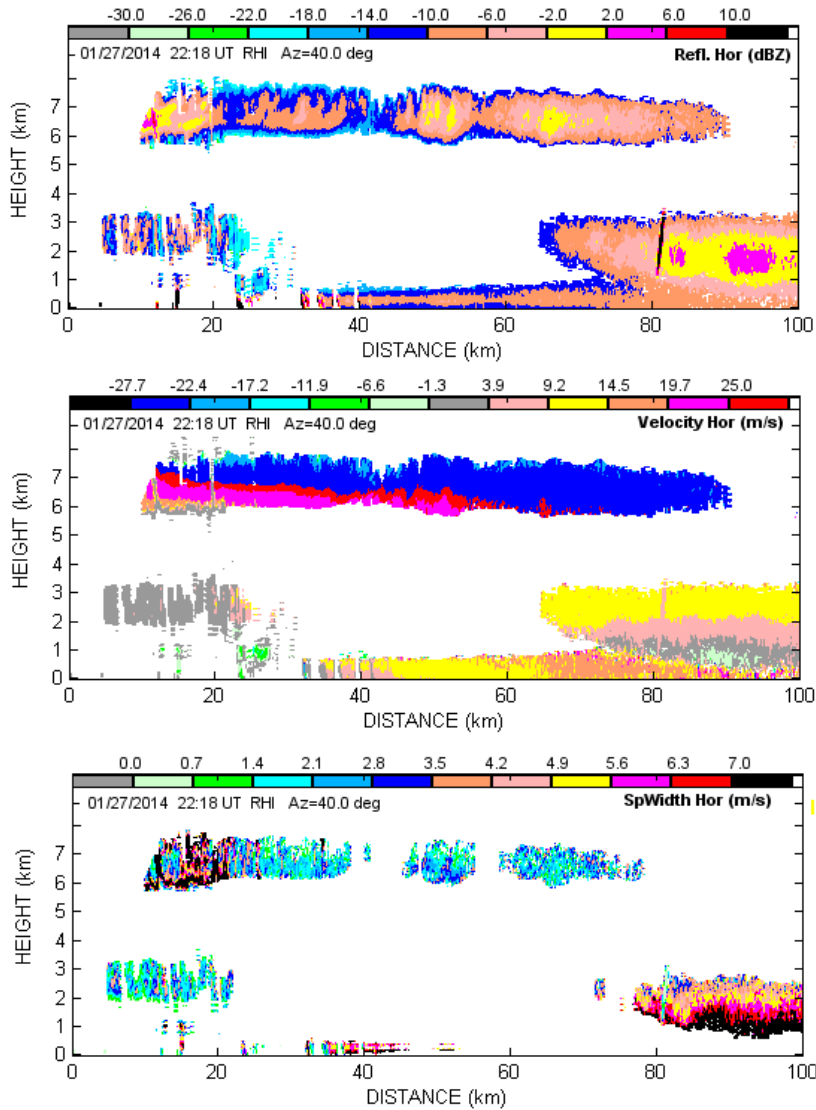
Fig. 4.1: RHI of Z, V, and W collected with KOUN on 27 January 2014 at 2218 UTC at an azimuth of 40°.

Fig. 4.2 exemplifies situations with non-uniform clouds; the cloud tops are highly variable. The lower cloud bounds can be obtained with better certainty, but still not at any range. The W field (left panel) shows a layer of enhanced width created by the wind shear at the height of about 4.5 km. The echo located below 1 km is from Bragg scatter. Such echoes are also seen in the right panels at the heights up to 2.5 km. The right panels in Fig. 4.2 is an example of two-layer clouds: the lower layer is at altitudes between about 3.5 and 5.5 km and the upper clouds are located above 6.5 km. Multi-layered cloud structures are of interest for aviation, meteorologists, and cloud physicists. The velocity field in the right panel allows obtaining the wind characteristics almost at all heights up to 9 km. Such situations could be of interest for

20

meteorologists because it is possible to obtain environmental winds at high altitudes. Such data could be complementary to data from the wind profilers.
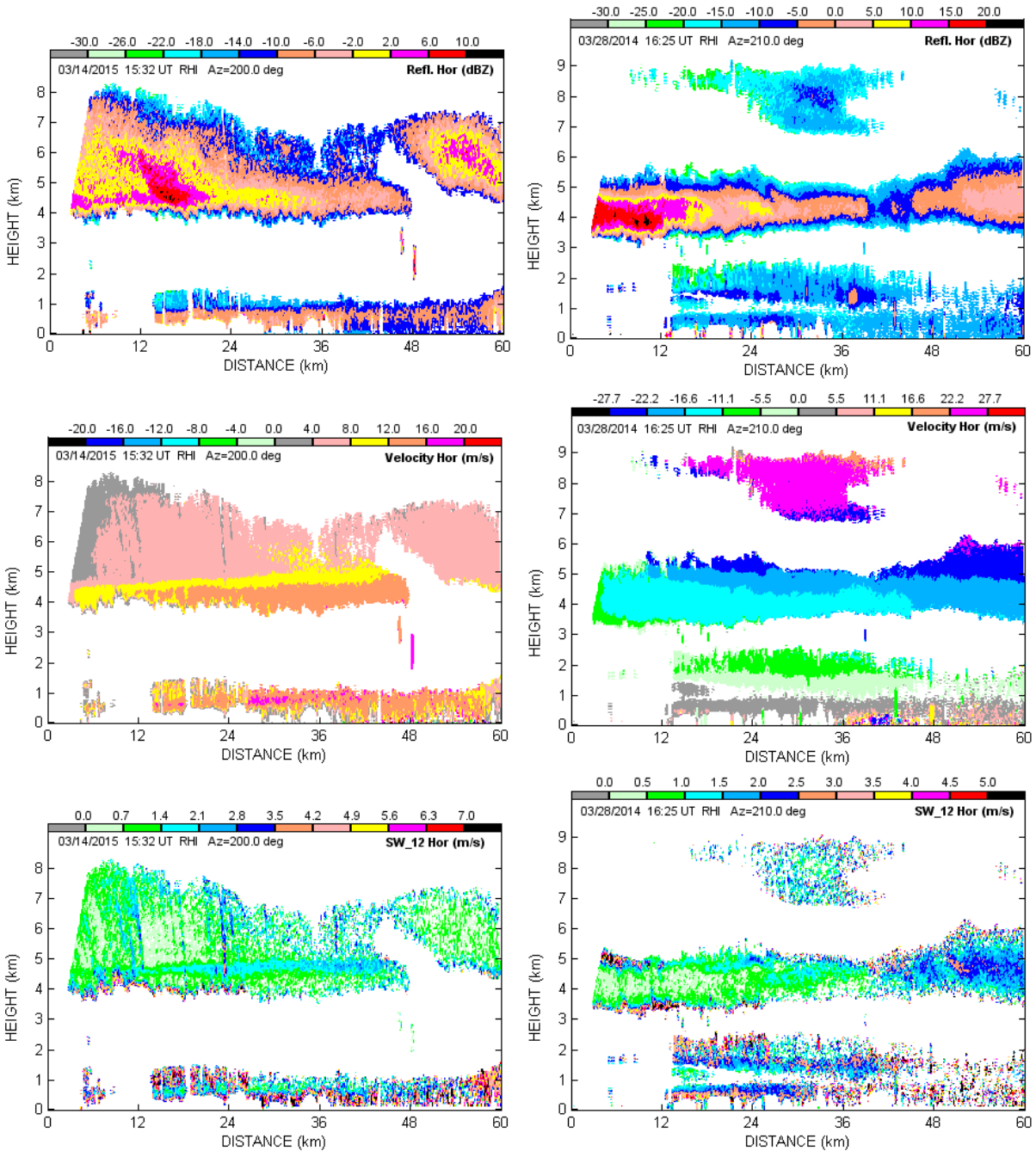
Fig. 4.2 (left column): RHI of Z, V, and W collected with KOUN on 14 March 2015 at 1532 UTC at an azimuth of 200°. (right column): Same as in the left column but on 28 March 2013 at 1625 UTC at an azimuth of 210°.

For additional reference, 3D images of Z, V, and W are provided in Fig. 4.3, Fig. 4.4, Fig. 4.5, and Fig. 4.6 for the case of the left column of Fig. 4.2 (14 March 2015), but at the time of 1515 UTC instead due to the current availability of Level-II KOUN data for certain times. Also for that same reason, 3D imagery is not currently available for the case of the right column of Fig. 4.2 or for Fig. 4.1. Note that the color scales used in these 3D plots are the same as those used in Fig. 4.2.
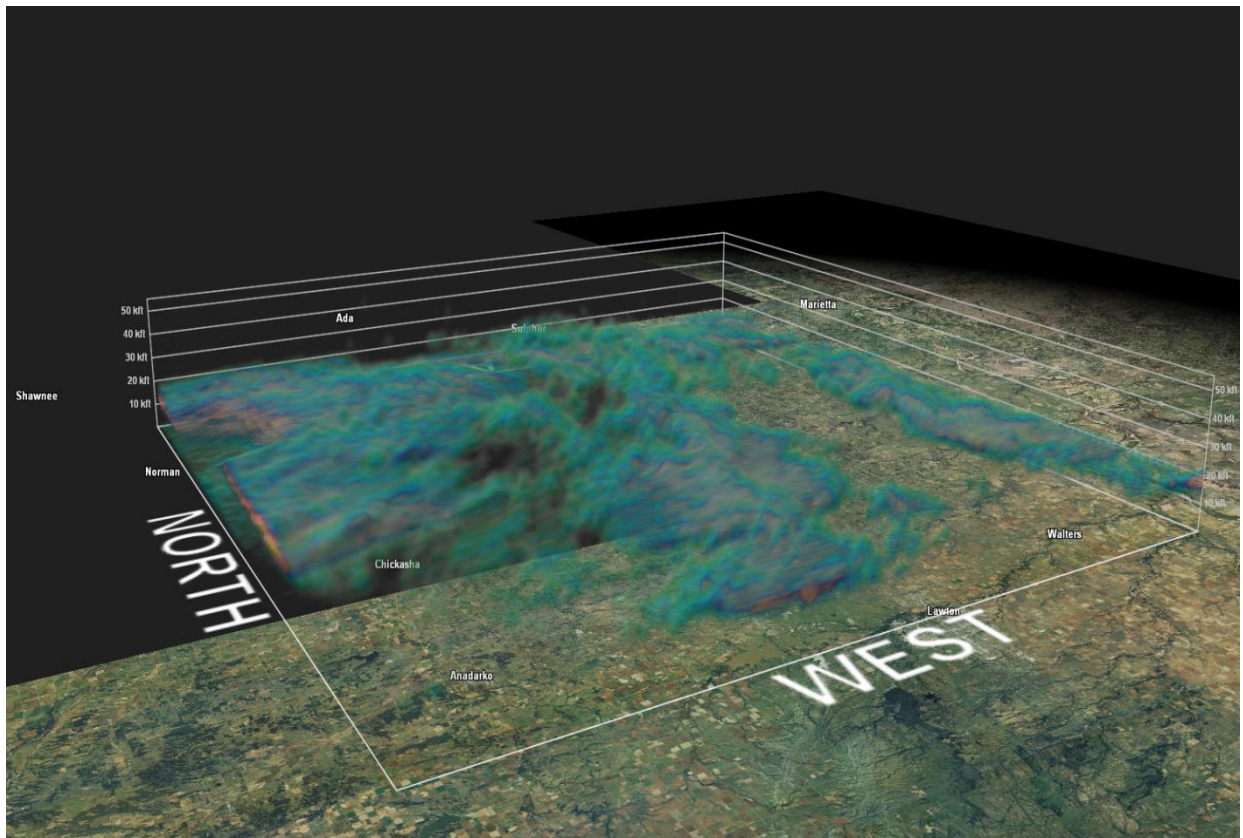
Fig. 4.3: 3D Z field from KOUN from 14 March 2015 at 1515 UTC taken from the same general area as the plots from Fig. 4.2 (left panel). This plot shows the overall cloud coverage in the area in reference to the KOUN radar site.
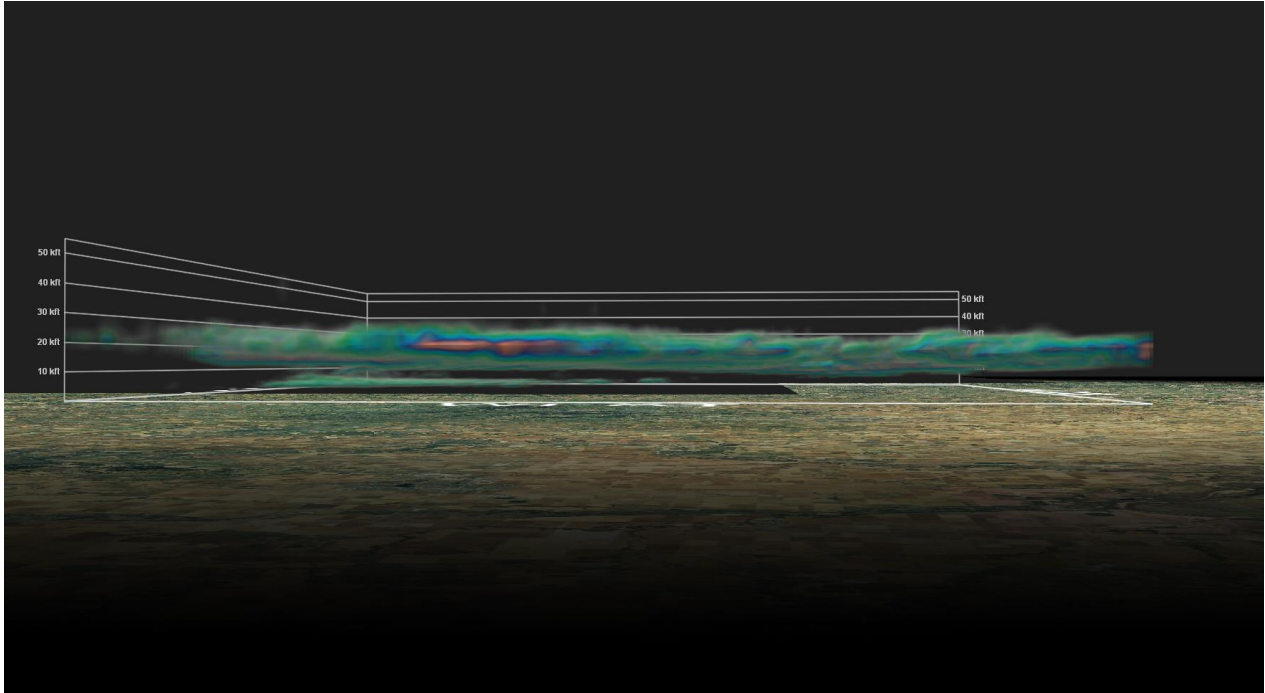
Fig. 4.4: Additional 3D Z field for the case of Fig. 4.3. The perspective of this plot is close to that of the RHI plots in the left panel of Fig. 4.2, and shows that multiple cloud layers are, in fact, present.
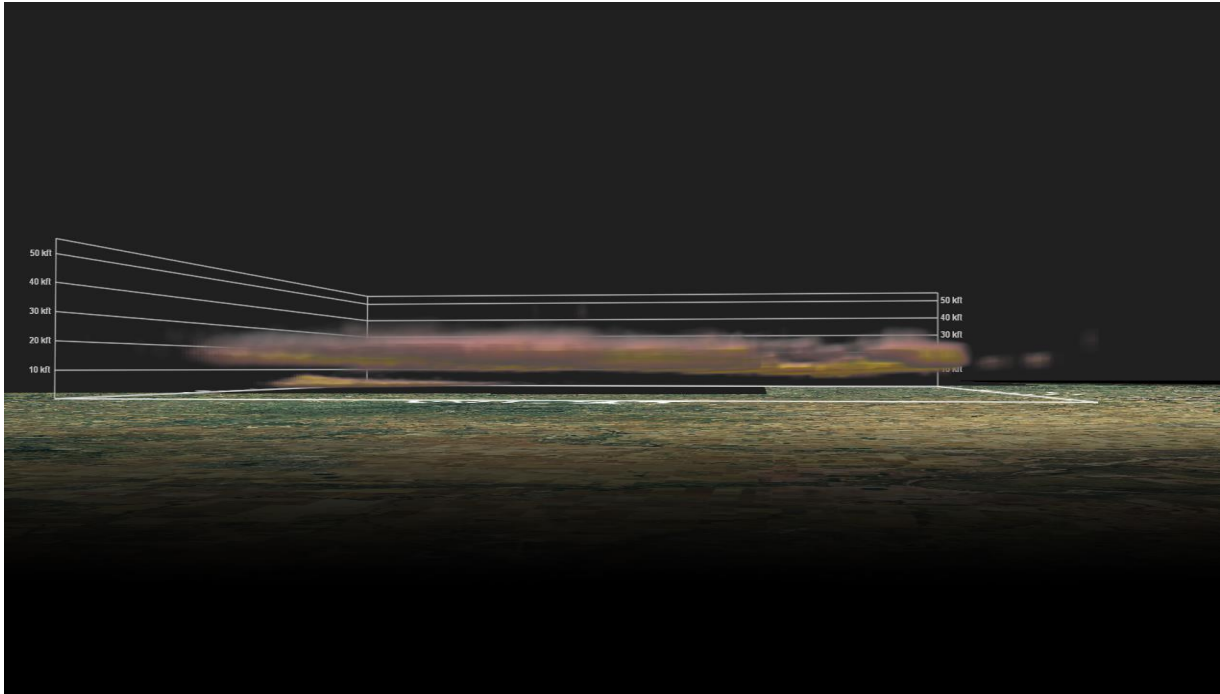
Fig. 4.5: 3D V field for the case of Fig. 4.3.
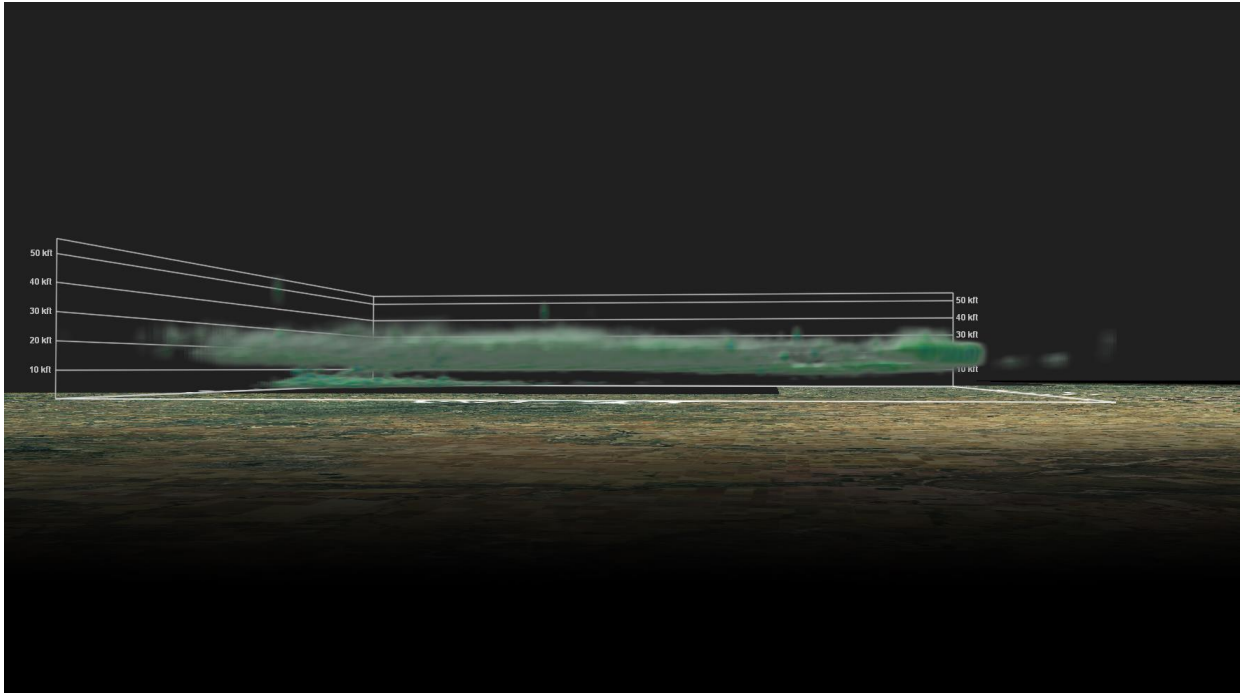
Fig. 4.6: 3D W field for the case of Fig. 4.3. In this case, there was very little severe turbulence present since most of the contours show values below 4.0 m/s.

5. Detecting strong wind shears and turbulence in clouds

Measurement of wind shear and turbulence is of both practical and theoretical interest. The rate at which turbulent energy dissipates as heat depends on the intensity of turbulence within the inertial subrange, and the safety of flight depends on avoiding regions of strong wind shear and intense turbulence. Weather radars have been used for these purposes for a long time (e.g., Atlas 1964; Gossard and Strauch 1983, Mahapatra 1999, Doviak and Zrnić 2006). Vertical profiles of wind and turbulence in the clear atmosphere are obtained with long wavelength (i.e., λ > 30 cm) radar wind profilers (Woodman and Guillen 1974; Hocking 1983, 1988; Holloway et al. 1996), but the measurements strictly apply above the radar's height. Short wavelength (i.e., λ $\leq$ 10 cm) weather radars typically do not have the capability to reliably measure shear and turbulence in the clear air, but can make measurements over vast regions of precipitation and clouds (Doviak and Zrnić 2006; Melnikov et al. 2007).

Turbulence in clouds and precipitation can be estimated with weather radars by measuring the spatial correlation function of the mean Doppler velocity v_m (e.g., Brewster and Zrnic 1986) or the velocity spectrum width W (Doviak and Zrnic 2006, section 10). The wind shear and turbulence in the radar volume are two major contributors to W. Børresen (1971), conducting radar observations in stratiform precipitation at slant soundings, concluded that vertical shear cannot be neglected in determining turbulence. He used data collected with 2° elevation increments (i.e., twice the beam-width) at relatively close ranges (i.e., 12 to 17.5 km),

24

and expressed concern that such relatively large elevation increments (i.e., about 500 m in height) were too coarse for accurate measurements of shear and turbulence. As shown by Chapman and Browning (2001), the correct separation of shear and turbulent contributions to $\hat{\sigma}_v$ is a necessary step in measuring turbulence. The shear and turbulent contributions can be separated using the approach of Melnikov and Doviak (2009). Our goal herein is mapping large W in clouds to identify areas that can pose threats for aircraft.

Examples of layers of very high W are shown in Fig. 5.1 for stratiform clouds. The W field in the left column exhibits two layers of high W located at heights of about 5.5 and 7.5 km. The maximal W in the lower layer reaches 6 m s^{-1} and in the upper layer, exceeds 10 m s^{-1}.
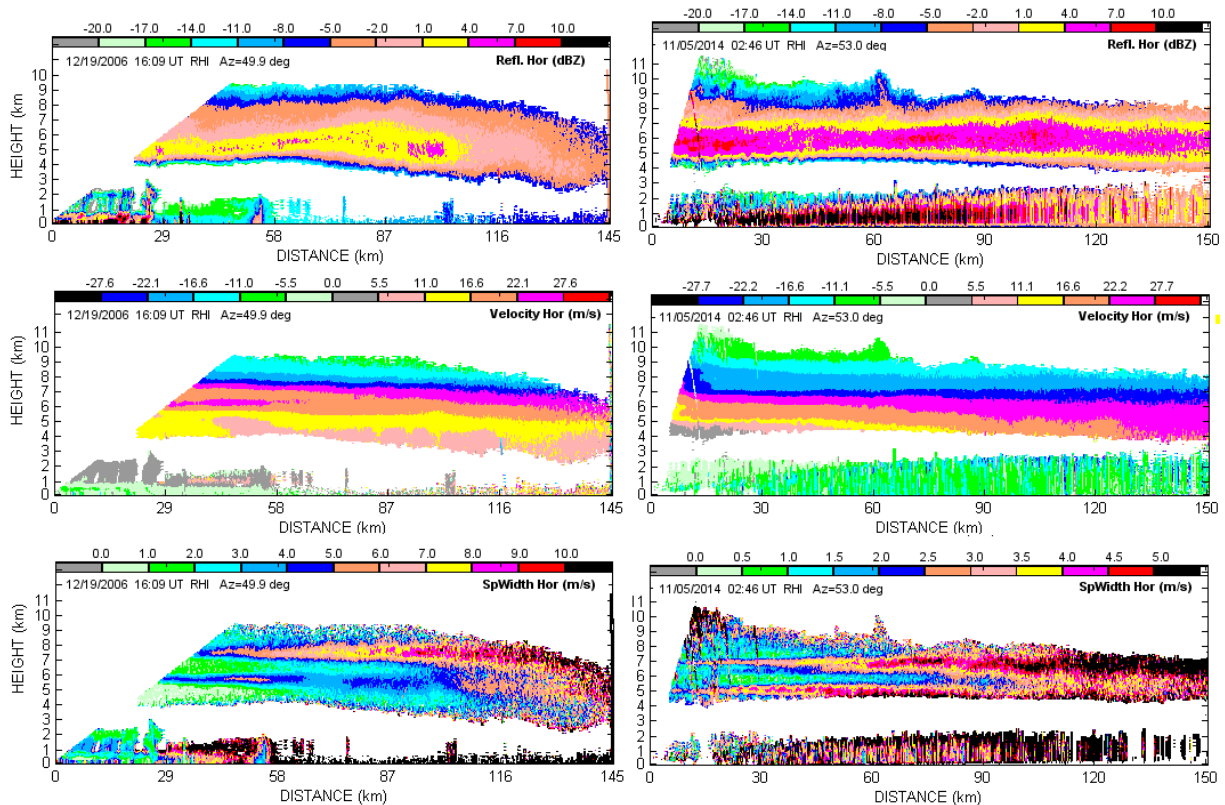
Fig. 5.1 (left column): RHI of reflectivity, Doppler velocity, and spectrum width collected on 19 Dec 2006 at 1609 UTC at an azimuth of 50°. (right column): same as in the left column but for 5 November 2014 at 0246 UTC. The radar site used is WSR-88D KOUN.

In aviation meteorology, W data ≥ 4 m s^{-1} are used to indicate the potential for turbulence to cause a hazard to aircraft and/or its crew and passengers (Lee 1977). A threshold of 4 m s^{-1} is used because it is accepted as an indicator of turbulence possibly hazardous to aircraft and/or its crew (Lee 1977, Evans 1985). Because W is a function of range and radar parameters, even if turbulence is homogeneous and has an outer scale larger than the dimensions of radar volume, a better metric to assess potential hazard to safe flight is the turbulent energy dissipation rate; this metric can be derived from W (Melnikov and Doviak, 2009). The 4 m s^{-1} threshold corresponds

to a turbulent energy dissipation rate of about 1.6×10^{-2} m^2 s^{-3}, corresponding to moderate turbulence theory (Hocking and Mu, 1997; Table 2). In order to convert the turbulent dissipation rate to shocks to aircraft, information about certain parameters of the given aircraft is required, including weight, wing area, airspeed, and other factors.

An airplane's response to turbulence is mostly affected by the along-track gradients of the vertical wind (Proctor et al. 2002), a component typically not measured with airborne or ground-based weather radars. Nevertheless, good correlation between the variance of vertical and along-track wind components has been observed in strong convection (Hamilton and Proctor 2006a, b). Lee (1977), Bohne (1981), Meischner et al. (2001), and Cornman et al. (2003) found, in thunderstorm environments, strong correlation between aircraft shocks and large W measured by airborne and/or ground-based weather radars. We call W "large" if it equals or exceeds 4 m s^{-1}. It can be shown that turbulence hazards to safe flight can often be non-existent in stratiform precipitation, although Ws are large. On the other hand, stratiform weather can also harbor regions of large W that could be hazardous to safe flight.

Strong wind shears aloft poses little thread to aircrafts. The impact of shear can be minimized by adjusting the angle of attack. Strong shears in clouds can generate Kelvin-Helmholtz (K-H) waves with strong vertical velocity components that can shake aircrafts. Examples of K-H waves are shown in Fig. 5.2. One can see a wavy pattern in the W fields (two lower panels) at heights from 4 to 5 km at distances beyond 35 km.
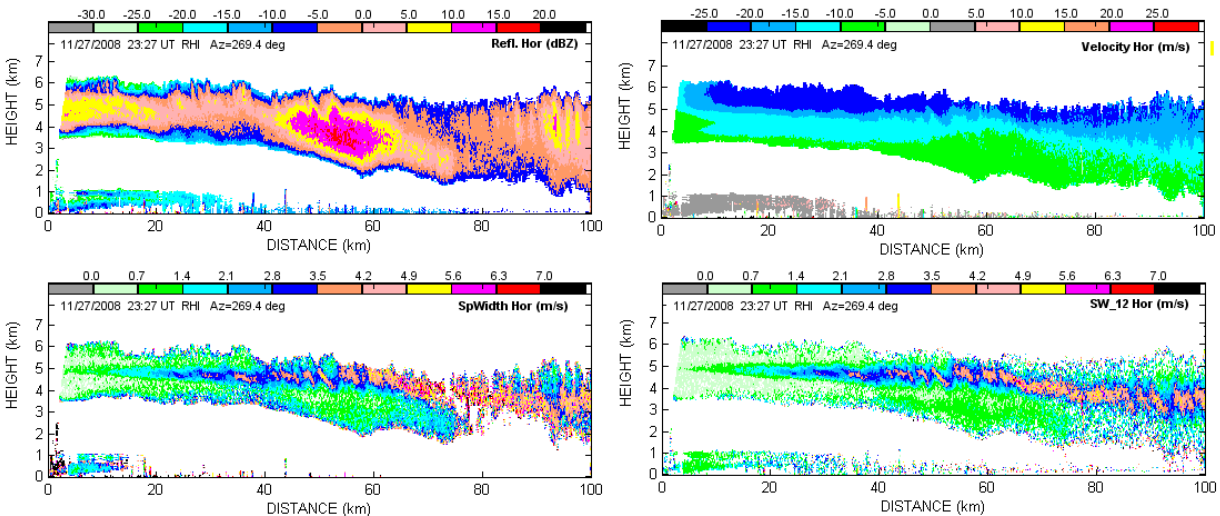
Fig. 5.2: RHI of reflectivity, Doppler velocity, and spectrum width collected on 27 November 2007 at 2327 UTC at an azimuth of 200°. The lower-right panel is the spectrum width calculated via the lag-1-2 algorithm.

The spectrum width is estimated in the WSR-88D by using so called lag-0-1 algorithm (the left W panel in Fig. 5.2), which is vulnerable to be impacted by system noise. Values of W are biased high at SNR < 15 dB, and this bias increases with decreasing SNR. To make this

impact smaller, the lag-1-2 algorithm has been applied to the data. The result is shown in the right lower panel in Fig. 5.2. One can see that the lag-1-2 algorithm provides a larger W image filling in some gaps produced by the lag-0-1 algorithm. The layer of enhanced W is clearly seen at all distances and we can say that large W values in the layer at distances 70 to 90 km (left W panel) are not due to low SNR, but are indeed due to the wind shear and K-H waves located at a height of about 5 km at distances beyond 30 km from radar.

One more case with K-H waves is shown in Fig. 5.3. K-H waves are clearly seen in the left W panel at a height of about 4 km at distances within 30 km from the radar. In this case, the lag-1-2 algorithm produces a pattern (right lower panel), where the K-H waves is difficult to recognize. So to identify the K-H waves, both W algorithms can be useful and it would be informative to study the difference between the algorithms in various situations.
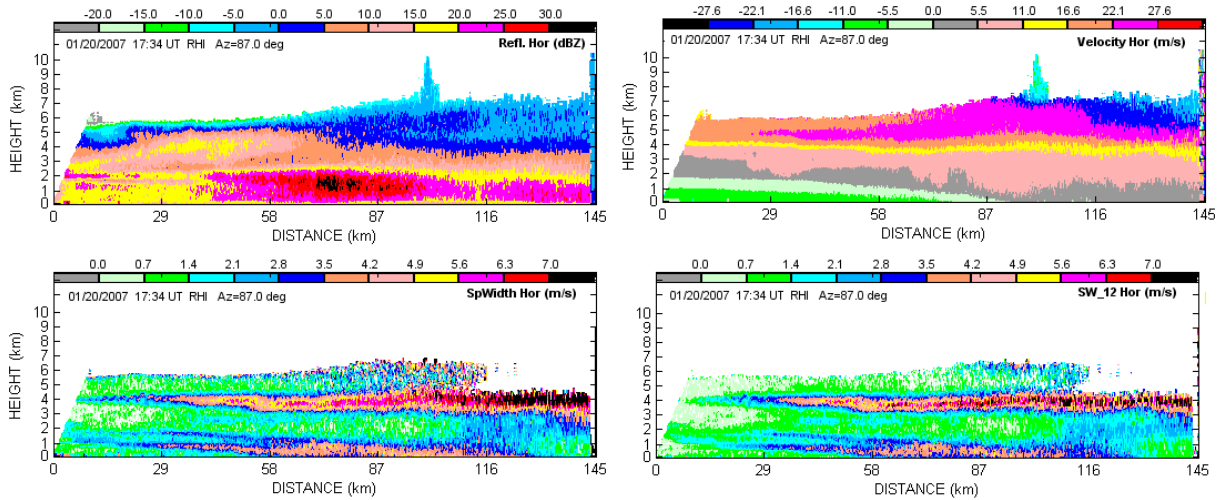
Fig. 5.3: RHI of reflectivity, Doppler velocity, and spectrum width collected on 20 January 2007 at 1734 UTC at an azimuth of 87°. The lower-right panel is the spectrum width calculated via the lag 1-2 algorithm.

Sometimes K-H waves manifest themselves as a patchy strip of enhanced spectrum width. An example is shown inFig. 5.4, collected in nonprecipitating clouds, where a slant strip of enhanced spectrum width is seen at heights of 8-10 km (the right panel). At distances from about 15 to 30 km, a wavy pattern of K-H waves is noticeable. The strip exhibits a patchy pattern beyond 30 km that could be caused by K-H waves. Enhanced shocks to aircraft can be expected in such areas.
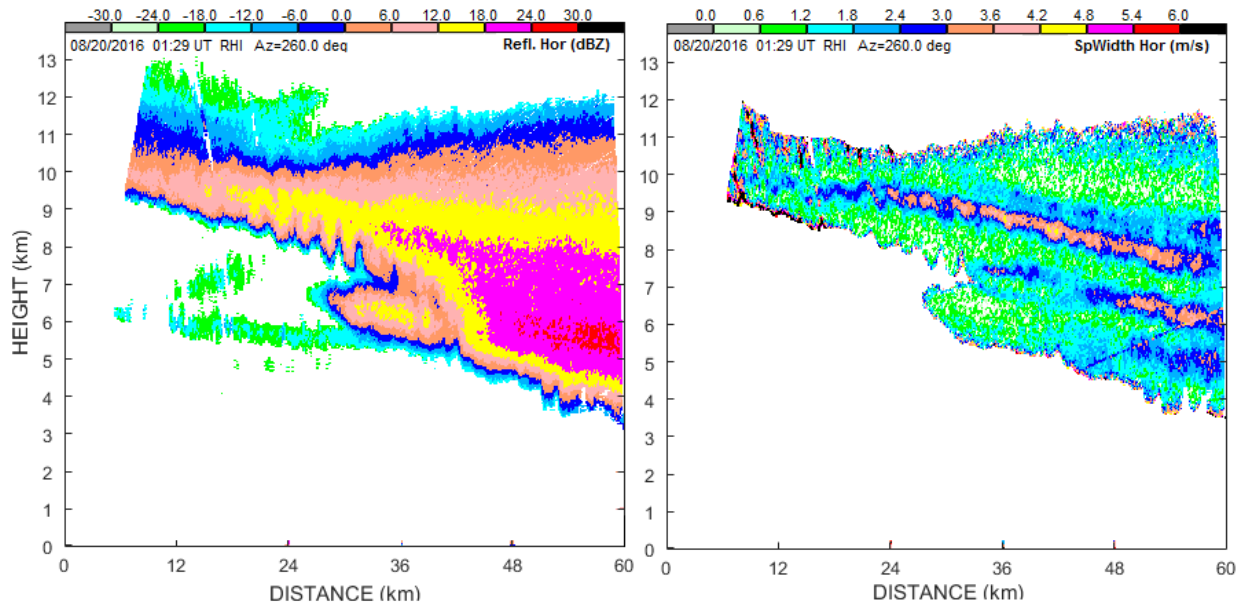
Fig. 5.4: RHI of reflectivity (left) and spectrum width (right) collected on 20 August 2016 at 0129 UTC at an azimuth of 260°.

6. Transitions from clouds to rain

The transition from nonprecipitating clouds to precipitation is pooarly understood (Stephens and Kummerow 2007). Any information about this transition can be useful and the WSR-88Ds can be used for that. Cloud growth can be monitored with radar, and examples of rainfall beginning are shown in Fig. 6.1). Cloud radars are not expected to perform well in precipitation, so observations at 10-cm wavelengths are especially advantageous for studies of water accumulation in clouds and the transition to rain.

One of the long-standing problems in atmospheric research is the understanding of the physical mechanisms leading to the onset of precipitation in shallow warm clouds (Beard and Ochs 1993). Examples of precipitation that occurred in small areas are presented in Fig. 6.1. The WSR-88Ds cannot be used to monitor transitioning from clouds to precipitation using the current operational VCPs. To accomplish such a mission, the radar update time should be about 1 min or shorter, and that time cannot be reached with the WSR-88Ds. Phased array weather radar could serve such purposes.
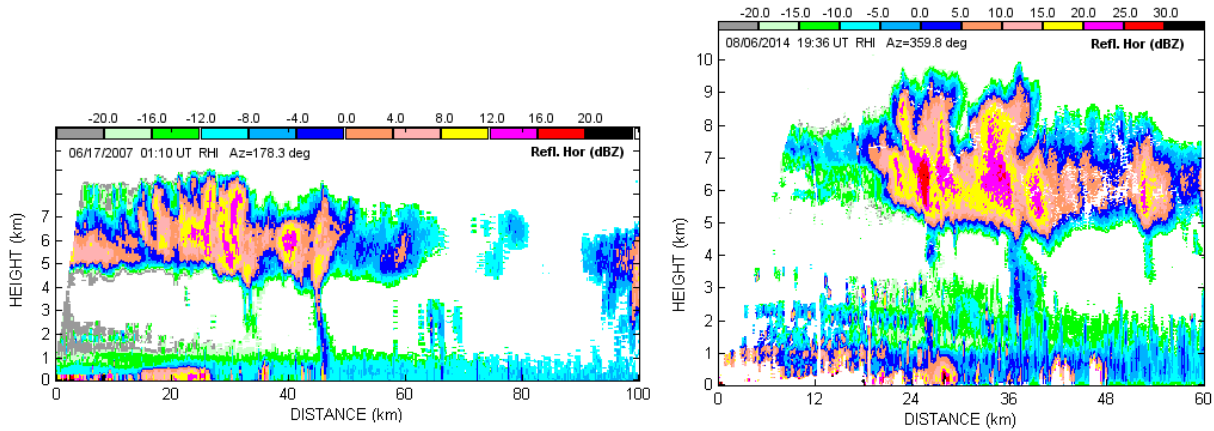
Fig. 6.1: RHIs collected with KOUN on 17 June 2007 at 0110 UTC (left) and 8 June 2014 at 1936 UTC (right) demonstrate spatially small rainfall amounts from mainly nonprecipitating clouds.

7. Utilization of polarimetric products in cloud observations

The WSR-88D is a polarimetric radar delivering differential reflectivity (Z_{DR}), correlation coefficient (CC or ρ_{hv}), and differential phase (Φ_{DP}). The latter parameter is useful in precipitation but its values are small in ice clouds, and thus are not analyzed in this study. Values of Z_{DR} and ρ_{hv} depend on the shape of cloud particles, and can be used in retrievals of particles parameters.

a. Clouds or atmospheric biota?

In warm seasons, radar echoes on cloudy days can emanate from clouds, and from flying insects and birds, which are frequently called atmospheric biota. Polarimetric data are extremely effective in distinguishing between echoes from weather and biota (e.g., Zrnic and Ryzhkov, 1999). It has been established that biota has Z_{DR} (CC) larger (smaller) than that from weather. In a reflectivity field, echoes from clouds and biota can look similar. An example is shown in Fig. 7.1 (left column), where clouds are located above 6 km. The echo at the height of $4.5 - 5$ km is from Bragg scatter and echoes below 4 km are from Bragg scatter and insects. This is concluded from corresponding Z_{DR} and CC fields. We can also conclude that the WSR-88D observes not only clouds with low Z_{DR}, but also Bragg scatter with low Z_{DR} that can be difficult to distinguish from cloud echoes. Values of CC in both clouds and Bragg scatter are high, so CC is also difficult to use for this distinction.
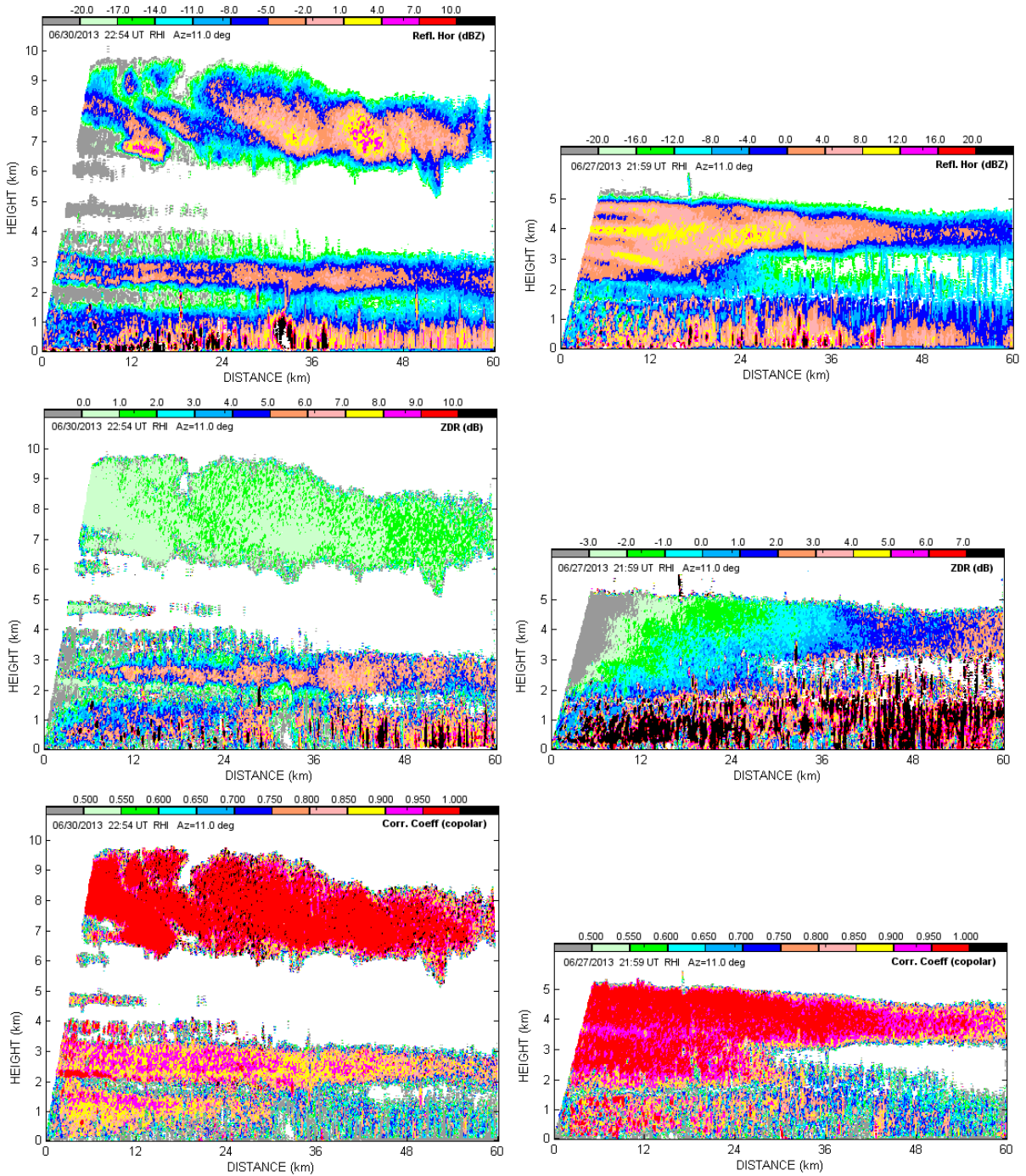
Fig. 7.1 (left column): RHI collected with KOUN on 30 June 2013 at 2254 UTC in an azimuth of 11°. (right column): Same as in the left column, but on 27 June 2013 at 2159 UTC in an azimuth of 11°.

Sometimes Z fields from insects appear as cloud echoes (Fig. 7.1, right column). High echo tops could cause the illusion of the presence of clouds. An analysis of the Z_{DR} field shows

that this feature is not a meteorological echo: Z_{DR} values become strongly negative at high antenna elevations. This feature indicates that the echo emanates from insects. The positive Z_{DR} at lower elevations have values similar to ones from clouds. Interestingly enough, the CC in the upper part of this echo has values close to weather values, so it is difficult to use CC for distinguishing this echo from biota.

b. Retrieving the shape of ice cloud particles using Z_{DR} and ρ_{hv} values

Values of Z_{DR} in ice clouds depend on the shapes, bulk ice density, and the orientation of fluttering cloud particles. Ice cloud particles of simple shapes are of solid ice, but particles of more complicated shapes contain intricately shaped ice crystals (e.g., dendrites, Pruppacher and Klett, 1997, chapter 10). For the latter particles, bulk ice density is introduced as the content of solid ice in a particle of visible sizes. Thus, bulk density varies from 0.93 g cm^{-3} for solid ice to values more than two orders of magnitude less.

The fluttering of scatterers affects their scattering properties. The intensity of flutter depends on the shapes and weight of ice cloud particles and on turbulence in clouds and varies in a large interval. The standard deviation σ_θ^2 in the canting angles is frequently used as a measure of flutter. Matrosov et al. (2005) found the intensity of flutter from 3° to 15°. Photographic measurements of Kajikawa (1976) indicated canting of 10° - 25°. Zikmunda and Vali (1972) found canting of rimed crystals to be mainly in an interval of 5° - 15°, but a few crystals exhibited canting of 75°. Radar data analyzed by Melnikov and Straka (2013) exhibited canting in a wide interval from 2° to 20°.

The impact of flutter can be seen from Fig. 7.2, which was generated at $\sigma_\theta = 1°$ (i.e. for almost horizontal particles), 5°, and 10° for two types of ice crystals - plates and columns. It is seen that Z_{DR} decreases with increasing flutter. The corresponding equations are placed to the Appendix. The maximal Z_{DR} are quite different for plates and columns: at weak flutter, they reach 10 dB for plates, and only 4 dB for columns. So we conclude that if measured Z_{DR} in clouds is larger than 4 dB, the scatterers have plate-like shapes.
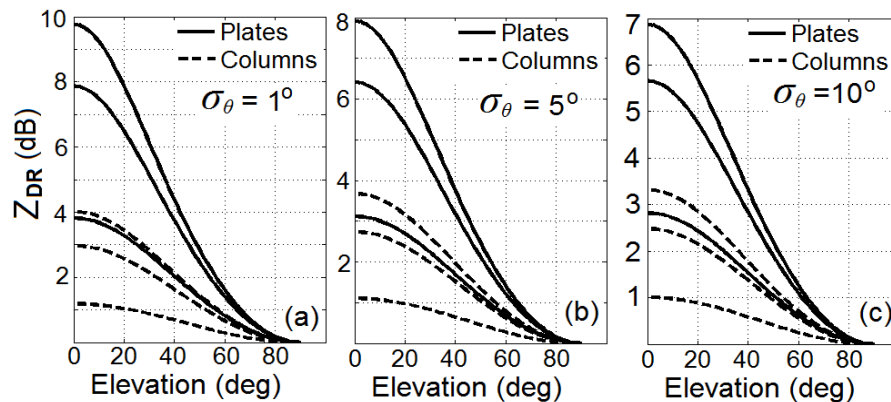
Fig. 7.2: Z_{DR} for plate-like and columnar ice crystals as a function of antenna elevation at various flutter intensities σ_θ.
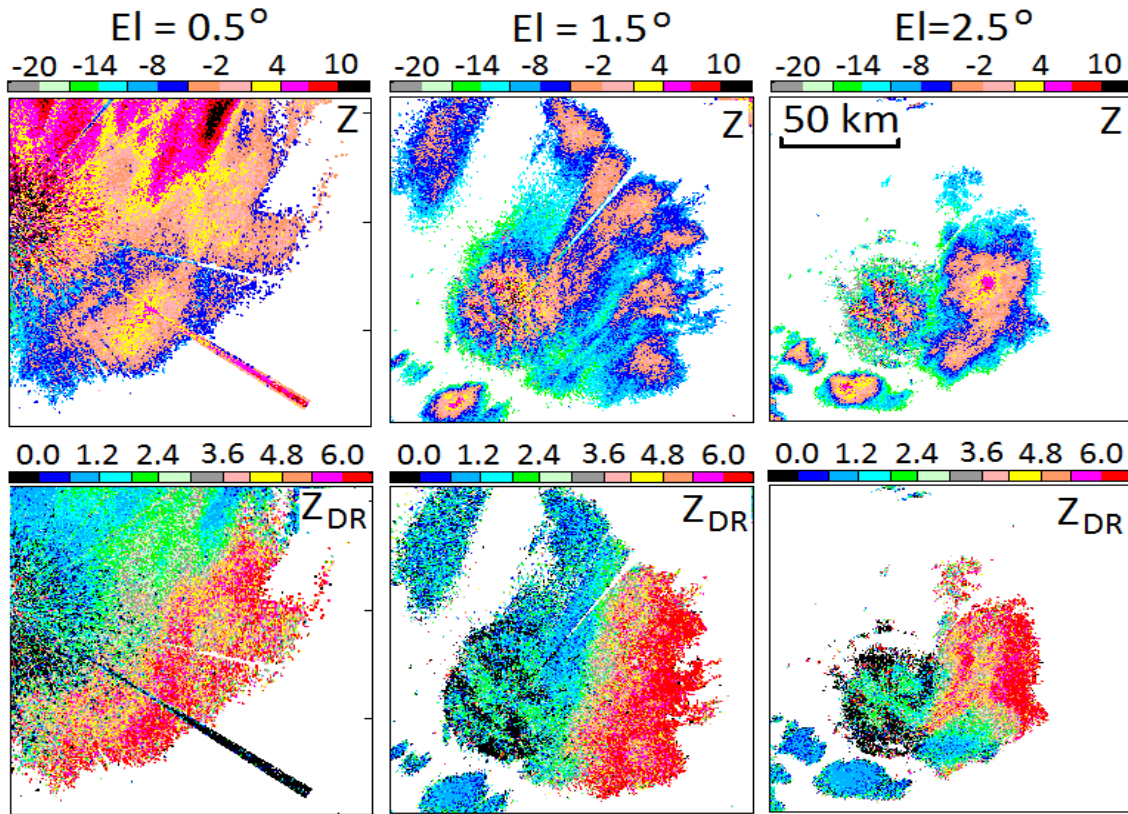
Fig. 7.3 (top row): Reflectivity fields at elevations of 0.5, 1.5, and 2.5° collected with KOUN on 1 February 2011 at about 1948 UTC. (bottom row): Corresponding Z_{DR} fields. The radial spike to the south-east in the left column is from an interference signal.

An example of observations of plate-like ice particles is shown in Fig. 7.3. The data were collected with WSR-88D KOUN on 02/01/2011. One can see large areas with $Z_{DR} > 4$ dB at elevations 0.5, 1.5 and 2.5°, i.e., yellow and red colored areas. A distinct category can be introduced to the Hydrometeor Classification Algorithm (HCA): plate-like ice particles, which are recognized by $Z_{DR} \geq 4$ dB. This information is useful for cloud modeling.

Z and Z_{DR} RHIs of an ice cloud are shown in Fig. 7.4. A layer of high Z_{DR} at the height of about 4.5 km is apparent, where the maximal Z_{DR} values reach 7.5 dB. One can see a sufficiently thick layer with $Z_{DR} > 4$ dB. So we conclude that this layer contains plate-like particles. There are three layers beneath the cloud; these layers exhibit low Z_{DR}, which are areas of Bragg scatter.

Polarimetric radar parameters can be used to retrieve particles' axis ratios (length/width) and the degree of their orientation in clouds. The equations derived in the Appendix have been applied to a case shown inFig. 7.3. A layer of $Z_{DR} > 4$ dB at heights around 4.5 km is seen in Fig. 7.3, (central panel). For such Z_{DR} values, cloud particles have the plate-like shape (Melnikov and Straka 2013). The threshold $Z_{DR} \geq 4$ dB have been obtained for antenna elevation angles less than 7°. Z_{DR} values decrease with antenna elevation. Fig. 7.4depicts elevation dependences of Z_{DR} for thin ice plates and needles oriented strictly horizontally. At low elevations, if Z_{DR} is larger than 4 dB, the scatterers have plate-like shapes. At an elevation of, for instance, 40°, ice

columns have a maximal Z_{DR} of 2 dB and if measured Z_{DR} values are larger than 2 dB, the scatterers have plate-like shapes. The dashed line in Fig. 7.4 has been used to identify areas with ice plates in Fig. 7.3 at all available elevation angles.
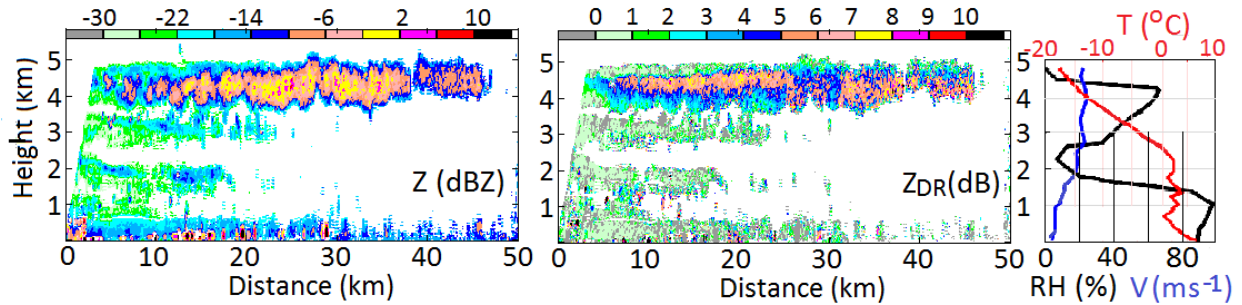
Fig. 7.3: RHI of reflectivity(left panel) and Z_{DR} (central panel) collected with KOUN on 23 March 2013 at 1855 UTC in an azimuth of 270°. The right panel presents the rawinsonde data obtained at 00 UTC 24 March 2013 at the KOUN site.
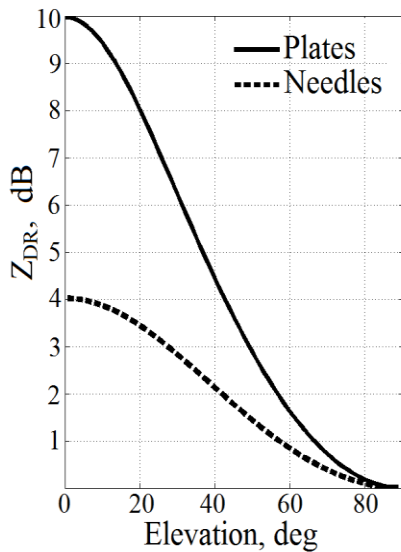
Fig. 7.4: Z_{DR} as a function of antenna elevation angle for very thin horizontally oriented ice plates (solid line) and needles (dashed line).

Let a and b be the major and minor axes, respectively, of a scatterer in a form of a spheroid. Orientations of cloud particles are described with a distribution of their canting angles θ. The standard deviation in angle θ is the degree of orientation σ_θ. To obtain the mean a/b of the particles and their degree of orientation from measured Z_{DR} and ρ_{hv}, a method proposed by Melnikov and Straka (2013) has been used with the generalizations described in the Appendix. The maximal elevation angle for the WSR-88Ds is 60°. For elevation angles in an interval 0-60°, a look-up table for Z_{DR} and ρ_{hv} with $0.01 \leq b/a \leq 1$ (stride = 0.01) and $1° \leq \sigma_\theta \leq 90°$ (stride = 1°) as the input parameters has been generated. The measured pairs of Z_{DR} and ρ_{hv} were then used as

the inputs to the table to obtain b/a and σ_θ for a case shown inFig. 7.3. The results are shown in Fig. 7.5 where panel (a) exhibits an area filled with plate-like particles and is shown with the red color. The rest of the radar echo is presented with gray color. It can be seen that almost the entire cloud located higher than 3.5 km contains plate-like ice particles.
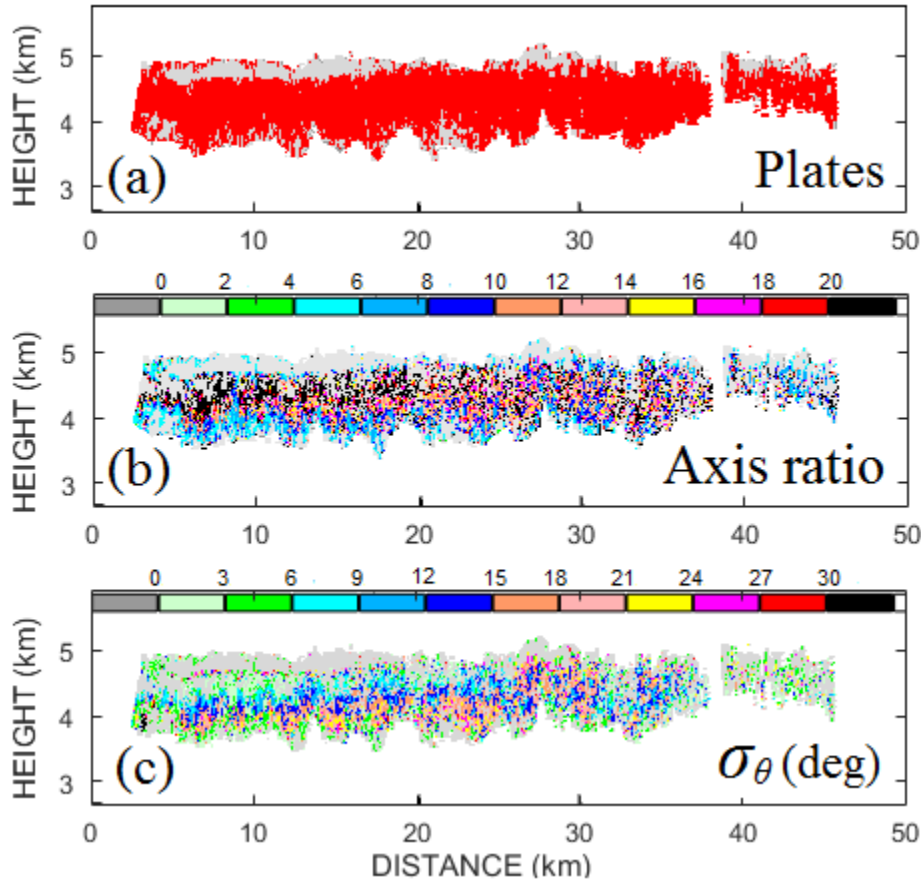
Fig. 7.5 (a): Cloud areas occupied by plate-like ice particles (red color). Z and Z_{DR} data are shown inFig. 7.3. (b): Axis ratios *a/b* of plate-like particles. The light gray color indicates the cloud areas. (c): Degree of particles' orientation. Again, the light gray color indicates the cloud areas.

Panel (b) presents a field of axis ratios of the ice cloud plate-like particles. It is hard to guarantee a sufficient accuracy in retrieving *a/b* if the ratio is larger than 20. So, all axis ratios larger than 20 are painted with the black color. It is apparent that the cloud contains very thin plate-like particles having large axis ratios. The axis ratios decrease towards the cloud bottom. Panel (c) presents a field of σ_θ values in degrees. One can see that σ_θ decreases with height, meaning that the particles with larger *a/b* exhibit lower σ_θ. This situation could be due to the

34

following reasons: 1) Larger *a/b* make the particles more stable, and thus the particles with lower *a/b* flutter in the air more intensely. 2) Turbulence inside the cloud decreases with height which decreases the orientation disturbances at higher altitudes.

The temperature stratification (the right panel inFig. 7.3) shows that the temperatures in cloud areas filled with plate-like particles are in an interval from -12°C to -17°C. Such temperatures are favorable for the growing of ice plates (Pruppacher and Klett 1997, chapter 10).

One more case is shown inFig. 7.6, which is presented in the same format as that ofFig. 7.3. The cloud of interest is located at an altitude higher than 5 km. The radar echo below 3 km is from insects. In the cloud, areas of large Z_{DR} are seen in a form of patches, and not in a layer as inFig. 7.3. Areas of plate-like particles are shown in panel (a) ofFig. 7.7. The locations of ice plates having *a/b* > 20 (panel b, black color) are rather complicated. The field of σ_{θ} (panel c) shows that particles with large *a/b* have smaller σ_{θ} which could mean the particles with larger *a/b* are more stable in the air. The temperature in cloud areas containing ice plates is in an interval of -15° to-19°C, which is favorable for growing ice plates.
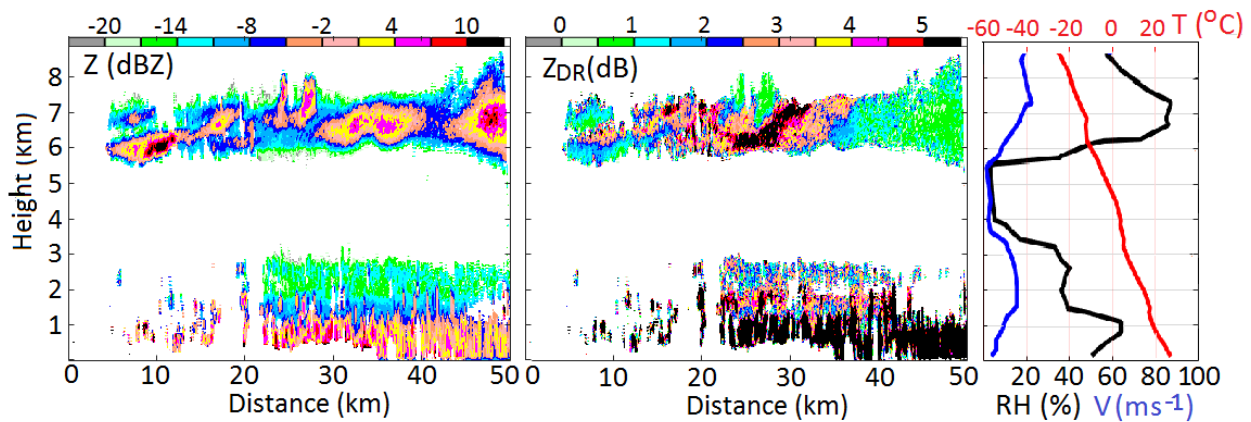

Fig. 7.6: RHI of reflectivity (left panel) and Z$_{DR}$ (central panel) collected with KOUN on 20 August 2016 at 0049 UTC at an azimuth of 270°.
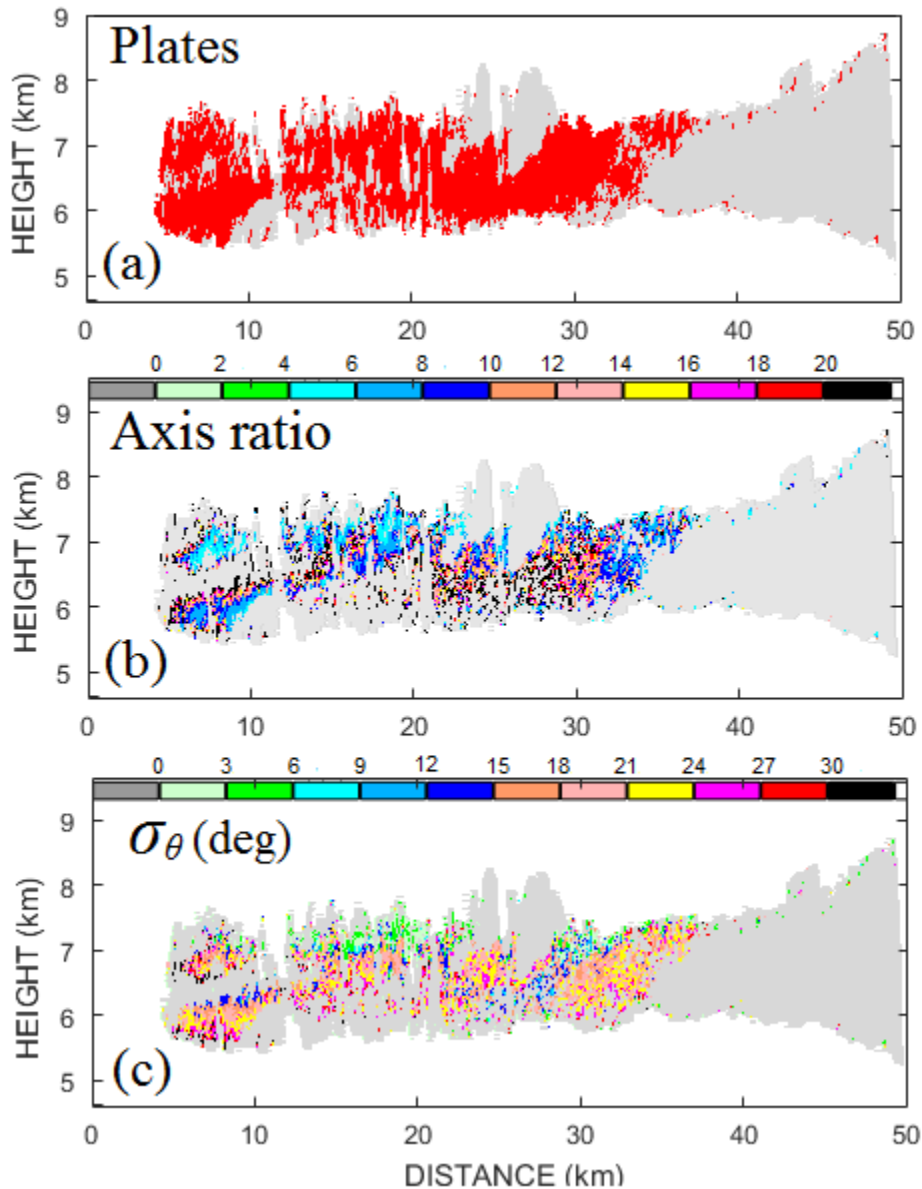
Fig. 7.7: Same as in Fig. 7.5 but on 20 August 2016 at 0049 UTC.

8. Comparisons of data from the WSR-88D and satellite CPR

The WSR-88D could provide complementary data on the vertical structure of clouds and precipitation to improve the information extracted from satellite observations. NASA's Cloudsat satellite has an onboard mm-wavelength radar to map the inner structure of clouds and precipitation (e.g., Stephens and Kummerow, 2007). This Cloud Profiling Radar (CPR) has the main parameters presented in Table 8.1.

Table 8.1: Parameters of the CPR, WSR-88D, and TDWR radars that map clouds

Parameter	NASA's CPR (Cloudsat)	NOAA's WSR-88D (short/long pulse mode)	FAA's TDWR (Terminal Doppler Weather Radar)
Wavelength (mm)	3	109	56
Pulse power (kW)	Not available	450	250
Pulse width (μs)	3.3	1.57/4.5	1.1
Antenna size (m)	1.85	8.54	
Beam-width (one-way half power width), deg	0.12	0.96	0.55
Radial resolution (m)	500	250/750	150
Two-way transversal resolution (m)	1400 (cross-track) 1700 (along-track)	49@10 km;	28@10 km
Z_{10} (dBZ)	Minimal detectable Z is < -29 dBZ	-21.5/-30 (single pol) -18.5/-27 (dual pol) -25.5/-34 (with enhanced processing in dual-pol).	-27 (estimated from the radar parameters)
Scanning capability	No	Yes	Yes
Doppler capability	No	Yes	Yes
Dual Polarization	No	Yes	No
Attenuation	Severe	Negligible	Negligible
Number of systems	1	157	47

To map clouds with the WSR-88D, the short radar pulse mode is preferable because it provides the shortest range resolution. One can see from Table 8.1 that the sensitivity of the WSR-88D in the short pulse mode with standard signal processing, i.e., -18.5 dBZ, is about 10 dB worse than that of the CPR. A sensitivity of -18.5 dBZ is related to the range of 10 km. This range corresponds to short horizontal distances from the radar and cloud detectability decreases as 20 log(Distance). For instance, at a distance of 50 km, detectability drops by about 14 dB and clouds with reflectivity values of about -4 dBZ can be detected with the WSR-88Ds. At a distance of 100 km, the minimal detectable reflectivity values are about 2 dBZ. These values are much higher than -29 dBZ for the CPR and this detectability does not depend on the distance to the clouds. For the first look, cloud detectability using the WSR-88Ds should be much lower than that for the CPR. But cloud observations presented in the previous sections of this report demonstrate sufficient sensitivity of WSR-88Ds for various types of clouds.

To obtain statistics of cloud detectability with the CPR and WSR-88D, radar echoes collected simultaneously with these radars have been analyzed. The best comparison would be that with a WSR-88D radar site lying right on the CPR's ground track. Such a site minimizes the

decrease in the WSR-88D's sensitivity with distance. For this experiment, two WSR-88D sites laying almost on the CPR ground track have been selected. The geographical locations of KGWX (Columbus AFB, MS) and KSHV (Shreveport, LA) are shown in Fig. 8.1. Fig. 8.2 presents the site locations with the ground CPR track overlaid (the red solid lines), where the arrows show the direction of movement of the Cloudsat. The median minimal distance between the tracks and WSR-88D locations is about 1 km with minimal and maximal distances of 0.1 and 18.2 km.
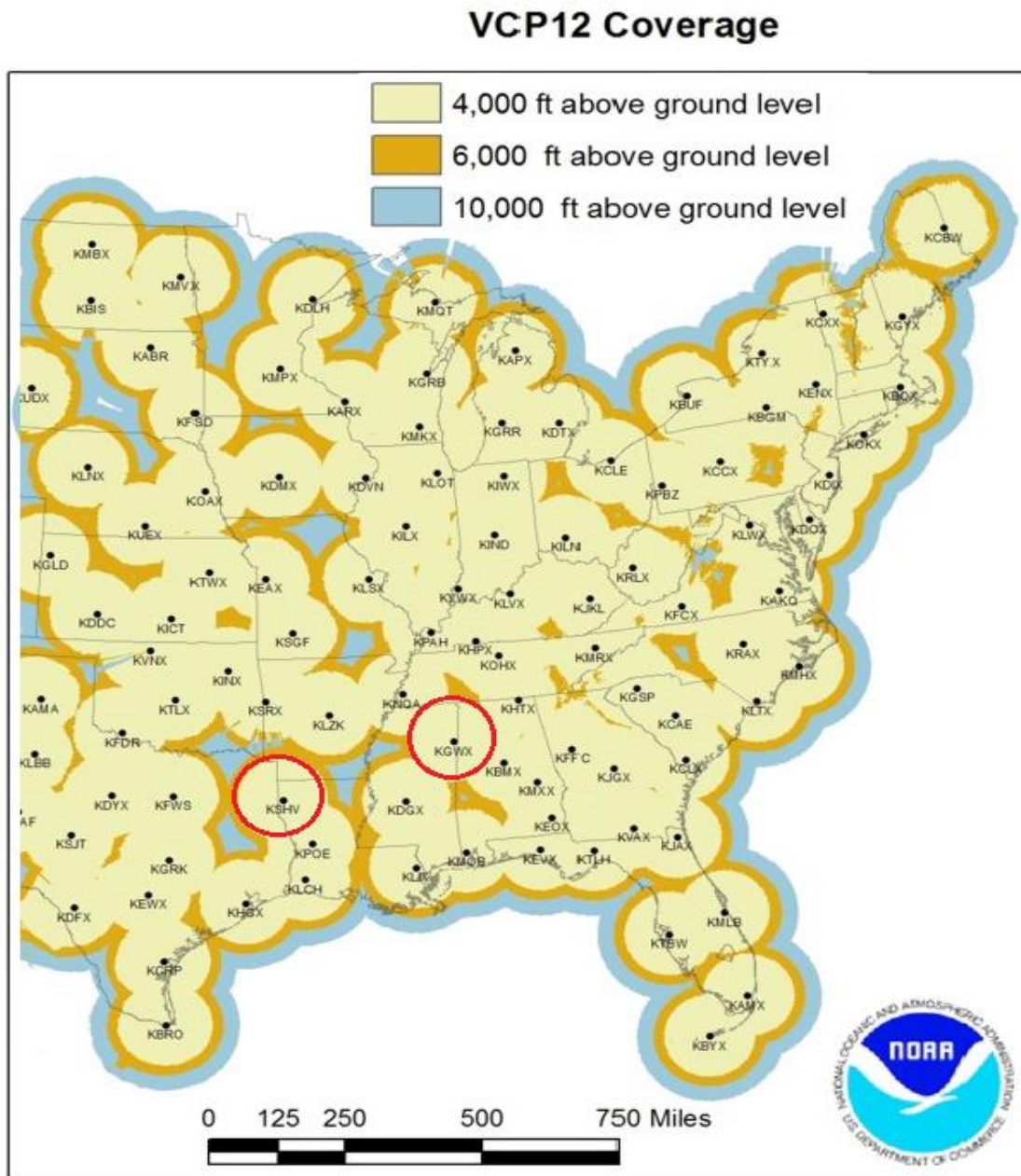
Fig. 8.1: Locations of the WSR-88Ds KSHV and KGWX
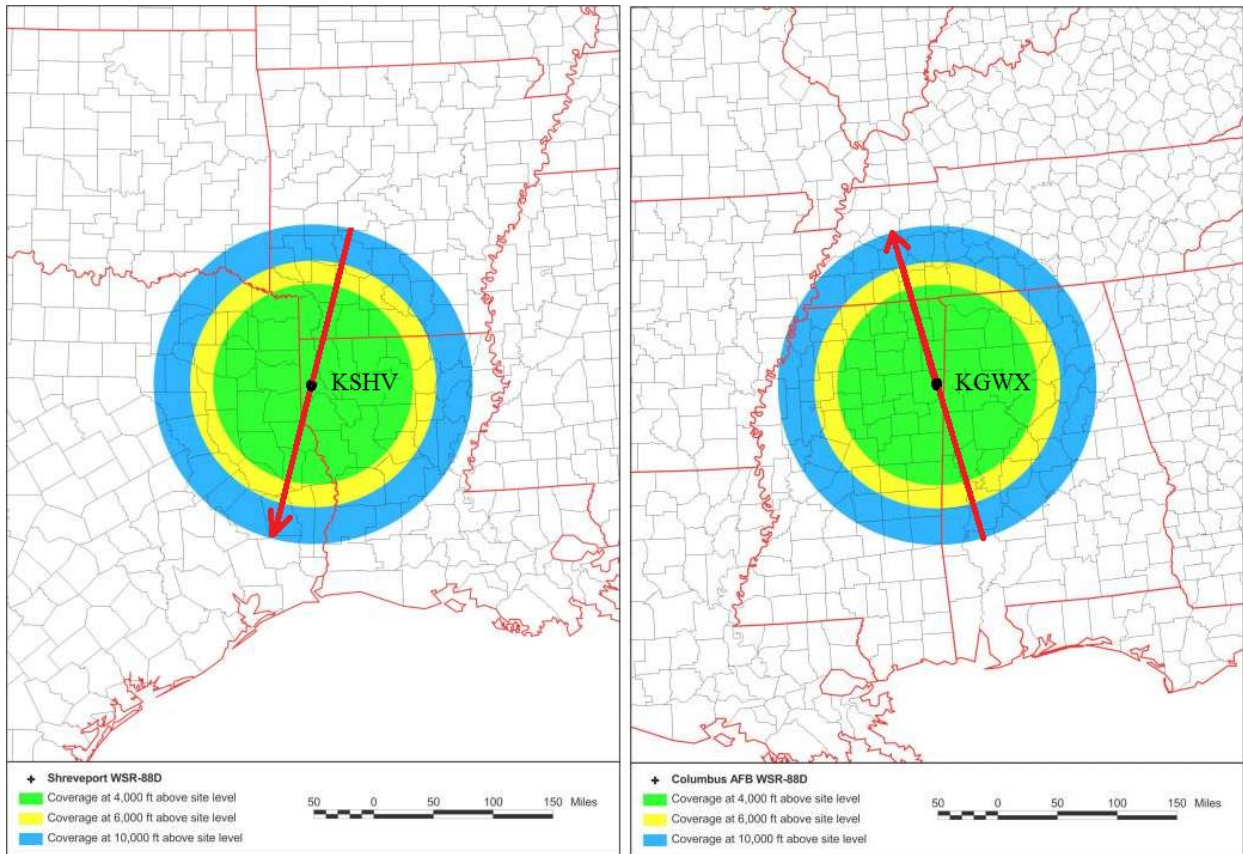
Fig. 8.2: CPR tracks (red thick lines) over sites KSHV (left, descending node) and KGWX (right, ascending node). The green circles indicate coverage at 4,000 ft. above site levels.

KGWX and KSHV are operational radars having a sensitivity of -18.5 dBZ at 10 km in the short pulse mode. In cloudy weather without precipitation, the radars can run the "clear air" VCPs with the maximum elevation of 4.5° (an example is shown in Fig. 8.3) which are not suitable for good comparisons because of low antenna elevations. One can see weak echoes in the left panel at heights of 5 − 7 km at distances of about 80 km. The CPR's reflectivity field (right panel) exhibits the maximal Z values of about 0 dBZ, which exceeds the detectability limit for the WSR-88D. Most likely, these clouds would be detected with KSHV more clearly if the radar would have run a precipitation VCP with the maximum elevation angle of 19.5°. In the case in Fig. 8.3, the cloud tops and bases obtained from the radars are at 5.0 and 7.0 km. That is, despite the fact that KSHV was running the clear air VCP, the cloud boundaries obtained from the CPR and WSR-88Ds are in good agreement.
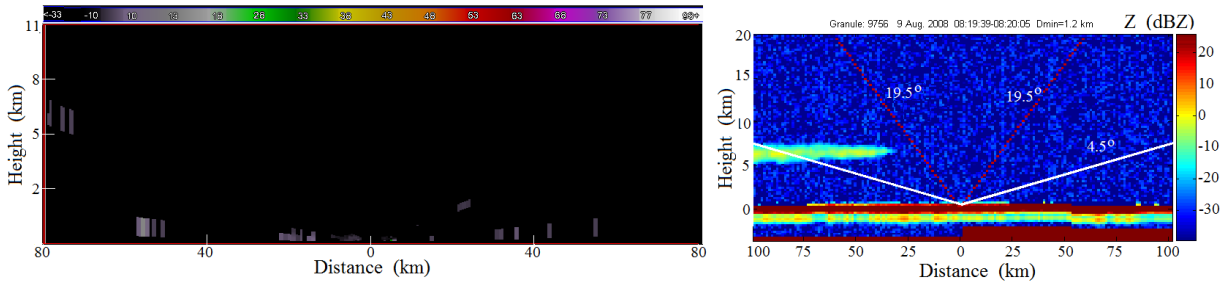
Fig. 8.3 (left): KSHV pseudo-vertical slice along the CPR's track. (right): CPR's reflectivity field in the vicinity of KSHV. The data were collected 9 August 2008 at about 0820 UTC.

There is another difficulty in the comparisons of radar echoes: pseudo-vertical cross-sections from the WSR-88Ds are obtained from a whole VCP that ran for several minutes, i.e., about 10 (6) minutes for clear air (precipitation) VCPs. The Cloudsat collects data from distances within 100 km from the WSR-88Ds for 26 sec, thus creating a snapshot of reflectivity. A time span of 6 - 10 min is sufficiently large for changes in cloud fields to occur, so the comparisons of reflectivity fields from the radars will have a statistical sense.

An example of no cloud detection with KSHV is shown in Fig. 8.4. KSHV was running the clear air mode that prevented detecting the clouds at higher elevations and shorter distances. Fig. 8.4 also demonstrates some differences in detections of atmospheric biota with the CPR and WSR-88Ds. The left panel exhibits such echoes at heights up to 2 km (a spot echo is seen at a height of 3.5 km). Reflections from biota are barely recognizable in the right panel: those heights are much lower than 2 km. This interesting feature could be due to the difference in wavelengths, but has no clear explanation as of now.
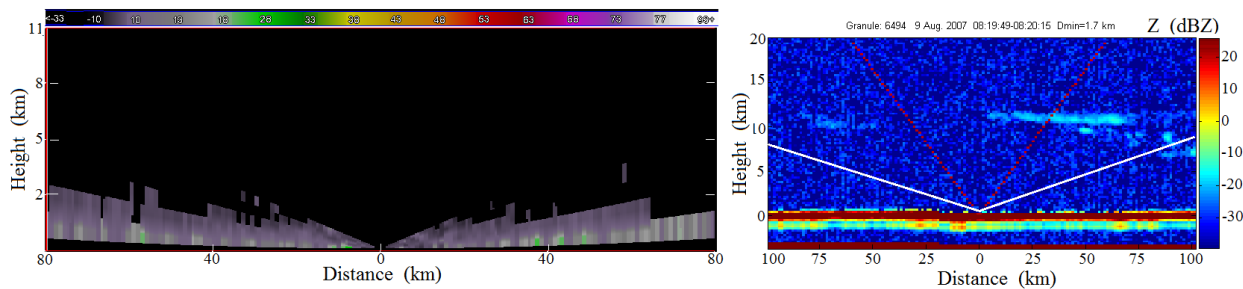
Fig. 8.4: Same as in Fig. 8.3, but for 9 August 2007 at around 0820 UTC.

An example of radar echoes from thick nonprecipitating clouds is shown in Fig. 8.5. KGWX radar was running a precipitation VCP with the maximal antenna elevation of 19.5°. The cone of silence is clearly seen in the left panel. It is also obvious that a "saw tooth" echo pattern exists because of large steps at higher antenna elevations. Nevertheless, KGWX detected the clouds and provided sufficiently accurate estimations of the cloud tops and bases at distances up to 100 km from the radar.
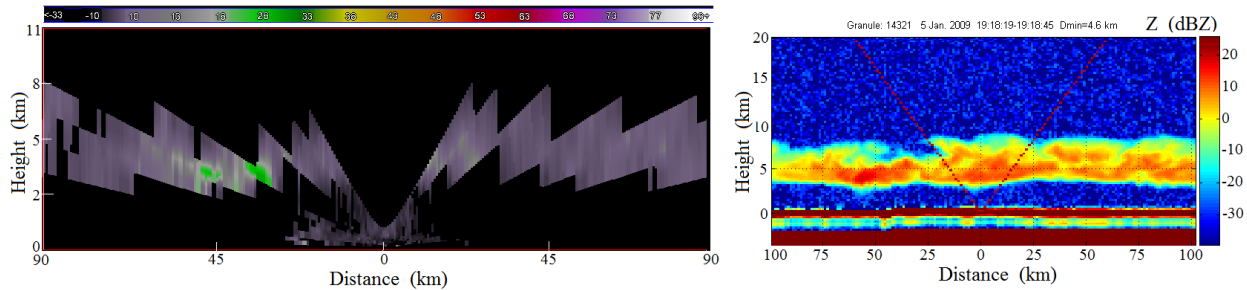
Fig. 8.5 (left): KGWX's pseudo-vertical reflectivity vertical cross-section on 5 Jan. 2009 at1940 UTC. (right): CPR reflectivity field (granule 14321) on the same day at 1910 UTC.

An example of a precipitation echo is shown in Fig. 8.6 where the cloud tops can be easily compared. One can also obtain the base of nonprecipitating clouds to the left from radar to distances of about 45 km and compare it with the one from the CPR (right panel).
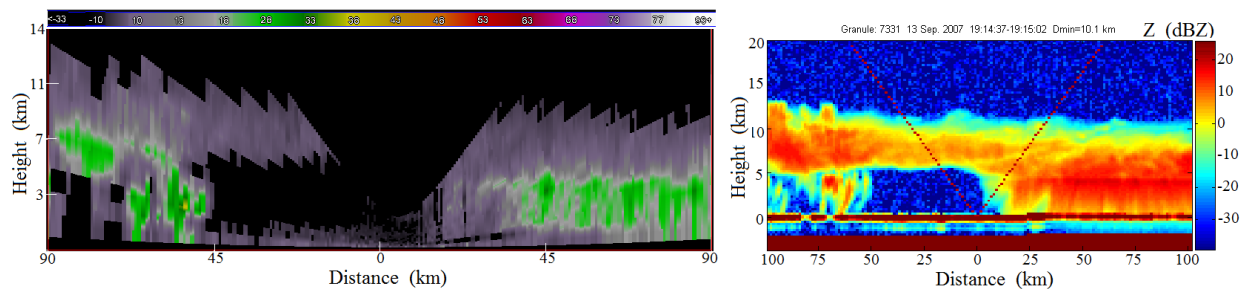
Fig. 8.6: Same as in Fig. 8.5, but for 13 September 2007 at 1914 UTC.

Due to the WSR-88Ds' sensitivities decreasing with range, the data on cloud tops and bottoms have been divided into two categories: within 50 km and beyond 50 km from the WSR-88D. The total number of cloudy cases with simultaneous observations is 56. In 15 cases, WSR-88Ds did not detect clouds. The missing cases are typically high, light clouds as in Fig. 8.4 when the WSR-88Ds ran a "clear air" VCP with the maximal antenna elevation angle of 4.5°. The statistics of the differences between heights measured with the CPR and WSR-88Ds for the rest of the 41 cases are presented in Fig. 8.7. Panel (a) presents the difference of cloud top heights obtained from the WSR-88Ds and CPR within distances of 50 km. One can see that the median difference is close to zero with some tail at the negative values meaning that WSR-88Ds sometimes underestimate the cloud tops due to lower sensitivity in comparison with the CPR. The differences between cloud lower bounds, obtained within distances of 50 km, have a median at 0 km (panel (b)). The cloud top differences at distances beyond 50 km have a median close to 0 km with visible bias to the right, meaning that the WSR-88Ds overestimated the top heights. This situation is most likely due to the effect of increasing beam-width with distance. The heights of the "teeth" of "saw tooth" patterns are at the center of the radar beams. If a cloud top is lower than the center of beam but produces enough signal to be detected, echoes are placed at the beam's center that will increase the apparent echo heights. In a case where two heights can be obtained from two echo sides, i.e., to the left and right from the radar site, two heights have been obtained. An example is in Fig. 8.6 where the cloud top heights at 90 km from the radar in either

41

direction are different. That is why the total number of cases which can be obtained from Fig. 8.7 is larger than the 41 cases suitable for the comparisons.
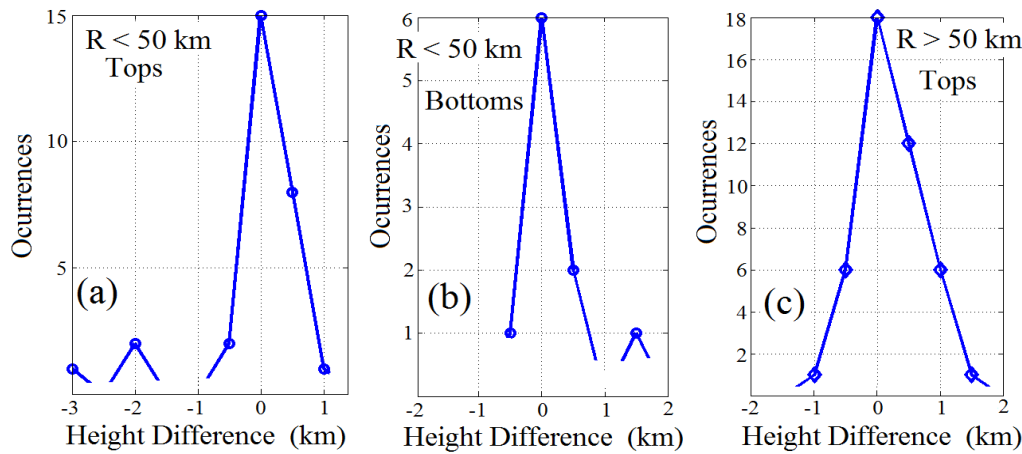
Fig. 8.7: Histograms of the differences between cloud boundaries obtained with the WSR-88Ds and CPR, i.e., height(WSR) – height(CPR). (a): The differences between the cloud tops observed within distances of 50 km. (b): Same as in (a) but for the cloud lower bounds. (c): Same as in (a) but for distances beyond 50 km.

Our analysis also reveals different detections of atmospheric biota by the CPR and WSR-88Ds; an example is in Fig. 8.4. One can see that the WSR-88D observes biota echoes up to a height of 2 km whereas the CPR's echo is seen very close to the ground. A possible explanation could be in the difference in the wavelengths. The atmospheric species are not Raleigh scatterers at mm-wavelengths (CPR), but at the S frequency band (WSR-88D), they are close to the Rayleigh regime. Furthermore, the Mie scattering regime for large scatterers has lower reflected power than that for the Rayleigh regime.

9. Comparisons of cloud data from the WSR-88D and TDWR radars

The Federal Aviation Administration (FAA) of the USA runs a network of terminal Doppler weather radars (TDWR) installed at the major airports. The TDWRs operate at the C frequency band and have parameters listed in Table 8.1. Due to a shorter wavelength and narrower beam-width, the TDWR's calculated sensitivity is about 5 dB better than that of the WSR-88D (attenuation of radiation in the waveguides is assumed to be 6 dB stronger than that for the WSR-88Ds). So, the TDWRs should observe nonprecipitating clouds more effectively than the WSR-88Ds.

An example of simultaneous observations of nonprecipitating clouds with the WSR-88D KOUN and TDWR TOKC, situated 3.85 km away from KOUN, is shown in Fig. 9.1. Reflectivity collected with TOKC and KOUN at the elevation of 60° is shown in panels (c), (d), and (e). Panels (c) and (d) present KOUN's data collected with the long and short pulses. The maximal cloud tops from the panels are 12.3 and 12.1 km whereas it is 12.0 km from panel (e). We see that KOUN's sensitivity in the short pulse mode is about the same as that of TOKC

despite the big difference in their wavelengths. In the long pulse mode (panel c), KOUN's sensitivity is better that that of TOKC.
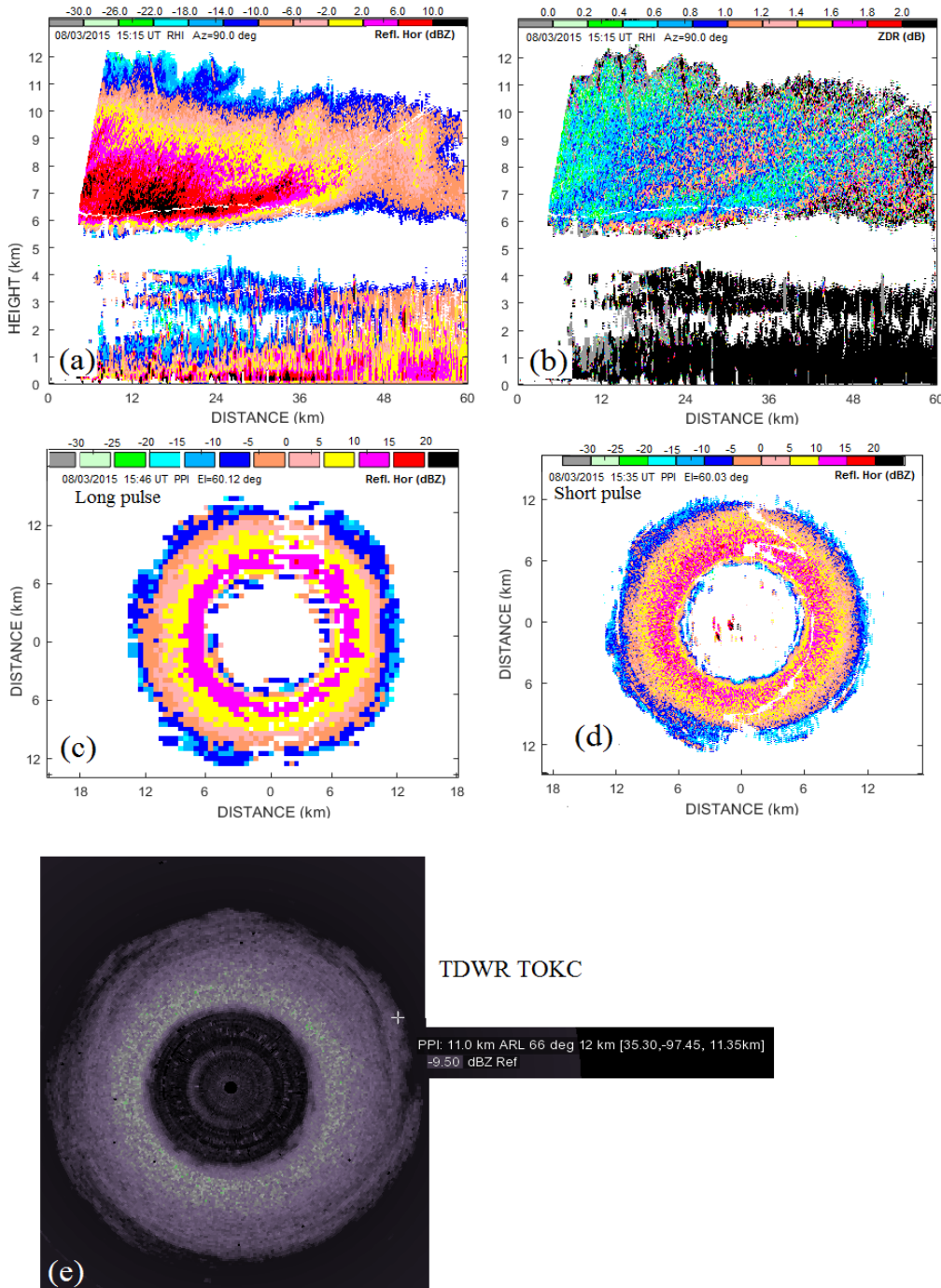
Fig. 9.1 (a, b): Vertical cross-sections of Z and Z_DR collected with KOUN at an azimuth of 90°. (c, d): PPIs of reflectivity at an elevation of 60° collected with the long and short pulses. (e): PPI of reflectivity collected with TOKC at 1540 UTC at an elevation of 60°.

Panels (a) and (b) show vertical cross-sections of Z and Z_{DR} in the short pulse mode with 5-time range oversampling. This mode allows a detailed presentation of radar variables. One can see that the maximal cloud top is at 12.1 km. The Z_{DR} field allows for distinguishing the cloud and insect echoes. The latter is located below 4.3 km and has Z_{DR} values exceeding 5 dB.

10. The WSR-88D as a wind profiler

The wind in the atmosphere is obtained with a special radar network of wind profilers operating at wavelength of about 70 cm. Return signals in the profilers are weak, so various processing algorithms are applied to measure the Doppler velocity. Cloud radar echoes observed with the WSR-88Ds exhibit a wide range of signal strength, i.e., from SNR values less than -5 dB up to SNR stronger than 30 dB. The echo intensity depends upon the ice/water content and the range to clouds. SNR diminishes as R^2 with range R. So to obtain the wind in clouds, various techniques can be applied to WSR-88D's signal; usual processing, i.e., the pulse pair technique can be used for strong echoes, and spectral processing similar to one in use in the wind profilers.

An example of the Doppler velocity field from a stratiform cloud is shown in Fig. 10.1. An annular ring echo is a form of nonprecipitating clouds. The reflectivity field is shown in Fig. 3.1. Aliased velocities are seen at the cloud edges at azimuths about 50° and 230°.
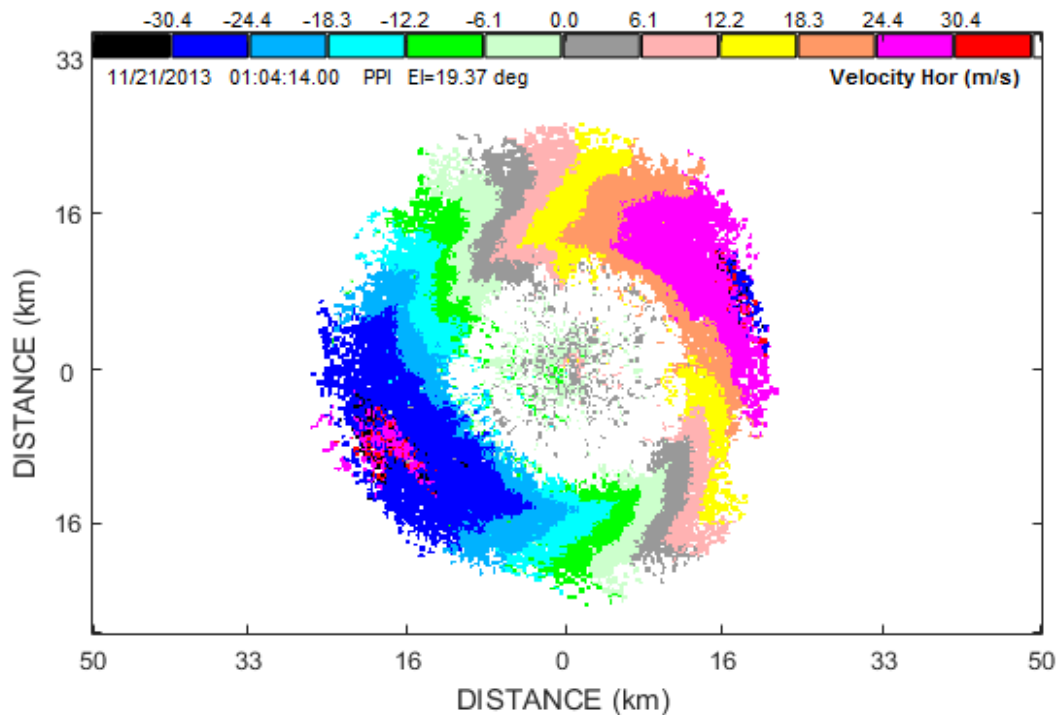
Fig. 10.1: Doppler velocity field collected with KTLX on 21 Nov. 2013 at 0140Z at the elevation of 19.4°.

Since the vertical velocities in clouds are much smaller than the horizontal ones, the latter can be obtained from the measured Doppler velocities by using Velocity-Azimuth-Display (VAD) technique. The procedure consists of two steps:

- velocity dealiasing that is done in the radial direction
- VAD technique is applied azimuthally.

The dealiasing procedure is straightforward. Since just a single line of zero isodop is exhibited, the velocities lie in the interval $\pm 2V_N$, i.e., two Nyquist intervals. In the case in Fig. 10.1, this interval is ± 61 m s^{-1}. The dealiasing procedure is applied radially. The dealiased velocities are then used azimuthally in the VAD technique by matching an azimuthal velocity profile with a sinusoid. The radial wind and its direction have been obtained from a matching sinusoid. The horizontal wind has been obtained by the multiplication of the velocity by 1/cos(El), where El is the elevation angle. The results are shown in Fig. 10.2. One can see that the horizontal velocities and their directions in clouds are obtained with good precision, which is important for cloud physicists and modelers. The height resolution of the data is 83 m (250 m radar radial resolution multiplied by sin(19.5°)), which is much smaller than the height resolution of the NOAA's wind profilers.
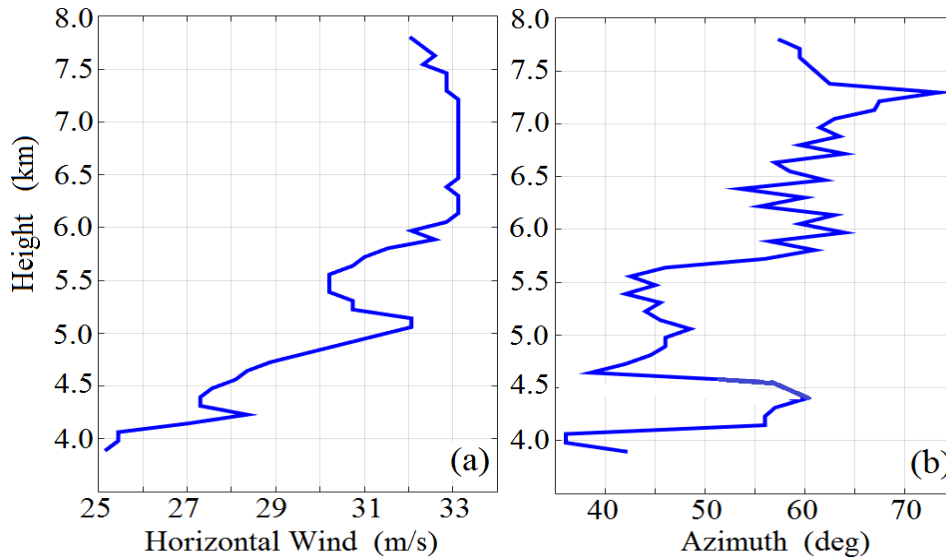
Fig. 10.2 (a): Height profile of the horizontal wind and (b): the wind direction for the case shown in Fig. 10.1.

The WSR-88D uses currently the 2-dB SNR threshold to get good quality data. It is possible to enhance detectability of the WSR-88D by lowering the SNR threshold below 0 dB, which allows observing much weaker radar returns. To suppress noise contaminations, a de-speckling procedure is applied. Fig. 10.3a shows a reflectivity field collected on a cloudy day. The SNR threshold was – 7dB, i.e., 9 dB below standard threshold of 2 dB. The clouds were so

weak that even at this threshold, they were not seen in the reflectivity field. Bragg scatter layers (with contamination from biota at heights between 2 and 3 km) are seen up to 6.5 km. The corresponding Doppler velocity field is shown in panel (c).
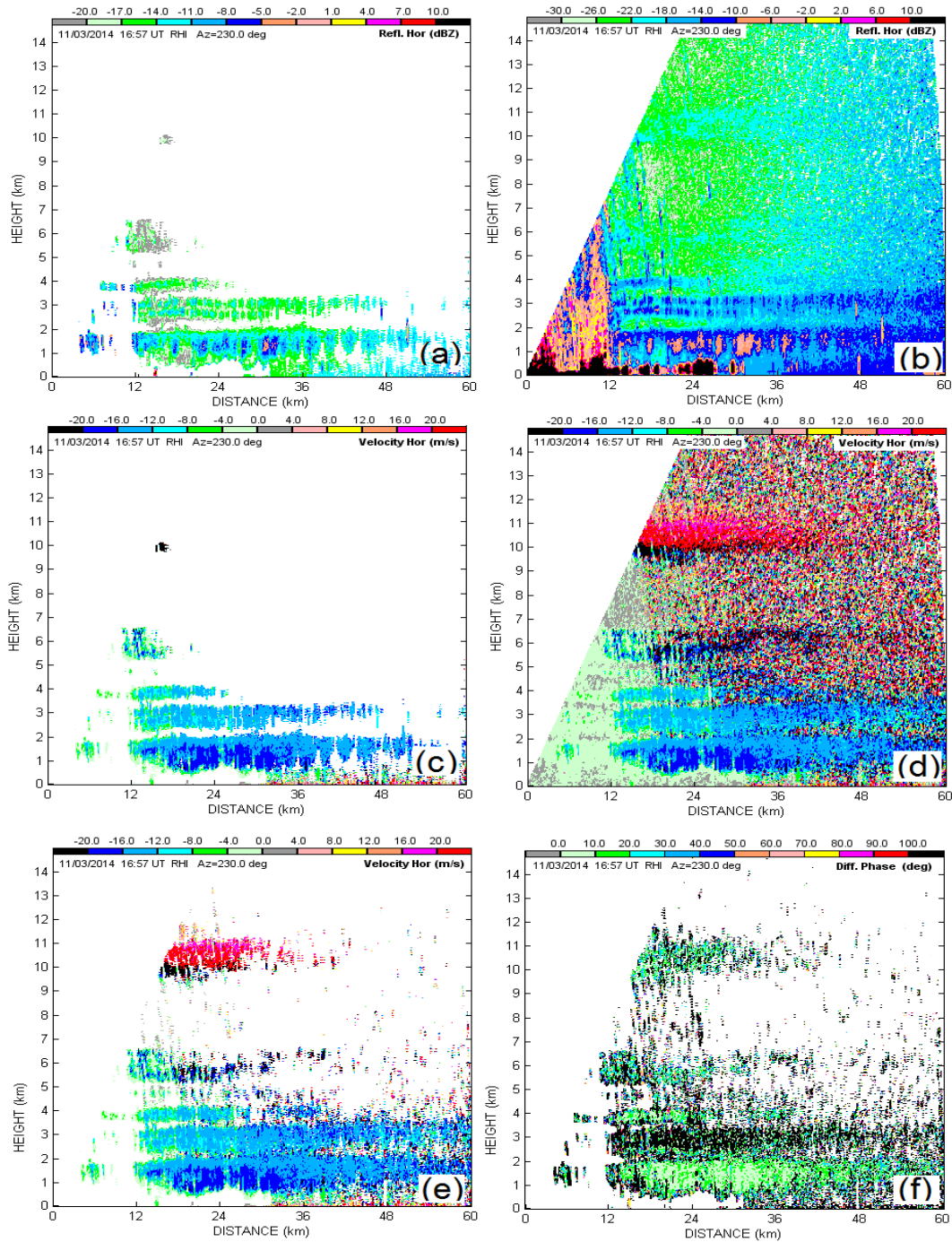
Fig. 10.3: RHI collected with KOUN on 3 November 2013 at 1657 UTC in the azimuth of 230°. The data in various panels are discussed in the text.

46

The initial non-thresholded Z field is shown in panel (b). The whole field is filled in with noise; strong leftovers of ground clutter are also seen at ranges within 12 km. These echoes emanated from antenna sidelobes. An apparent increase in values with range in noisy areas is due to R^2 normalization applied in the reflectivity calculations. However, a human eye can recognize a slight change in the pattern at heights from 10 to 11 km and distances close to the radar. The non-thresholded Doppler velocity field is shown in panel (d). Here it is easy to see the change in pattern at heights 10 - 11 km. Because the Doppler velocity is not biased by noise, we conclude that we observe true Doppler velocities in this layer.

Panel (e) has been generated using the SNR threshold of -10 dB. Lots of noise speckles remain in the image, but the presence of echoes at heights 9.5 - 12 km is apparent. Panel (f) shows the field of differential phase that can be used to recognize very weak echoes: one can see that the values (green colors) are the same for the Bragg scatter areas and clouds. Height profiles of the wind velocity and its direction are shown in Fig. 10.4. The profile of wind direction has been smoothed with the Golay filter. This case demonstrates that the WSR-88D can be used to measure the winds in clouds and areas of Bragg scatter at very low SNR values. Such a capability could be advantageous because the number of WSR-88D systems across the country is much larger than that of the wind profilers. The WSR-88D can measure the winds in weak clouds located at high altitudes, which are problematic for the wind profilers.
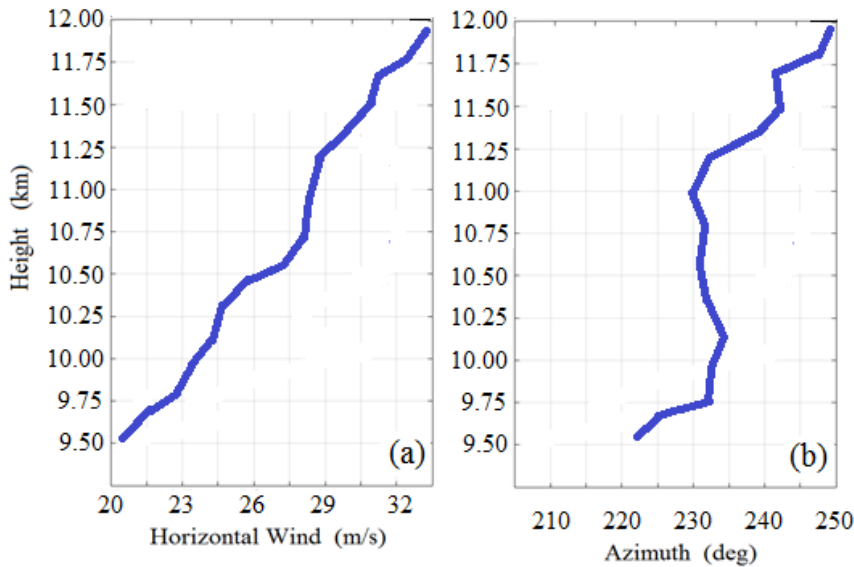

Fig. 10.4 (a): Height profile of the horizontal wind and (b): the wind direction for the case shown in Fig. 10.3.

11. Comparisons between cloud data from radar and the METAR system

It was shown in the previous sections of this report that the WSR-88D is capable obtaining the tops and bottoms of nonprecipitating clouds. Information about cloud bases is extensively useful for aviation. To obtain the cloud ceilings and types of clouds in the vicinity of a given airport , ceilometer measurements and visual observations are conducted. The METAR meteorological system that includes ASOS stations is the source of meteorological information for aviation. Two types of METAR information can be directly compared with radar data: the cloud bases and the types of clouds in an airport vicinity.

The WSR-88D KOUN is situated 20.8 km away from the KOKC station located at Will Rogers World Airport in Oklahoma City, OK. An azimuth of this station from KOUN is 325$^{\mathrm{o}}$, so radar vertical cross sections at this azimuth deliver information about clouds above the KOKC station. The METAR reports on cloud ceilings in hundreds of feet up to 12,000 feet. The ceiling represents the height of the lowest boundary of broken or overcast clouds. Visual cloud observations are reported in a textual form. An example of METAR data on cloud cover on 15 Sep. 2016 at 15:20:52 UTC is shown below:

METAR for: KOKC (Oklahoma City/Will R, OK, US)
KOKC 152052Z

Ceiling: 9000 feet AGL

Clouds: few clouds at 2200 feet AGL, scattered clouds at 7000 feet AGL, broken clouds at 9000 feet AGL, broken clouds at 16000 feet AGL

The numerical METAR information about cloud ceilings can be directly compared with cloud bases obtained from radar measurements. Radar is capable of delivering more precise information on clouds located above the cloud ceiling than the METARS because the ceilometer's lidar beam cannot penetrate deep into the clouds, and the visual observations are limited in accuracy. Comparisons of radar and METAR data are presented below for various types of clouds.

a. Low clouds in cold seasons

Atmospheric biota, i.e., flying insects, birds, and bats, produce sufficient returned radar signals and can mask low-level nonprecipitating clouds. This issue is severe in warm seasons in Oklahoma. In cold seasons, contamination from atmospheric biota is much less or absent and can be identified by radar more easily. To distinguish echoes from biota and clouds, Z_{DR} values can be used: Z_{DR} values from insects typically lie in an interval of 3-12 dB whereas Z_{DR} from clouds are typically lower than 3 dB. It was noted from radar observations that Z_{DR} from insects can be lower than 3 dB which can compromise the detection of clouds. On the other hand, clouds can have Z_{DR} values larger than 3 dB (ice crystals), which also makes it difficult to separate them

48

from biota echoes. In some situations, clouds and biota can be distinguished by using values of correlation coefficient ρ_{hv}, but this method also has limitations. Therefore, automated identification of radar echoes from clouds and biota can be difficult, so the METAR and radar data are compared herein by analyzing radar echoes visually.

An example of a radar vertical cross section on 6 March 2016 is shown inFig. 11.1. The METAR signals the ceiling height at 1200 feet (366 m). The base of the clouds from KOUN can be estimated at about 500 m above the KOKC station (Fig. 11.1, panel a). That is, the radar cannot accurately detect the lowest cloud boundary containing small droplets.

The METAR indicates an overcast cloud deck at 1200 feet, while the radar reveals a multi-layered cloud field. An analysis of other similar cases shows that the radar cannot obtain the bases of low clouds as accurately as a ceilometer; radar typically indicates cloud bases approximately 200-300 m higher.

The radar reveals the second layer echo at a height range of 1800 - 2200 m. Most likely, this feature is a cloud layer, but it could be a layer of Bragg scatter, i.e., an echo from turbulent clear air. It is not possible to distinguish clouds from Bragg scatter areas using radar data alone since Z_{DR} and ρ_{hv} from Bragg scatter are almost identical to those from clouds. So, this situation creates a difficulty in the identification of low level non-precipitating clouds: their echoes have the same radar characteristics as areas of Bragg scatter.
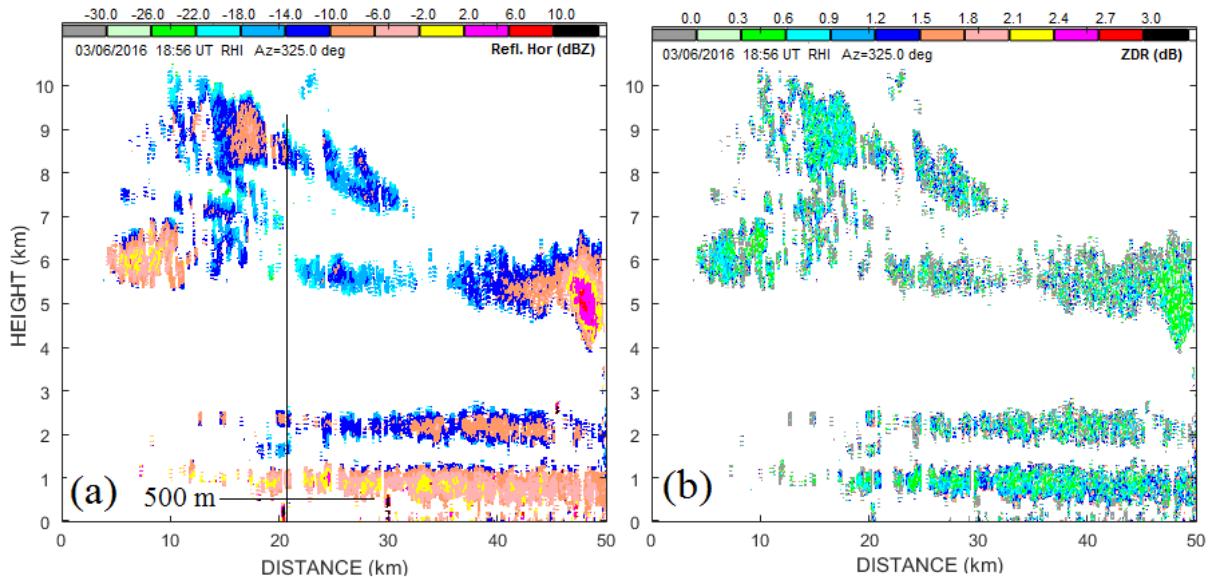
Fig. 11.1 (a): Vertical cross section of reflectivity and (b) Z_{DR} on 6 March 2016 at 1856 UTC collected at KOUN. The vertical black line in panel (a) shows the location of the KOKC station. The black horizontal line in panel (a) depicts a height of 500 m AGL.

The radar reveals scattered clouds at heights above 4 km stretching to heights higher than 10 km. This information is not available from the METAR system, so the radar is capable of revealing cloud patterns not seen through overcast low clouds, thus giving it an advantage over using METARs alone.

b. *Clouds above 12000 feet AGL.*

If clouds are above 12000 feet (3657 m), the METAR system reports a ceiling height of 12000 feet at least. An example of such radar data is inFig. 11.2. On 3 March 2016 at 1535 UTC, the METAR reported:

Ceiling: at least 12,000 feet AGL
Clouds: scattered clouds at 20000 feet AGL, scattered clouds at 25000 feet AGL

Comparing these reports with radar data (Fig. 11.2a), one can see that the radar detected layered clouds above the KOKC station. The cloud bases were at 5100 – 5300 m (16732 – 17388 feet), i.e., higher than 12000 feet. It is also noticeable that the tops of the clouds can be obtained (at around 6100 m = 20013 feet in this case) from radar data. At an azimuth of 180°, the radar indicates two cloud layers at median heights of 4.5 and 5.5 km (14763 and 18044 feet). The cloud tops in panel (b) are at 6.5 km (21325 feet). So here, the radar data is in agreement with the METAR text reports on cloud cover. However, the radar gives more detailed information on the cloud tops and layer structure than the METAR.
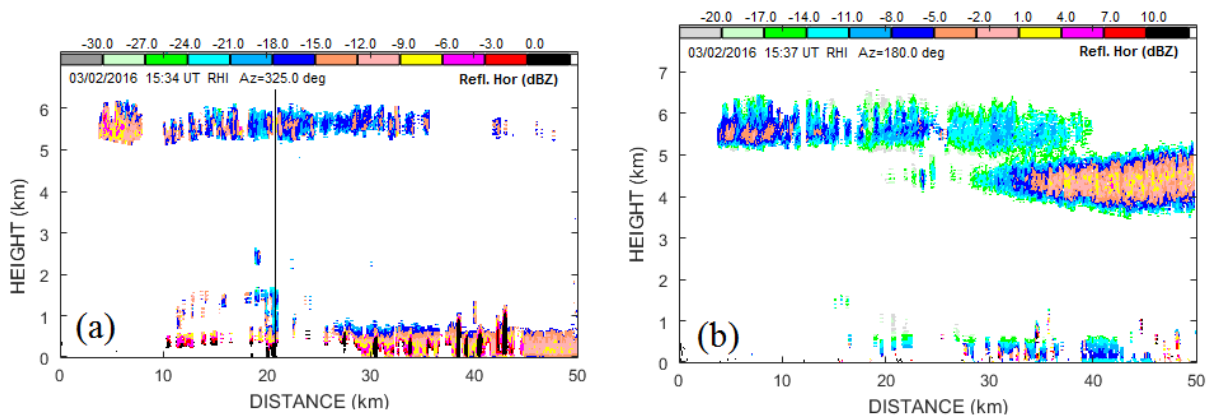
Fig. 11.2 (a): RHI at an azimuth of 325° (03/02/2016, 1534 UTC). (b) RHI in an azimuth of 180° (03/02/2016, 1537 UTC). The thin vertical line represents the location of the KOKC station.

Panel (a) in Fig. 11.2 also demonstrates a difficulty in the interpretation of radar data. The thin black vertical line shows the location of the KOKC station. Two-layered echoes at heights of about 400 m and 1500 m are evident directly above the KOKC station. The lower reflection is from insects and can be determined from Z_{DR} data (not shown). The second layer has low Z_{DR} and is from Bragg scatter, but could be interpreted as a cloud layer.

c. Clouds with variable ceiling heights.

Some problems in the comparisons of METARs and radar data are demonstrated in Fig. 11.3 in a case with broken clouds. This plot is an RHI from KOUN collected at 0200 UTC at an azimuth of 325°. The location of the station is shown in panel (a) with the thin black vertical line. The METAR reports the ceiling at 15000 feet (4572 m); the radar detects the lower cloud base at approximately the same height. In panel (a), there is a group of small clouds with their bases indicated at that height, but the radar does not detect the clouds *around* the group. The cloud base at that height is clearly detected at ranges beyond 30 km from the radar. It is hard to compare cloud bases from the METAR and radar when clouds have variable heights of low-level cloud boundaries.
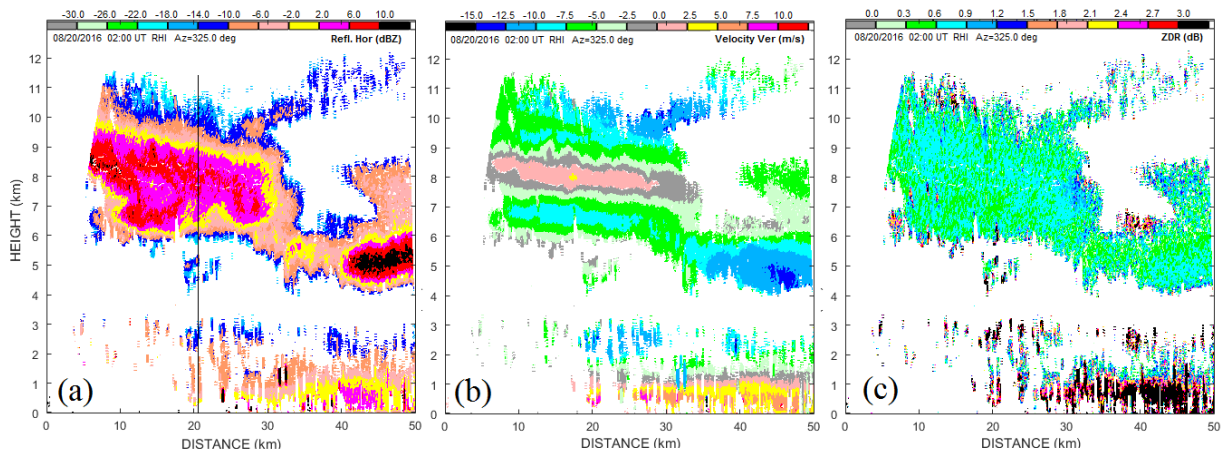
Fig. 11.3: Vertical cross sections of reflectivity (a), Doppler velocity (b), and Z_{DR} (c) from KOUN obtained at an azimuth of 325° at 0200 UTC August 20, 2016. The black vertical line in panel (a) represents the location of the KOKC station.

The METAR indicated scattered clouds at 4500 feet AGL, broken clouds at 15000 feet, broken clouds at 21000 feet, and an overcast cloud deck at 25000 feet. One can see from Fig. 11.3 that the radar is not capable of unambiguously detecting clouds at 4500 feet (1371 m). There is some reflection from that height at ranges beyond 30 km: see the Z_{DR} image in panel (b). However, this reflection could be interpreted as an echo from Bragg scatter. Broken clouds at 15000 feet (4572 m) from the METAR correlate well with the low cloud boundaries shown from the radar.

51

"Broken clouds at 21000 feet" (6400 m) from the METAR correlate well with radar data at that height. Although, the "Overcast cloud deck at 25000 feet" (7620 m) from the METAR is difficult to associate with radar data.

The METAR data do not contain information on the cloud tops. The radar clearly shows that the ceiling height is highly variable, and is higher than 11 km. The radar can also provide Doppler velocity in the clouds (Fig. 11.3b), which the METAR is not capable of measuring.

d. Clouds with light precipitation

Light precipitation is easily detectable with the WSR-88D at distances within 50 km from radar. Since the radar is highly sensitive, it is capable of detecting light precipitation, radar echos from which can mask echos from clouds. An example is shown inFig. 11.4, where precipitation is falling onto the KOKC station. The METAR shows the ceiling height at 900 ft (274 m). It is hard to connect this height with any features of the radar echo because light rain has sufficient reflectivity values to mask radar echoes from clouds. The METAR reports clouds: "overcast cloud deck at 900 feet AGL". Again, it is difficult to obtain cloud features in radar echoes because light rain masks the low cloud boundaries.
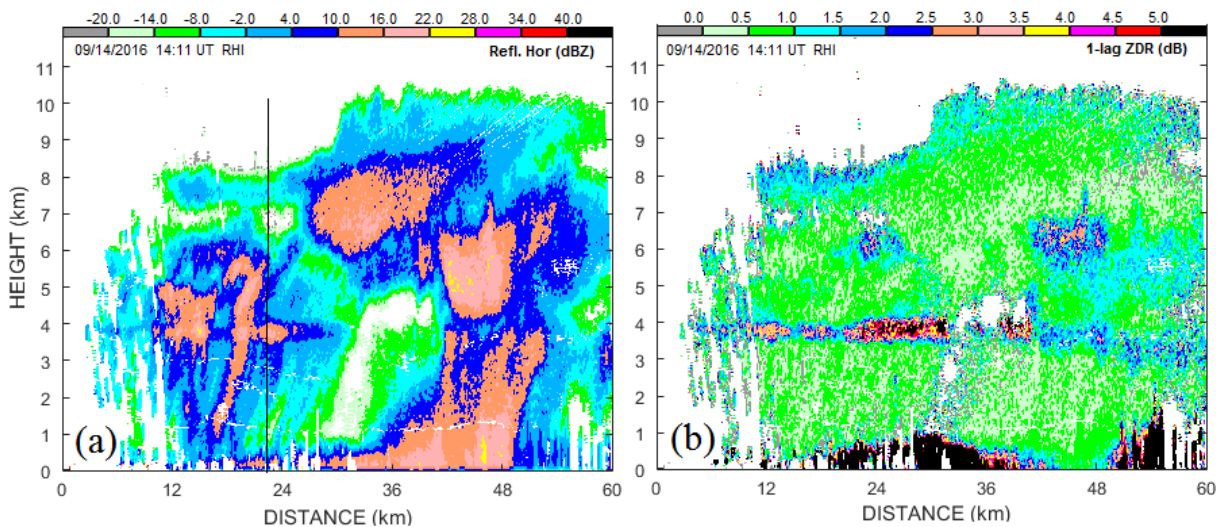
Fig. 11.4: Vertical cross sections of reflectivity (a) and Z_{DR} (b) from KOUN obtained at 1411 UTC on September 14, 2016. The black vertical line in panel (a) represents the location of the KOKC station.

e. Low-level warm clouds

The WSR-88Ds cannot observe warm clouds having small raindrops. Reflectivity is inversely proportional the 6-th power of diameter of a droplet. Low-level warm clouds frequently have droplets with diameters about 0.1 mm. Such raindrops are frequently undetectable at the S

frequency band; an example is shown inFig. 11.5 in which KOKC reported the ceiling height at 1500 feet (457 m) AGL. The radar shows a layered echo at 500 m, but Z_{DR} in the layer is 1-3 dB, which points to the presence of insects. There are weak radar echoes at heights of 1.5-2.5 km, which are most likely due to insects as well because of sufficiently large Z_{DR} values. So, low-level warm clouds were undetectable with KOUN on this day. The collected radar data suggest that this situation occurs frequently.
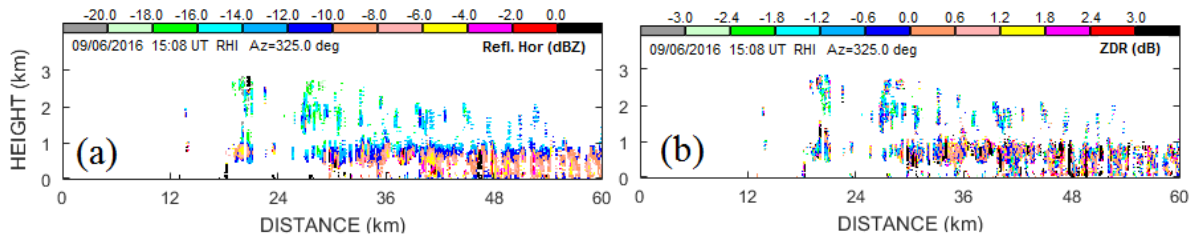
Fig. 11.5: Vertical cross sections of (a) reflectivity and (b) Z_{DR} collected with KOUN at an azimuth of 325° (09/06/2016 at 1508 UTC).

f. Concluding remarks

The comparisons of the METARs and radar data show that despite the high sensitivity of the WSR-88Ds, radars are not capable of detecting low boundaries of warm clouds with the accuracy of a ceilometer. KOUN indicates the cloud bases at heights 200-300 m higher than those from the KOKC's ceilometer, i.e., KOUN is not capable of detecting low-level warm clouds that have small droplets at a sufficiently low number concentration.

The second issue with radar data is that the radar cannot distinguish between warm clouds and Bragg scatter. – All radar parameters from these types of echoes are nearly identical. So, layers of Bragg scatter from radar can be mistakenly identified as clouds. Furthermore, in some situations, radar echoes from insects make it difficult to identify the bases of nonprecipitating clouds.

Radar data also can be useful for the aviation service in obtaining the cloud structure aloft and measuring the cloud tops. Radar can additionally deliver the wind parameters in clouds: strong gradients of Doppler velocity and large values of spectrum width could be used to indicate areas of strong turbulence and Kelvin-Helmholtz waves, which can be very hazardous to airplanes.

12. Monitoring system Z_{DR} calibration using clouds

Ice cloud particles fall down with their major dimensions oriented horizontally in the mean, though the particles experience fluttering (Pruppachet and Klett 1997, chapter 10). Nonprecipitating clouds have no strong electric fields inside that can orient ice cloud particles vertically. So Z_{DR} values in nonprecipitating clouds are positive. The mean axis ratio of ice cloud particles is close to 0.6 (Hogan et al. 2003) and the mean Z_{DR} value is about 1 dB for elevations

below 20°. At higher elevations, Z_{DR} decreases; see for instance the right panel in Fig. 7.. Positive Z_{DR} in clouds can be used to monitor negative system Z_{DR}: if the measured Z_{DR} in clouds is negative, the radar has a negative system Z_{DR} bias. Cloud Z_{DR} cannot be used to calibrate the radar because Z_{DR} values can be larger than 0.2 dB at antenna elevations below 60°, but the monitoring of negative system Z_{DR} is possible.

Some WSR-88Ds exhibit negative Z_{DR} biases that have been revealed by observing precipitation or Bragg scatter. Bragg scatter is often masked by biota in summer time. So measurements of Z_{DR} in nonprecipitating clouds can be used to monitor system Z_{DR} in "clear air" situations. A possible procedure to check if the system Z_{DR} bias is negative can contain the following steps:

- Measure Z_{DR} in small areas (sectors in range and azimuth).
- Obtain the minimum measured Z_{DR} in clouds.
- If the minimum Z_{DR} is negative, the system Z_{DR} is biased low by at least this minimal value.

A key element of the method is obtaining the median Z_{DR} value for a specified area. Minimal measured Z_{DR} in single range gates cannot be used because of fluctuations in the Z_{DR} estimates. The mean Z_{DR} should be calculated for an area. This area has been determined as follows. The standard deviation (SD) of the Z_{DR} estimate depends on the values of correlation coefficient ρ_{hv}, normalized spectrum width σ_{vn}, and number of samples M as (Melnikov and Zrnic 2004),

$$SD(Z_{DR}) = \frac{6.15}{M^{1/2}} \left[\frac{(1-\rho_{hv}^2)}{\pi^{1/2}\sigma_{vn}} \right]^{1/2} \text{[dB]}.$$

For typical cloud variables and radar parameters, SD(Z_{DR}) is about 1 dB. To reduce the standard deviation to the level of 0.1 dB, 100 range gates should be used [1 dB/sqrt(100) = 0.1 dB]. Two forms of such an area have been tested. The first form contains 5 radials and 20 range gates (a distance of 5 km along the radial) in each radial, i.e., 100 range gates total. This area is called Radially Aligned Area (RAA). The second form contains 10 radials with 10 range gates (a distance of 2.5 km) in each radial, i.e., 100 range gates total. This area will be referred to as Azimuthally Aligned Area (AAA). The median Z_{DR} values are calculated for areas in forms of RAA and AAA.
The algorithm consists of the following steps.

1) Create an RAA area in clouds.
2) Obtain SNR in the area: At least 100 range gates must have SNR >= 10 dB in both polarization channels.
3) At least 100 range gates must have correlation coefficients (CC) larger than 0.95.
4) Calculate median Z_{DR} for the area.
5) Loop steps 1-4 for the entire cloud echo and obtain the minimal Z_{DR}_min(RAA).
6) Perform steps 2-5 for an AAA area and obtain Z_{DR}_min(AAA).
7) Calculate Z_{DR}_bias = min[Z_{DR}_min(RAA), Z_{DR}_min(AAA)].
8) If Z_{DR}_bias < 0, then this value is the minimal negative system Z_{DR} bias.

The method is illustrated in **Error! Reference source not found.**. The data have been collected with WSR-88D KOUN on 21 December, 2013 at 0104 UTC. Results of the application of the method to the case in **Error! Reference source not found.**a, are shown in panels (b) and (c). Panel (b) is for the RAA areas: $Z_{DR}\_min(AAA) = -0.44$ dB (see the black arrow pointing on the area). Panel (c) shows an AAA area with minimal Z_{DR}: $Z_{DR}\_min(RAA) = -0.50$ dB (the black arrow points on the area). Thus, the system Z_{DR} is biased low by at least -0.50 dB. It is known from the rain and Bragg methods that KTLX's system Z_{DR} was negatively biased by about 0.5 dB that time. Thus, nonprecipitating clouds can be used to monitor system Z_{DR} bias.
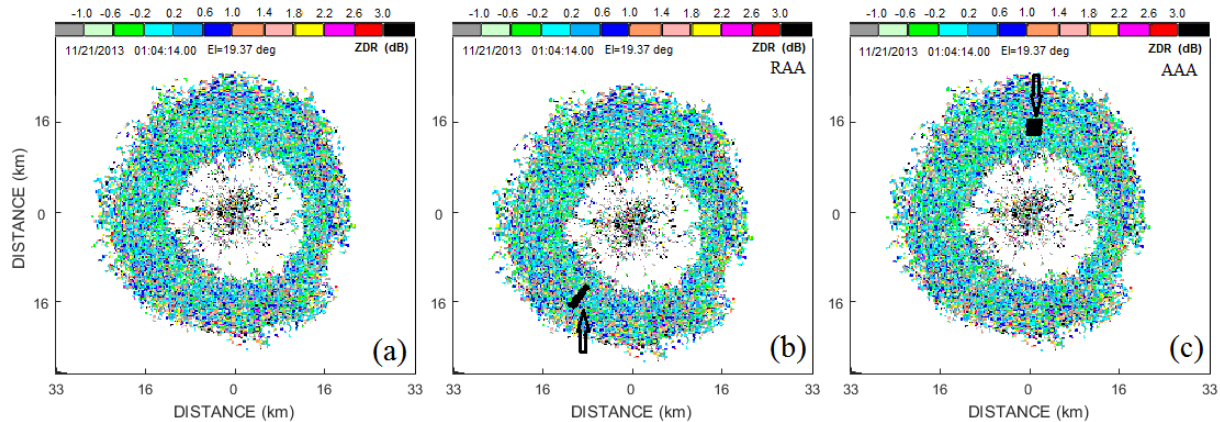
Figure 12.1 (a): ZDR fields from WSR-88D KOUN on Dec.21, 2013 at 0104 UTC at the elevation of 19.4o. (b, c): ZDR fields with RAA and AAA areas (black sector indicated with black arrows) with minimal ZDR values.

13. Cloud detection algorithm for the WSR-88Ds

It was shown in the previous sections that the sensitivity of the WSR-88D is sufficient for observations of various nonprecipitating clouds. There are challenging problems in the automated detection of nonprecipitating clouds with the WSR-88D:

- clouds have low reflectivity and should be distinguished from atmospheric biota,
- clouds should be distinguished from Bragg scatter layers,
- the use of long and short pulse widths can depend on cloud types,

In this report, we do not consider a special VCP for cloud observations that can give detailed information about cloud boundaries and microphysics needed for cloud modeling: detection of clouds using existing VCPs is the focus at this section. Two major cloud characteristics should be obtained automatically: the lower and upper cloud boundaries.

a. Detection of the cloud tops

Cloud tops can be obtained with the existing WSR-88D's algorithm by reducing the SNR threshold to +2 dB. The Multi Radar-Multi Sensor (MRMS) system displays the cloud tops at certain level of reflectivity, e.g., 16 dBZ. To obtain the true cloud top, this algorithm should be modified to switch from a Z threshold to a SNR threshold. The algorithm should be based on obtaining the cloud top at a given radial at the furthest range gate where a radar return is detected.

b. Detection of the lower cloud boundaries

The cloud lower boundary can be detected at the height of a range gate with detectable signal (SNR $\geq$ 2 dB) if there is no detectable signal in two (2) consecutive preceding range gates, or if detectable signals in these gates are not from weather. For instance, they can contain echoes from insects/birds or leftovers from ground clutter. The algorithm consists of the following steps:

- On a given radial, obtain four consecutive range gates with weather-like returns. To identify weather-like range gates, use the WSR-88D's algorithm for weather identification.
- Select the closest to radar range gate from the obtained four (4) weather-like range gates.
- Test two (2) range gates preceding the selected one. If there are no significant returns or the returns are not from weather, the height of the selected range gate is the height of cloud bottom for the given radial.
- Obtain the cloud top by applying algorithm a) above and apply algorithm b) for the part of radial beyond the obtained top to verify there is no second cloud layer above the first one.

The above algorithms for detecting the cloud boundaries have a caveat: layers of Bragg scatter can be classified as cloud layers; examples are in Fig. 7.1 and Fig. 10.3. In the left column of Fig. 7.1, one can see two layers at heights of 3.5 - 4 km and 4.5 - 5 km with weather-like polarimetric parameters, i.e., low Z_{DR} and high CC values. Most likely these are layers of Bragg scatter, but there are no means to prove that conjecture. Such layers would be classified as clouds by the above algorithms. In Fig. 10.3a, c, and e, the layer between 5.5 and 6.5 km is from Bragg scatter because visually there were no clouds at those heights. The above algorithm would classify this layer as a cloud. To distinguish clouds and Bragg scatter, precise measurements of Z_{DR} could be used. Z_{DR} values from Bragg scatter are close to 0 dB whereas Z_{DR} values from clouds frequently lie in the interval of 0.2 – 0.6 dB. To measure such small Z_{DR} values, the radar has to be calibrated on Z_{DR} precisely. Not every WSR-88D system is at that stage yet.

Layers of Bragg scatter and clouds can be separated by heights. Bragg scatter has not been observed higher than 7 km. So radar echoes located at heights higher than 7 km are from clouds. Echoes from heights lower than 7 km can be from Bragg scatter and clouds. In such a case, they are hard to distinguish.

14. Conclusions

Clouds are one of the critical climatic components, and thus data on clouds obtained from various sensors are valuable. The WSR-88Ds are sufficiently sensitive to observe various types of nonprecipitating clouds. The presence of clouds, the heights of their boundaries, and the wind

and turbulence measurements are valuable information that can be used for climatic studies, cloud modeling, and aviation services. Polarimetric data obtained from the WSR-88Ds can be used for distinguishing clouds from atmospheric biota and for microphysical studies of clouds. The WSR-88D is also sensitive enough to observe nonprecipitating clouds at distances up to 300 km in the long pulse mode (e.g., Fig. 2.1 in section 2). The accuracy of determining cloud boundaries diminishes with range because of increasing radar beam-width. Comparisons of radar data obtained from the WSR-88D with those from the Cloud Profiling Radar show the satisfactory detection of cloud boundaries with the WSR-88D in the short pulse mode at distances up to 100 km (section 8). The short pulse VCPs are advantageous in the measurements of Doppler velocities in clouds because of higher PRFs.

Nonprecipitating clouds can be detected with the WSR-88Ds running the long and short pulse VCPs. In the long pulse VCP, the maximum antenna elevation that allows observing sufficiently thick clouds is 4.5^{o}. With this VCP, the probability of missing thin clouds at altitudes higher than 6 km is about 27% than was obtained from comparisons of the WSR-88D data and satellite CPR (section 8). This condition is mostly due to low elevations angles in VCP31 because the sensitivity of CPR and WSR-88D at a distance of 10 km is about the same (section 8).

Detectability of clouds with the WSR-88D depends on distance. Therefore obtaining the cloud tops and bottoms is more accurate at high antenna elevations. Comparisons of the cloud tops measured at the maximum antenna elevation for VCP31, i.e., 4.5^{o}, with those obtained at elevations higher than 40° shows that the difference in heights may reach 2.5 km (section 2). For the short-pulse VCPs this difference may reach 1 km. So for accurate estimation of the cloud tops in the airport terminal area (60 km from an airport), higher antenna elevations are advantageous. The TDWR radars have a VCP with a maximum elevation of 60°. Our comparisons of data from the WSR-88D and TDWR show that the WSR-88D is not less sensitive in cloud detection than the TDWR, despite a significant difference in the wavelengths (section 9).

Data presented in sections 2 and 3 show that 2D cloud images in forms of a single PPI or RHI do not adequately represent cloud fields. It is frequently difficult to imagine the important cloud features looking at a series of PPIs obtained with a single VCP. A 3D representation of clouds designed from a series of PPIs is more adequate. Three dimensional images of clouds can be rotated and viewed from different perspectives and allow their main features to be examined more quickly. A "read-out" tool could be designed to obtain numerical values of the cloud parameters. Developing such a tool could require sophisticated software (section 3b) and extensive computer resources. To obtain numerical values of cloud parameters, a "read-out" tool is also necessary. The tool is quite sophisticated in 3D (section 3.b). A "read-out" tool could be designed to obtain numerical values of the cloud parameters. Developing such a tool could require sophisticated software (section 3b) and extensive computer resources. One of the issues

viewing 3D radar data, is the "saw-tooth" cloud top shape experienced when working with sufficiently large elevation increments at high antenna elevations

The conclusions below are grouped in three categories. The first contains findings and recommendations that can be implemented into the operational practice in a year's time. The second group contains propositions that can be implemented in a period of 2-3 years. The third group contains findings obtained with special VCPs and requires further studies and additional time.

a. Short term recommendations

While cloud tops and bases are major characteristics, they are inadequate to describe multi-layered clouds. Radar data display advances are needed for both the aviation community as well as future advances in cloud modeling. Currently, the WSR-88D has a reflectivity based Echo Tops algorithm for obtaining the cloud tops. The Multi-Radar Multi-Sensor System (MRMS) provides options to show the reflectivity data in many ways that represent the visible cloud edges. Options such as displaying reflectivity data near 10 dBZ with a data threshold of 2 dB SNR would be possible with the MRMS.

To obtain the lower cloud boundary, an algorithm described in section 13.b should be designed and tested. Layered clouds can be confused with Bragg scatter layers that have similar polarimetric characteristics. Distinguishing these layers could be based on the altitude of the echoes: Bragg scatter is usually observed at heights below 7 km so echoes above 7 km are from clouds. At heights lower than 7 km, there is no reliable approach to separate out clouds and Bragg scatter.

The wind in clouds can be obtained by using the known Velocity-Azimuth-Display (VAD) method. The method works well in a case when cloud echo is in a form of an annular ring (section 10). In this case the Doppler velocity is sufficiently easy to dealias. If the cloud field is patchy, the VAD algorithm depends on how many azimuths are available. This should be studied in the future work.

Z_{DR} cloud data can be used to obtain cloud areas containing plate-like ice particles. Such areas have $Z_{DR} \geq 4$ dB (section 7.b). This is a solid finding, and it can be implemented into the existing HCA sufficiently quickly.

Radar echoes from clouds can also be used to monitor the system Z_{DR}. It is known that cloud particles fall down with their major axes horizontally oriented, on average, so Z_{DR} from clouds must be positive. If the measured Z_{DR} in a cloud is negative, then the system has negative Z_{DR} bias. The algorithm is described in section 12. Table 2 summarizes the short term recommendations.

58

Table 2: Short term recommendations

Proposition	Algorithm	Caveats	Needed work
Cloud tops	Algorithm exists. SNR threshold in the existing algorithm should be reduced to + 2 dB (section 12a)	1.Saw-tooth appearance 2. Possible detection of Bragg scatter layers	1. Algorithm to fill in gaps between the adjacent radials at high elevations. 2. No clear solution.
Cloud lower bounds	Algorithm can be designed from the one that is use for the cloud tops (section 12b)	1.Saw-tooth appearance 2. Possible detection of Bragg scatter layers	1. Algorithm to fill in gaps between the adjacent radials at high elevations. 2. No clear solution.
Winds in clouds	VAD algorithm exists (section 10).	Patchy clouds can cause problems with VAD algorithm	Obtain limits at what VAD is applicable for patchy clouds.
3D cloud imaging	Algorithms exist (sections 3 and 4)	Data in between adjacent radials at high elevations are missing.	Algorithms to fill in gaps between the adjacent radials at high elevations. This could take a time period greater than 1 year.
Identification of the plate-like ice particles	Algorithm: $Z_{DR} >$ 4 dB (section 7.b)	Not known	Modification of the HCA to include the category
Monitoring negative system Z_{DR} bias	Algorithm is described in section 12.	Not known	Needed work seems straightforward because the algorithm has many features similar to the "snow" method used by the ROC to monitor Z_{DR} calibration.

   b. Middle term propositions

   The WSR-88D has a capability to observe very weak echoes from clouds and reliably measure Doppler velocities in weak echoes (section 10). This capability can be used to obtain the atmospheric winds by utilizing the Velocity-Azimuth-Display (VAD) technique. The wind information can complement the data obtained from the wind profilers. For high-altitude clouds, the WSR-88D data is unique because the wind profilers are not capable of getting data from such altitudes. To measure Doppler velocity in weak echoes, the spectral technique that is in use in the wind profilers could be utilized. The second approach could be using algorithms of pattern

recognition. The spectral approach seems to be a more promising technique especially in patchy clouds where patter recognition is not as robust.

Doppler velocity and spectrum width fields in clouds allow mapping areas of strong wind shears, turbulence, and Kelvin-Helmholtz waves that are of interest for the aviation service and cloud physicists (section 5). The spectrum width is a pseudo-scalar, i.e., its value depends on the viewing angle. Algorithms to mitigate this effect should be developed. The middle term propositions are summarized in Table 3 below.

Table 3: Middle term propositions

Proposition	Algorithm	Caveats	Needed work
Using the WSR-88D as a wind profiler	Spectral analysis and pattern recognition	Unknown	Adapt the existing wind profiler spectral algorithms to the WSR-88D. Analyze relevant approaches for pattern recognition.
Detection of turbulence and Kelvin-Helmholtz waves	An analysis of the Doppler velocity field along with the spectrum width field.	1. The detectability depends on the range of observation. 2. The detectability depends on the angle between the radar beam and the mean wind flow.	1. Consider the spectrum width field normalized by range that can supposedly represent the features independent of distance. 2. No easy fix.
3D cloud imaging	Algorithms exist (sections 3 and 4)	Data in between adjacent radials at high elevations are missing.	This work could take more than 1 year, so it is placed here.

c. Propositions that require special VCPs

Elevation dependences of Z_{DR} and CC in clouds can deliver information on the shape of particles, their bulk ice density, and the intensity of flutter (section 7.b). This information is very valuable for cloud modeling, but to obtain it, radar scans at high elevations (up to 50°) are needed. That is, a special VCP should be designed for such a retrieval. This process can be done upon requests from the cloud modeling community.

Transition from clouds to precipitation is one of the major meteorological problems: when and where precipitation begins, and what triggers precipitation. Radar data can deliver valuable information on such processes but the update time of radar data should be about 1 minute which is not achievable with the WSR-88D. This can be accomplished with phased array weather radar, which is under development. The special VCP propositions are summarized in Table 4 below.

Table 4: Propositions that require special VCPs

Proposition	Algorithm	Caveats
Information on ice particle habits	Elevation dependences of Z_{DR} and CC (section **Error! eference source not found.**)	Elevations from 30 to 50° should be scanned.
Transitioning from cloud to precipitation	Radar observations with update time of about 1 min.	Such an update time can be achieved with phased array weather radar.

**15. Appendix: Variables of STAR weather radar measured above the melting layer**

This appendix contains supporting equations used in section **Error! Reference source not ound.** to retrieve the parameters of cloud ice particles using radar polarimetric variables as functions of the antenna elevation angle. General dependencies of polarimetric moments upon elevation are derived in this appendix.

It is often said that the dual-polarization WSR-88D transmits and receives horizontally and vertically polarized waves simultaneously, implying a frame affixed to the Earth's surface and low antenna elevation angles. At higher elevations, the horizontally polarized wave remains horizontal, but the orthogonally polarized wave has vertical and horizontal components in that frame. This polarimetric configuration is called Simultaneous Transmit And Receive (STAR). The main parameters of the transmitted wave are expressed in a reference frame affixed to the radar antenna. In this frame, it is convenient to use terms horizontally and vertically polarized waves always because they do not change with antenna elevation. The latter parameter is defined in a frame affixed to the Earth's surface. This frame is also natural for characterizing orientations and motions of atmospheric hydrometeors. To consider the scattering problem using parameters natural for radar and hydrometeors, various reference frames should be introduced first.

a. Reference frames and geometry of scattering

It is convenient to consider a hydrometeor in Cartesian grid OXYZ (Fig. 15.15.1) with axis Z orthogonal to the ground so that plane XOY is horizontal. In this reference frame, a hydrometeor has a canting angle (θ in Fig. 15.15.1) and falls down along Z axis in still air. Axis OX is horizontal and chosen in a plane formed by the direction of incident radar radiation (vector $\vec{k}$ in the figure) and vertical axis OZ. Axis Y is chosen to make the frame a right coordinate system. Coordinate system OXYZ will be called the natural frame. Orientation of a hydrometeor in the natural frame is characterized with angles θ and φ of hydrometeor's axis OZ'. For many types of hydrometeors, this axis is their axis of symmetry. Hydrometeors flutter in the air, so the orientation angles θ and φ vary. These variations can be described with probabilities that will be introduced later.

Scattering problems have the simplest form in a reference frame with a center inside the scatterer. This frame is called herein the particle frame. Many hydrometeors have a symmetry axis. For such scatterers, it is convenient to choose one of the frame axes along the symmetry axis. For a plate-like particle (Fig. 15.15.1), the particle frame is OX'Y'Z' with axis OZ' oriented along the particle's symmetry axis.
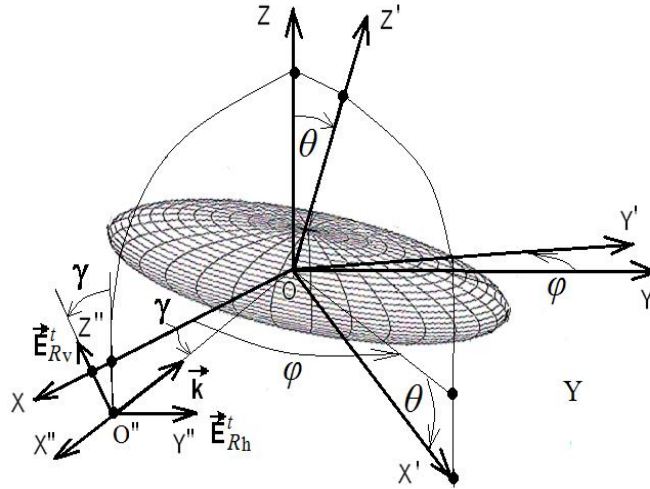
Fig. 15.15.1: Natural frame OXYZ, particle frame OX'Y'Z', and radar frame O''X''Y''Z''.

In a frame affixed to the radar antenna, STAR radar transmits waves with horizontal and vertical polarizations (E_{Rh}^t and E_{Rv}^t in Fig. 15.15.1) regardless of antenna elevation. Superscript t denotes transmitted waves and the subscripts R, N, and P will be used to indicate the radar, natural, and particle reference frames respectively. The subscripts h and v will be used to indicate horizontal and vertical wave amplitudes. The radar frame is O''X''Y''Z'' (Fig. 15.15.1). Axis O''X'' lies in plane OXZ of the natural frame. The frames' origin O'' can be moved to O without any loss of generality. Angle γ between axes OX and O''X'' (or OX'') is the antenna elevation angle. In the natural frame, E_{Rh}^t is horizontal always but E_{Rv}^t is vertical at the zero elevation angle, and becomes horizontal at an elevation of 90°.

b. System differential phases in transmit and receive

The STAR radar configuration has two separate channels for the waves of different polarizations. These waves have the differential phase in transmit ψ_t, which is determined in the far field zone of the antenna. If the propagation media (e.g., clear air at S band) does not shift their phases, ψ_t is the incident phase ψ_i for scattering. If the media shifts the phase by the two-way propagation phase Φ_{DP}, the incident phase is $\psi_i = \psi_t + \Phi_{DP}/2$. The amplitudes of the transmitted waves can be set to unity without any loss of generality due to linearity of the scattering problem. The relative intensity of the amplitudes is determined during Z_{DR} calibration. So in the radar frame, the transmitted waves can be represented as vector $\boldsymbol{E}_R^t$ with zero x-component and unit amplitudes:

$$\boldsymbol{E}_R^t = \begin{pmatrix} 0 \\ 1 \\ e^{j\psi_t} \end{pmatrix} \tag{1}$$

Bold letters are used herein to represent vectors and matrixes in a compact form and usual letters are used for the components of vectors and matrixes.

The radar receiver channels also contain waveguides of different lengths that causes phase shift ψ_r upon reception. Let $\boldsymbol{E}_R^s$ be the amplitude vector of scattered waves on the antenna input. Then amplitudes $\boldsymbol{E}_R^r$ at the input to the radar digitizer can be written using receive matrix $\boldsymbol{V}$ as,

$$\boldsymbol{E}_R^r = \boldsymbol{V}\boldsymbol{E}_R^s = \begin{pmatrix} 0 & 1 & e^{j\psi_r} \end{pmatrix} \begin{pmatrix} E_{Rx}^s \\ E_{Ry}^s \\ E_{Rz}^s \end{pmatrix} \tag{2}$$

Since the signal paths in transmit and receive are different, phases ψ_t and ψ_r are different in general. Sum $\psi_t + \psi_r$ is the system differential phase ψ_{sys}, which can be measured as the differential phase in the nearest to radar fringes of echoes containing small droplets. Separate measurements of ψ_t and ψ_r are complicated technical problems.

c. Backscattering

In the radar frame, the amplitudes of transmitted waves are given by (1). The amplitudes of incident waves in the radar frame can be obtained using the transmission matrix $\boldsymbol{T}_R$ as, $\boldsymbol{E}_R^i = \boldsymbol{T}_R \boldsymbol{E}_R^t$. If the amplitudes of depolarized waves in forward direction are much weaker than the amplitude of incident radiation, matrix $\boldsymbol{T}_R$ can be written in a diagonal form as,

$$\boldsymbol{T}_R = \begin{pmatrix} 1 & 0 & 0 \\ 0 & \Gamma_{\mathrm{h}} & 0 \\ 0 & 0 & \Gamma_{\mathrm{v}} \exp(j\Phi_{\mathrm{DP}}/2) \end{pmatrix}, \tag{3}$$

where Γ_{h} and Γ_{v} (positive numbers less than 1) are attenuation coefficients in the radar frame. Phase Φ_{DP} is usually measured for two-way signal path thus (3) contains ½ in the exponent because $\boldsymbol{T}_R$ is applied for the incident waves. Matrix $\boldsymbol{T}_R$ can be generalized by including depolarization in propagation (e.g., section 4.5 in Bringi and Chandrasekar 2001).

The scattering matrix $\boldsymbol{S}$ of a single hydrometeor frequently has the simplest form in the particle frame. Many practically important hydrometeors have symmetric shapes, e,g., raindrops, plate-like ice particles, ice needles, and many dendrites. Let E_{Px}^i, E_{Py}^i, and E_{Pz}^i are the components of the incident wave in the particle frame, then the scattered wave has components E_{Px}^s, E_{Py}^s, and E_{Pz}^s obtained as,

$$\begin{pmatrix} E_{Px}^s \\ E_{Py}^s \\ E_{Pz}^s \end{pmatrix} = \begin{pmatrix} S_{\mathrm{hh}} & 0 & 0 \\ 0 & S_{\mathrm{hh}} & 0 \\ 0 & 0 & S_{\mathrm{vv}} \end{pmatrix} \begin{pmatrix} E_{Px}^i \\ E_{Py}^i \\ E_{Pz}^i \end{pmatrix}, \tag{4}$$

which can be written also in a compact form as, $E^s_P = SE^i_P$. It is seen from (4) that symmetric particles do not depolarize the incident wave in the particle frame.

Consider propagation and scattering in various frames. Such an approach is frequently used in antenna problems (e.g., Mott, 1992, chapter 4.13) and was utilized by Matrosov et al. (2001) for radar measurements of depolarized signals. Vivekanandan et al. (1991) utilized this technique in backscatter in terms of the Muller matrix without considering the incident phase. Vertical radar remote sensing using wave decomposition was studied by Tang and Aydin (1995). Consider transmission of radar waves, their propagation, and scattering sequentially. Radar transmits the waves represented by (1). These waves propagate through the media and the incident waves in the radar frame are $E^i_R = T_R E^t_R$. To apply (4) for scattering, the incident waves in the radar frame should be transformed into the particle frame. This transformation can be accomplished in two steps: the first one is transforming the waves from radar frame to the natural one and then from the natural frame to the particle one. The first step is described by matrix equation $E^i_N = U E^i_R$, where U is a rotation matrix. The second step can be represented as, $E^i_P = W E^i_N$ with another rotation matrix W. Scattering is described by (4), i.e., $E^s_P = S E^i_P$. These waves should be converted back to the radar frame, which is done by transposed matrixes W^T and U^T. The scattered waves travel back to the radar, and at the radar antenna they are $E^s_R = T_R U^T W^T E^s_P$. The radar shifts the phases in receive according to (2) and the received amplitudes are $E^r_R = V E^s_R$. Substituting the above matrix equations into the latter one yield the amplitudes of received waves:

$$E^r_R = V T_R U^T W^T S W U T_R E^t_R. \tag{5}$$

The latter is the general solution to the backscattering problem. Matrixes U and W have the following forms [e.g., Mischenko et al. 2002, section 2.4]:

$$U = \begin{pmatrix} \cos\gamma & 0 & \sin\gamma \\ 0 & 1 & 0 \\ -\sin\gamma & 0 & \cos\gamma \end{pmatrix}, \tag{6}$$

$$W = \begin{pmatrix} \cos\theta\cos\varphi & \cos\theta\sin\varphi & -\sin\theta \\ -\sin\varphi & \cos\varphi & 0 \\ \sin\theta\cos\varphi & \sin\theta\sin\varphi & \cos\theta \end{pmatrix}. \tag{7}$$

Eq. (5) is applicable for any scatterer (any S) and propagation media (any T_R). For a symmetrical scatter having scattering matrix (4) and non-depolarizing propagation media (3), the amplitudes of received signals in the horizontal and vertical channels are obtained from (5) as,

$$E_h = S_{hh}\Gamma_h + \Delta S B \sin\theta\sin\varphi, \tag{8}$$

$$E_v = [S_{hh}\exp(j\psi_i)\Gamma_v + \Delta S B(\sin\gamma\sin\theta\cos\varphi + \cos\gamma\cos\theta)]\exp(j\psi_r + j\Phi_{DP}/2), \tag{9}$$

with $\Delta S = S_{vv} - S_{hh}$ and

$$B = \Gamma_v \sin\gamma \sin\theta \cos\varphi \, \exp(j\psi_i) + \Gamma_h \sin\theta \sin\varphi + \Gamma_v \cos\gamma \cos\theta \, \exp(j\psi_i) \qquad (10)$$

To simplify notations, received amplitudes $E_{h,v}$ in (8) and (9) are written without the superscript and with one subscript indicating polarization. The solution (8-9) is expressed in terms of the scattering matrix elements in the particle frame, incident differential phase, orientation angles of the scatterer in the natural frame, antenna elevation angle, and radar phases in transmit and receive. It is seen from (8) and (9) that the measured radar variables, which are products of the amplitudes [see (25)-(28) below], do not depend on the phase in receive because this phase enters in (9) as a multiplicative exponent. In contrast, ψ_t affects both the amplitudes and phases. So if radar has a capability of varying ψ_t, such variations will alter the radar variables that can be used to obtain additional information about scatterers. Such a capability is discussed in section 7c.

d. Forward scattering

The differential phase upon scattering in forward direction is an important characteristic of the media. The specific differential phase K_{DP} determined for scatterers in the radar volume is

$$K_{DP} = \lambda N \mathrm{Re}(f_{Rh} - f_{Rv}) \quad [\mathrm{rad\ m}^{-1}] \qquad (11)$$

with λ being the wavelength [m], N the number concentration [m^{-3}], and f_{Rh}, f_{Rv} the scattering amplitudes in forward direction. Eq. (11) should be generalized for a case with incident differential phase ψ_i. Let $\boldsymbol{E}^i_{Rf}$ and $\boldsymbol{E}^s_{Rf}$ be the amplitudes of incident and scattered waves in the forward direction. Then the phase change in the scattered waves in forward direction is obtained as, $\arg[\boldsymbol{E}^s_{Rf} \exp(-j\psi_i)]$ and K_{DP} is obtained as,

$$K_{DP} = \lambda N \mathrm{Re}[< E^s_{Rfh} > - < E^s_{Rfv} > \exp(-j\psi_i)] \, , \qquad (12)$$

where $\qquad \psi_i = \psi_t + \Phi_{DP}/2 \qquad (13)$

and the angular brackets stand for averaging over sizes and orientations.

The amplitudes of the incident waves in the radar frame are $\boldsymbol{E}^i_R = \boldsymbol{T}_R \boldsymbol{E}^t_R$. For scatterers having a symmetry axis, the scattering matrix $\boldsymbol{S}_f$ in forward direction has a form similar to the one written in (4) for backscattering. Thus, the amplitudes of scattered waves $\boldsymbol{E}^s_P$ in forward direction in the particle frame can be written as,

$$\begin{pmatrix} E^s_{Px} \\ E^s_{Py} \\ E^s_{Pz} \end{pmatrix} = \begin{pmatrix} f_{Ph} & 0 & 0 \\ 0 & f_{Ph} & 0 \\ 0 & 0 & f_{Pv} \end{pmatrix} \begin{pmatrix} E^i_{Px} \\ E^i_{Py} \\ E^i_{Pz} \end{pmatrix} , \qquad (14)$$

where $f_{Ph,Pv}$ are the forward scattering amplitudes in the particle frame. By converting the incident waves in the radar frame to the particle frame with matrixes $\boldsymbol{U}$ and $\boldsymbol{W}$, the forward scattered waves in the particle frame can be written as, $\boldsymbol{E}^s_P = \boldsymbol{S}_f \boldsymbol{W} \boldsymbol{U} \boldsymbol{T}_R \boldsymbol{E}^t_R$. These waves should be converted to the radar frame using matrixes $\boldsymbol{U}^\mathrm{T}$ and $\boldsymbol{W}^\mathrm{T}$. The result is

$$\boldsymbol{E}_{Rf}^{s} = \boldsymbol{U}^{T}\boldsymbol{W}^{T}\boldsymbol{S}_{f}\boldsymbol{W}\boldsymbol{U}\boldsymbol{T}_{R}\boldsymbol{E}_{R}^{t} \tag{15}$$

The latter field should be used in (11). For a symmetrical scatterer, one obtains

$$E_{\mathrm{fh}} = f_{\mathrm{Ph}}\Gamma_h + \Delta f_P B\sin\theta\sin\varphi, \tag{16}$$

$$E_{\mathrm{fv}} = [f_{\mathrm{Ph}}\exp(j\psi_i)\Gamma_v + \Delta f_P B(\sin\gamma\sin\theta\cos\varphi + \cos\gamma\cos\theta)]\exp(j\psi_r + j\Phi_{\mathrm{DP}}/2), \tag{17}$$

with $\Delta f_P = f_{\mathrm{Pv}} - f_{\mathrm{Ph}}$ and B was determined in (10). To obtain K_{DP}, eq. (11) should be used with averaged fields (16)-(17) over sizes and orientations (see section 7c for zero mean canting angle).

e. Negligible attenuation

In some situations, attenuation in propagation media can be neglected, e,g., at short distances in precipitation and for cm-wavelength radiation propagating in clouds. In such cases, $\Gamma_{Rh} \approx 1$ and $\Gamma_{Rh} \approx 1$ and (8)-(10) are written as,

$$E_{\mathrm{h}} = S_{\mathrm{hh}} + \Delta SB\sin\theta\sin\varphi, \tag{18}$$

$$E_{\mathrm{v}} = [S_{\mathrm{hh}}\exp(j\psi_i) + \Delta SB(\sin\gamma\sin\theta\cos\varphi + \cos\gamma\cos\theta)]\exp(j\psi_r + j\Phi_{\mathrm{DP}}/2), \tag{19}$$

with

$$B = \sin\gamma\sin\theta\cos\varphi \exp(j\psi_i) + \sin\theta\sin\varphi + \cos\gamma\cos\theta \exp(j\psi_i) \tag{20}$$

At $\psi_t = \psi_r = 0$, and $\Phi_{\mathrm{DP}}= 0$, eqs. (18-19) reduce to

$$E_{\mathrm{h}} = S_{\mathrm{hh}} + \Delta S\sin\theta\sin\varphi(\sin\gamma\sin\theta\cos\varphi + \sin\theta\sin\varphi + \cos\gamma\cos\theta), \tag{21}$$
$$E_{\mathrm{v}} = S_{\mathrm{hh}} + \Delta S[(\sin\gamma\sin\theta\cos\varphi + \cos\gamma\cos\theta)^2 + \sin\gamma\sin^2\theta\sin\varphi\cos\varphi + \cos\gamma\sin\theta\cos\theta\sin\varphi]. \tag{22}$$

Eq. (21) can be represented as a sum of the primary (G_h) and depolarized (D_h) scattered components, i.e., $E_{\mathrm{h}} = G_{\mathrm{h}} + D_{\mathrm{h}}$, with

$$G_{\mathrm{h}} = S_{\mathrm{hh}} + \Delta S\sin^2\theta\sin^2\varphi \quad , \tag{23}$$

$$D_{\mathrm{h}} = S_{\mathrm{hh}} + (\Delta S/2)(\sin\gamma\sin^2\theta\sin2\varphi + \cos\gamma\sin2\theta\sin\varphi) \ . \tag{24}$$

The latter two equations coincide with eq. (2.53) from Bringi and Chandrasekar (2001). Similar decomposition can be done for vertically polarized component (22). Note that (21) and (22) do not account for differential phases ψ_t, ψ_r, and Φ_{DP}; eqs. (8) and (9) contain the phases.

f. Radar variables at zero mean canting angle

Eqs. (8)-(9) and (15) are valid for arbitrary orientation of scatterers; they can be used for hydrometeors having nonzero mean canting angle. Raindrops wobble and ice hydrometeors flutter in the air so the instantaneous canting angle (θ in Fig. 15.15.1) alters. In many important cases, the mean canting angle is zero. This is usual for raindrops falling through layers of not strong wind shears. Many ice hydrometeors fall down with their largest size being horizontal in the mean (Pruppacher and Klett 1997, chapter 10) in the absence of strong electrical fields in clouds. Due to the importance of such cases, zero mean canting angles is considered in this section.

The radar volume contains many scatterers that change their orientations over time. The radar variables are obtained by time averaging of the products of amplitudes E_h and E_v of the received waves. Due to ergodicidy, time averaging is equivalent to spatial and orientation averaging. The latter can be done by introducing probability $P(\theta, \varphi)\sin\theta d\theta d\varphi$ to have orientation angles in intervals from θ to $\theta + d\theta$ and from φ to $\varphi + d\varphi$. Assuming independence of orientations and particle sizes, averaging over orientations and sizes can be done separately. To average over orientations, assume independence of the θ- and φ-distributions and the totally random (uniform) φ-distribution, for which $<\sin\varphi> = <\sin^3\varphi> = 0$, $<\sin^2\varphi> = 1/2$, $<\sin^4\varphi> = 3/8$, and $< \sin^2\varphi\cos^2\varphi> = 1/8$, where angular brackets stand for orientation averaging. The mean received powers P_h and P_v in the respective channels are obtained as,

$$P_h = C_r <| E_h |^2> \text{ and } P_v = C_r <| E_v |^2> \tag{25}$$

with C_r being the radar constant, which will be omitted in the following discussion without any loss of generality. Z, Z_{DR}, the measured differential phase φ_{DP}, and ρ_{hv} are obtained as,

$$Z = 10 \log_{10}[(P_h - n_h)/n_h] , \tag{26}$$

$$Z_{DR} = 10 \log_{10}[(P_h - n_h)/(P_v - n_v)] , \tag{27}$$

$$R_{hv} =< E_h^* E_v > , \tag{28}$$

$$\varphi_{DP} = \arg(R_{hv}) , \tag{29}$$

$$\rho_{hv} = |R_{hv}|/[(P_h - n_h)(P_v - n_v)]^{1/2} , \tag{30}$$

where n_h and n_v are the mean noise powers in the channels. To measure the propagation differential phase, the measured phase φ_{DP} should be multiplied by $\exp(-\psi_{sys})$ so that the estimate of the propagation phase is

$$\widehat{\Phi}_{DP} = \arg[R_{hv} \exp(-j\psi_{sys})], \tag{31}$$

where the circumflex indicates the estimate that can differ from actual Φ_{DP} by the phase upon scattering δ. Averaging in (25) and (28) yields

$$P_h = \Gamma_h^2 < |S_{hh}|^2 > +J_1 Re(< S_{hh}^* \Delta S >)+< |\Delta S|^2 > C_1], \tag{32}$$

67

$$P_{\mathrm{v}} = \Gamma_v^2[< |S_{\mathrm{hh}}|^2 > +2Re(< S_{\mathrm{hh}}^*\Delta S >)C_2 + < |\Delta S|^2 > C_3] \,, \tag{33}$$

$$R_{\mathrm{hv}} = \Gamma_h\Gamma_v\exp\left(j\Phi_{\mathrm{DP}} + j\psi_{sys}\right)[< |S_{\mathrm{hh}}|^2 > +Re(< S_{\mathrm{hh}}^*\Delta S >)C_4 + \\ j\mathrm{Im}(< S_{\mathrm{hh}}^*\Delta S >)C_5 + (< |\Delta S|^2 >)C_6], \tag{34}$$

$$C_1 = [4(J_1 - J_2)\xi + 3J_2 + (5J_2 - 4J_1)\xi\sin^2\gamma]/8 \,, \tag{35a}$$

$$\xi = \Gamma_v^2/\Gamma_h^2, \tag{35b}$$

$$C_2 = 1 - J_1 - (1 - 3J_1/2)\sin^2\gamma \,, \tag{35c}$$

$$C_3 = 1 - 2J_1 + J_2 + (J_1 - J_2)\xi^{-1} - [(2 - 7J_1 + 5J_2) + (5J_2/8 - J_1/2)\xi^{-1}]\sin^2\gamma + \\ (1 - 5J_1 + 35J_2/8)\sin^4\gamma \,, \tag{35d}$$

$$C_4 = 1 - J_1/2 - (1 - 3J_1/2)\sin^2\gamma \,, \tag{35e}$$

$$C_5 = (1 - 3J_1/2)\cos^2\gamma \,, \tag{35f}$$

$$C_6 = \exp(-j\psi_i)[J_1 - J_2 + (5J_2/4 - J_1)\sin^2\gamma\cos\psi_i] \,, \tag{35g}$$

where $\mathrm{Re}(x)$ and $\mathrm{Im}(x)$ stand for the real and imaginary parts of x and

$$J_1 = < \sin^2\theta >, \quad J_2 = < \sin^4\theta > \tag{36}$$

are the moments of the θ-distribution. The primary measurables (32)-(34) of the STAR radar are explicitly expressed via the elements of scattering matrix in the particle frame, moments (36) of the θ-distribution determined in the natural frame, elevation angle γ, propagation differential phase Φ_{DP}, and system differential phases in transmit and receive ψ_t and ψ_r.

It is seen from (32) and (33) that P_{h}, P_{v}, and correspondingly Z_{DR} do not depend upon incident differential phase. This is the consequence of the uniform φ-distribution and the zero mean canting angle. If one (or both) of these conditions is not satisfied, ψ_i affects the measured powers and Z_{DR}. Eq. (34) shows that ψ_i affects R_{hv} even at the uniform φ-distribution. This can be used to obtain information on scatterers from measurements of Z_{DR} and R_{hv}. Such an approach was used by Melnikov and Straka (2013) to obtain the axis ratios of ice cloud particles. This is discussed further in the next section.

Eq. (29) determines also the differential phase upon scattering δ. This phase is the deviation of the measured phase φ_{DP} from the propagation phase Φ_{DP}. Combining (31) and (34) yields

$$\delta = \arg[< |S_{\mathrm{hh}}|^2 > +\mathrm{Re}(< S_{\mathrm{hh}}^*\Delta S >)C_4 + j\mathrm{Im}(< S_{\mathrm{hh}}^*\Delta S >)C_5 + < |\Delta S|^2 > C_6], \tag{37}$$

Equations for K_{DP} and differential attenuation A_{DP} are:

$$K_{\text{DP}} = N\lambda(3J_1/2 - 1)\cos^2\gamma \; \text{Re}(f_{P\text{h}} - f_{P\text{v}}) \; \text{(rad m}^{-1}),\qquad(38)$$

$$A_{\text{DP}} = N\lambda(3J_1/2 - 1)\cos^2\gamma \; \text{Im}(f_{P\text{h}} - f_{P\text{v}}) \; \text{(m}^{-1}).\qquad(39)$$

In the derivation of (8)-(9) and (16)-(17), independence of scatterers over the distance from radar was utilized. In averaging products of amplitudes (8) and (9) of scattered waves, the amplitudes should be multiplied by $\exp(j2kr_n + j\omega t)$ with r_n being the distance from radar to n^{th} scatterer, ω the radar frequency, and t the time. These multipliers enter into the products as $\exp[j2k(r_n - r_m)]$. The scatterers move relative to each other in the radar volume and $r_{n,m}$ vary. Assuming independence r_n from r_m ($n \neq m$), we get $< \exp[j2k(r_n - r_m)] >= \delta_{mn}$, i.e., the Kroneker delta. Thus the contributions to the powers and correlation function sum up incoherently. The same is valid for K_{DP} and A_{DP}.

g. Distributions of the canting angles

Distributions of canting angle θ can be described with the Gaussian, Fisher, and axial bell-shaped functions (e.g., Bringi and Chandrasekar 2001, section 2.3.6). The truncated Gaussian distribution is defined in the interval $0 - \pi$ as,

$$P(\theta) = D^{-1}\exp[-(\theta - < \theta >)^2/2\sigma_\theta^2],\qquad(40)$$

$$D = \int_0^\pi \sin\theta \, \exp[-(\theta - < \theta >)^2/2\sigma_\theta^2]d\theta,\qquad(41)$$

where $<\theta>$ is the mean canting angle and σ_θ is a parameter depending on the width of distribution. For narrow distributions, the width equals σ_θ. This distribution was used by Vivekanandan et al. (1991), Matrosov et al. (2001), and Ryzhkov et al. (2011) among others. Moment J_1 from (31) for zero mean canting angle is

$$J_1 = < \sin^2\theta >= D^{-1}\int_0^\pi \sin^3\theta \exp(-\theta^2/2\sigma_\theta^2)d\theta.\qquad(42)$$

Moment J_2 is obtained similarly. Distribution (40) is used herein. For non-fluttering plate-like scatterers, $J_1 = J_2 = 0$, and $J_1 = J_2 = 1$ for columnar particles oriented horizontally. For the totally random distribution, $J_1 = 2/3$ and $J_2 = 8/15$. Moments J_1 and J_2 are shown as functions of the width of distribution in Fig. 15.2 with the solid lines.
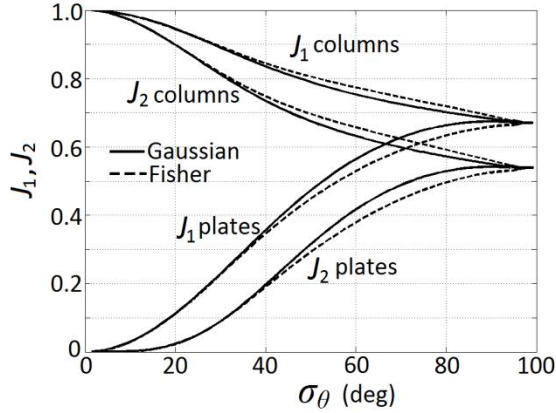
Fig. 15.15.2: Moments J_1 and J_2 shown as functions of the width of the Gaussian (solid lines) and Fisher (dashed lines) distributions for plate-like and columnar scatterers.

The Fisher distribution naturally describes probabilities on a sphere (Fisher 1953). For plate-like particles with zero mean canting angle, $P(\theta, \varphi)$ is a function of θ only:

$$P(\theta) = \frac{\mu}{2\sinh(\mu)} \exp(\mu cos\theta), \quad \mu \geq 0, \tag{43}$$

where parameter μ can be represented via the width of distribution σ_θ:

$$\sigma_\theta^2 = \int_0^\pi \theta^2 P(\theta) \sin\theta d\theta. \tag{44}$$

For plate-like particles, the moments from (31) are

$$J_1 = \frac{2}{\mu}\left[\coth\mu - \frac{1}{\mu}\right], \quad J_2 = \frac{4}{\mu^2}(2 - 3J_1) \qquad . \tag{45}$$

For columns oriented preferably horizontally, $\langle\theta\rangle = 90^\circ$ and the Fisher distribution depends on θ and φ. In this case, averaging over θ and φ cannot be separated and moments J_1 and J_2 are obtained numerically. This feature makes the application of the distribution for columnar particles cumbersome. Moments J_1 and J_2 as a function of the width of distribution are shown in Fig.14.2 for columnar and plate-like scatterers. One can see that the difference in the moments of the Gaussian and Fisher distributions can be considered insignificant for the scattering problems under consideration here.

16. References

Bieringer, P. E., B. Martin, B. Collins, and J. Shaw, 2004: Commercial aviation encounters with severe low altitude turbulence. *Proc. 11th Conf. on Aviation, Range and Aero. Meteorol.*, Paper #11.3, 8 pp.

Bohne, A. R. 1981: Radar detection of turbulence in thunderstorm. *Report of the Air Force*

Geophysics Laboratory, AFGL-TR-81_0102, 62 pp.

Børresen, J. A. 1971: Doppler radar study of shear zones and turbulence in a snowstorm. *J. Applied Meteor.,* **10**, 433 – 442.

Brewster, K. A., and D. S. Zrnić, 1986: Comparison of eddy dissipation rates from spatial spectra of Doppler velocities and Doppler spectrum widths. *J. Atmos. Ocean. Technol.,* **3**, 440 - 452.

Bringi, V. N. and V. Chandrasekar, 2001: *Polarimetric Doppler Weather Radar. Principles and Applications.* Cambridge University Press. 636 pp.

Chapman, D., and K. A. Browning, 1999: Release of potential shearing instability in warm frontal zones. *Quart. J. Royal Meteor. Soc.,* **125**, 2265-2288.

Chapman, D., and K. A. Browning, 2001: Measurements of dissipation rate in frontal zones. *Quart. J. Royal Meteor. Soc.,* 127, 1939-1959.

Clothiaux, E.E., M.A. Miller, B.A. Albrecht, T.P. Ackerman, J. Verlinde, D.M. Babb, R.M. Peters, and W.J. Syrett, 1995: An evaluation of a 94-GHz radar for remote sensing of cloud properties. *J. Atmos. Oceanic Technol.*, **12**, 201-229.

Cornman, L. B., J. Williams, G. Meymaris, and B. Chorbajian, 2003: Verification of an airborne Doppler radar turbulence detection algorithm. *Sixth Int. Symp. Tropospheric Profiling,* Leipzig, Germany, German Weather Service, 9-11.

Doviak, R. J. and D. S. Zrnić, 2006: *Doppler radar and weather observations*. 2nd ed., Dover Publications, Inc., Mineola, NY. 562 pp.

Evans, J. E., 1985: Weather Radar Studies, Dept. of Transp. Rpt. "DOT/FAA-PM-85-16", 48 pp. Document is available from the National Technical Information Service, Springfield, VA, 22161.

Fang, M., R. J. Doviak, and V. M. Melnikov, 2004: Spectrum widths measured by WSR-88D: Error sources and statistics of various weather phenomena. *J. Atmos. Oceanic Technol.* **21**, 888-904.

Fang, M., R. J. Doviak, 2008: Coupled contributions in the Doppler radar spectrum width equation. *J. Atmos. Ocean. Technol*.

Fisher, R.A., 1953: Dispersion on a sphere. *Proc. Roy. Soc. London* Ser. A., **217**, 295-305.

Gossard, E.E. and W. H. Hook, 1975: *Waves in the atmosphere; atmospheric infrasound and gravity waves – their generation and propagation.* Elsevier, N.Y., 532 pp.

Gossard, E. E., and R. G. Strauch, 1983: *Radar observations of clear air and clouds*. Elsevier, 280 pp.

Hamazu, K., H. Hashiguchi, T. Wakayama, T. Matsuda, R. J. Doviak, and S. Fukao, 2003: A 35-GHz scanning Doppler radar for fog observations. *J. Atmos. and Oceanic Technol.,* **20**, 972-986.

Hamilton, D. W., and F. H. Proctor, 2002: Convectively induced turbulence encounters during NASA's 2000 fall flight experiments. *Preprints 10th Conf. Aviation, Range, and Aerospace Meteorology*, AMS, 371-374.

Hamilton, D. W., and F. H. Proctor, 2006a: Progress in the development of an airborne turbulence detection system. *Preprints 12th Conf. Aviation, Range, and Aerospace Meteorology*, AMS, P6.5.

Hamilton, D. W., and F. H. Proctor, 2006b: Airborne turbulence detection system certification tool set. *44th AIAA Aerospace Sciences Meeting.* Reno, Nevada, paper: AIAA 2006-75.

Hocking, W. K., 1983: On the extraction of atmospheric turbulence parameters radar backscatter

Doppler spectra—I. Theory. *J. Atmos. Terr. Phys*., **45**, No.2/3, 89-102.

Hocking, W. K., 1988: Two years of continuous measurements of turbulence parameters in the upper mesosphere and lower thermosphere made with a 2 MHz radar. *J. Geophys. Res.,* **93**(D3), 2475-2491.

Hocking, W.K., 1999: "The Dynamical Parameters of Turbulence Theory as they apply to Middle Atmosphere Studies", Earth, Planets and Space, 51, 525-541.

Hocking, W. K, and P. K. L. Mu, 1997: Upper and middle tropospheric kinetic energy dissipation rates from measurements of $\bar{C}_n^2$ — review of theories, *in-situ* investigations, and experimental studies using the Buckland Park atmospheric radar in Australia. *J. of Atmos. and Solar-Terrestrial Phys.* 5**9**, No. 14, pp 1779-1803.

Hogan, R.J., and A. J. Illingworth, 2003: Parameterizing Ice Cloud Inhomogeneity and the Overlap of Inhomogeneities Using Cloud Radar Data. *J. Atmos. Sci.*, **60**, 756–767.

Holloway, C. L., R. J. Doviak, S. A. Cohn, and R. J. Lataitis, 1996: Retrieval of boundary-layer turbulence using spaced-antenna wind profilers. *Proc. of the IGARSS*, 27-31 May 1996, Lincoln, Nebraska. IEEE, New York, NY.

Holt, A. R., 1984: Some factors affecting the remote sensing of rain by polarization diversity radar in 3- to 35-GHz frequency range. *Radio Sci*., **47**, 1399–1421.

Istok, M. J., and Doviak R. J., 1986: Analysis of the relation between Doppler spectra width and thunderstorm turbulence. *J. Atmos .Sci.*, **48,** 2199-2214.

Kajikawa, M., 1976: Observation of falling motion of columnar snow crystals. *J. Meteor. Soc. Japan,* **54,** 276–283.

Kollias, P., E.E. Clothiaux, M.A. Miller, B. A. Albrecht, G.L. Stephens, and T.P. Ackerman, 2007: Millimeter-wavelength radars: new frontier in atmospheric cloud and precipitation research. *Bull. Amer. Meteorol. Soc.*, 1608-1624.

Kropfli, R. A., and R. D. Kelly, 1996: Meteorological research applications of mm-wave radar. *Meteor. Atmos. Phys.,* **59,** 105–121.

Labitt, M., 1981: Coordinated radar and aircraft observations of turbulence. *Proj. Rep. ATC 108,* MIT, Lincoln Lab., Cambridge, 35 pp.

Lee , J. T.,1977: Application of Doppler radar to turbulence measurements which affect aircraft. *Federal Aviation Administration Report.* FAA-RD-77-145, 45 pp.. Document is available from the National Technical Information Service, Springfield, VA, 22161.

Lee , J. T., D. Carpenter, 1979: 1973-1977 Rough Rider Turbulence-Radar Intensity Study. *Federal Aviation Administration Report.* FAA-RD-78-115, 27 pp.. Document is available from the National Technical Information Service, Springfield, VA, 22161.

Lhermitte, R. M., and D. Atlas, 1961: Precipitation motion by pulse Doppler radar. *Proc. Weather Radar Conf., 9th, pp.218-223.*

Mahapatra, P., 1999: *Aviation Weather Surveillance Systems*. *IEE Radar, Sonar, Navigation, and Avionics Series 8.*, Co-publishers: IEE and AIAA, 458 pp.

Matrosov, S.Y., R.A. Kropfli, B.E. Marner, and B.W. Bartram, 2001: On the use of radar depolarization ratios for estimating shapes of ice hydrometeors in winter clouds. *J. Appl. Meteor.*, **40**, 479-490.

Matrosov, S. Y., R. F. Reinking, and I. V. Djalalova, 2005: Inferring fall attitudes of pristine dendritic crystals from polarimetric radar data. *J. Atmos. Sci.*, **62**, 241–250.

Meischner P., R. Bauman, H. Holler, T. Jank. 2001: Eddy dissipation rates in thunderstorms estimated by Doppler radar in relation to aircraft *in situ* measurements. *J. Atmos. Ocean.*

Technol., 18, 1609-1627.

Melnikov, V, and D. Zrnic, 2004: Simultaneous transmission mode for the polarimetric WSR-88D: Statistical biases and standard deviations of polarimetric variables, NSSL report, 84 pp. Online: http://www.nssl.noaa.gov/publications/wsr88d_reports/SHV_statistics.pdf

Melnikov, V.M., D. S. Zrnić, R. J. Doviak, P. B. Chilson, D. B. Mechem, and Y. L. Kogan, 2011 Melnikov, V., and R. J. Doviak, 2009: Turbulence and wind shear in layers of large Doppler spectrum width in stratiform precipitation. *J. Atmos. Oceanic Technol*., **26**, 430-443.: Prospects of the WSR-88D radar for cloud studies. *J. Appl. Meteor. Climatol.*, **50**, 859–872.

Melnikov, V., and J. Straka, 2013: Axis ratios and flutter angles of cloud ice particles: retrievals from radar data. *J. Atmos. Oceanic Technol.*, **30**, 1691–1703.

Miller M. A., J. Verlinde, G. V. Gilbert, G. J. Lehenbauer, J. S. Tongue, E. E. Clothiaux, 1998: Detection of nonprecipitating clouds with the WSR-88D: A theoretical and experimental survey of capabilities and limitations. *Weather and Forecasting*, **13**, 1046- 1062.

Mischenko, M.I., L.D. Travis, and A.A. Lacis, 2002: *Scattering, Absorbtion, and Emission of Light by Small Particles",* Cambridge University Press, 228 pp.

Moran, K.P., B. E. Martner, M.J. Post, R.A. Kropfli, D.C. Welsh, and K. B. Widener, 1998: An unattended cloud profiling radar for use in climate research. *Bull. Amer. Meteor. Soc.*, **79**(3), 443 – 455.

Mott, H., 1992: *Antennas for radar and communications*. J. Wiley&Sons, NY, 521 pp.

Nastrom, G. D., and F. D. Eaton, 1997: Turbulence eddy dissipation rates from radar observations at 5-20 km at White Sands Missile Range, New Mexico. *J. Geophys. Res.,* **102**, **D16**, 19, 495-505.

Pruppacher, H. R., and J. D. Klett, 1997: *Microphysics of Clouds and Precipitation*. Kluwer Academic, 954 pp.

Proctor, F. H., D. W. Hamilton, and R. L. Bowles, 2002: Numerical simulation of a convective turbulence encounter. Preprints *10th Conference on Aviation, Range, and Aerospace Meteorology, AMS, Paper 2.3*, pp. 41-44.

Rogers, R.R. and B.R. Tripp, 1964: Some radar measurements of turbulence in snow. *J. Applied Meteor.,* 3, 603 – 610.

Ryzhkov, A., M. Pinsky, A. Pokrovski, and A. Khain, 2011: Polarimetric radar observation operator for a cloud model with spectral microphysics. *J. Applied Meteorol. Climat.* **50**, 873 - 894.

Sharman, R., L. Cornman, J. Williams, S. Koch, and W. Moninger, 2006: The FAA AWRP Turbulence PDT. Preprints *12th Conference on Aviation, Range, and Aerospace Meteorology, AMS, Paper* 3.3, 22pp.

Stephens G. L, D.G. Vane, R.J. Boain, G.G. Mace, K. Sassen, Z. Wang, A. J. Illingworth, J. O'Connor, W. B. Rossow, S.L. Durden, S.D. Miller, R.T. Austin, A. Benedetti, C. Mitrescu, 2002: The CLOUDSAT mission and the A-train. *Bull. Amer.Meteor. Soc.*, Dec, 1771-1790.

Stephens G. L, and C. D. Kummerow, 2007: The remote sensing of clouds and precipitation from space: A review, *J. Atmos. Sci.*, **64**, 3742-3765.

Tang, C., and K. Aydin, 1995: Scattering from ice crystals at 94 and 220 GHz millimeter wave frequencies. *IEEE Trans.* **GRS-33**, No 1, 93-99.

Treinish, L. 2002: How can we build more effective weather visualization? Task-specific visualization design. Available online at http://www.research.ibm.com/weather.

Trout, D., and H. A. Panofsky, 1969: Energy dissipation near the tropopause. *Tellus*, **21**, 355-358.

Vivekanandan, J., W. M. Adams, and V. N. Bringi, 1991: Rigorous approach to polarimetric radar modeling of hydrometeor orientation distributions, *J. Appl. Meteorol.,* **30**, 1053–1063.

Woodman, R F., and A. Guillen, 1974: Radar observations of winds and turbulence in the stratosphere and mesosphere. *J. Atmos. Sci.* **31**, March. 493-505.

Zikmunda, J., and G. Vali, 1972: Fall patterns and fall velocities of rimed ice crystals. *J. Atmos. Sci.,* **29,** 1334–1347.

Zrnic D.S., and A. V. Ryzhkov, 1999: Polarimetry for weather surveillance radars. *Bull. Amer. Meteorol. Soc.*, **80** (3), 389-406.